

Computational Study of Hypersonic Double-Cone Experiments for Code Validation

A THESIS
SUBMITTED TO THE FACULTY OF THE GRADUATE SCHOOL
OF THE UNIVERSITY OF MINNESOTA
BY

Ioannis Nompelis

IN PARTIAL FULFILLMENT OF THE REQUIREMENTS
FOR THE DEGREE OF
DOCTOR OF PHILOSOPHY

May 2004

© Ioannis Nompelis 2004

UNIVERSITY OF MINNESOTA

This is to certify that I have examined this copy of a doctoral thesis by

Ioannis Nompelis

and have found that it is complete and satisfactory in all respects,
and that any and all revisions required by the final
examining committee have been made.

Graham V. Candler

Name of Faculty Adviser

Signature of Faculty Adviser

Date

GRADUATE SCHOOL

Acknowledgments

I am grateful to many individuals who helped, directly and indirectly, in making this dissertation possible. First, I would like to thank my adviser and friend Professor Graham Candler, for introducing me to the exciting world of numerical simulation, for motivating this work, and for his constant support, encouragement and guidance. Dr. Michael Wright has helped enormously with all aspects of CFD, and I have gained much of that knowledge from our many discussions and by reading his works. Dr. Marie-Claude Druguet provided insight on the numerical schemes while doing a lot of the work on numerics that is included in this dissertation, and it was a pleasure working with her. Timothy Wadhams and Dr. Michael Holden provided all the experimental results, and were in close cooperation with us throughout the evolution of this work. I would also like to thank the members of the examining committee, Professors Ivan Marusic, Krishnan Mahesh and Bernardo Cockburn, and the many friends and colleagues at the University of Minnesota. I would particularly like to thank Dr. Konstantinos Hennighausen, Dr. Manoj Nagulapally, Ramnath Kandala and Chuck Campbell for all the fruitful discussions we had and for all their help. Finally, I am the most grateful to my family, my parents Vasileios and Amalia, my sister Alexia, my aunt Marianthi, and my wife Constance. They provided me with the support and encouragement that I needed.

Abstract

Numerical methods are used extensively for the solution of the coupled gasdynamic and gaskinetic equations that describe hypersonic flows with chemical reactions and nonequilibrium phenomena. Modern computational fluid dynamics (CFD) codes used for numerical simulations employ various models that describe physical phenomena such as energy relaxation, chemical reaction rates and diffusion processes. Additionally, novel algorithms have been developed for the efficient implementation of the numerical methods of solution on parallel computers. The objective of this work is to assess the ability of current state-of-the-art methods to simulate challenging hypersonic flow problems by comparing to well characterized experiments. This process involves simulation of experiments performed in inert environments, aiming to evaluate the quality of the numerics, followed by simulations of reacting flow experiments aiming to evaluate the accuracy of physical models. In this work, hypersonic double-cone flows are studied. The hypersonic flow past a double-cone model is a good test for numerical methods because it produces a very complicated shock interaction, and it requires a large number of grid points to simulate accurately. This thesis focuses on the simulation of a series of double-cone experiments performed at the Large Energy National Shock (LENS) facility using a reflected shock tunnel and an expansion tunnel. Simulations of experiments at low enthalpy showed very good agreement with measurements, and the discrepancies observed initially between numerical predictions and the experimental measurements were largely a result of having vibrational energy frozen in the free-stream. Simulations of high enthalpy experiments showed good agreement for nitrogen flows, and only qualitative agreement for air flows.

Contents

Acknowledgments	i
Abstract	ii
Contents	iii
List of Tables	vi
List of Figures	vii
1 Introduction	1
1.1 Motivations	1
1.2 Double-Cone Flows.	2
1.3 Review of Related Work	5
1.4 Scope of the Current Study	6
2 Mathematical Formulation	9
2.1 Introduction	9
2.2 Basic Assumptions	9
2.3 The Conservation Equations.	10
2.4 Equations of State	11
2.5 The Diffusive Terms	13
2.6 The Chemical Source Terms	15
2.7 Vibrational Energy Source Term	17
2.8 Boundary conditions	19
3 Numerical Method	21
3.1 Introduction	21
3.2 The Finite Volume Method	21
3.3 Evaluation of the Fluxes	23
3.4 Time Advancement.	28
3.5 The Data-Parallel Line Relaxation	31

3.6	Boundary Conditions	33
3.7	Other Flux Evaluation Methods	34
3.8	Second Order Spatial Accuracy	35
4	Low Enthalpy Double-Cone Experiments	37
4.1	Introduction	37
4.2	Low Enthalpy LENS Experiments	38
4.3	Computations of the Experiments	39
4.4	Remarks on Blind Comparisons	45
5	Effects of Numerics on Double-Cone Flows	49
5.1	Introduction	49
5.2	Grid Size Requirements	50
5.3	Importance of Time Integration Method	50
5.4	Flux Evaluation Methods	52
5.5	Time Convergence	53
5.6	Results on Coarse Grids	53
5.7	Results on Fine Grids	56
5.8	Evolution of the Separation Zone Size	57
5.9	Conclusions	59
6	Characterization of Experiments	60
6.1	Introduction	60
6.2	Vibrational Nonequilibrium	60
6.3	Nozzle Flow Simulations	63
6.4	Results	66
6.5	Under-resolved Solutions	72
6.6	Results for Low Density Experiments	75
6.7	Conclusions	80
7	High Enthalpy Double-Cone Experiments	81
7.1	Introduction	81

7.2	Design of High Enthalpy Experiments	81
7.3	High Enthalpy Double-Cone Flows	83
7.4	Nozzle Flow Simulations	89
7.5	Simulations at Computed Conditions	93
7.6	Conclusions	96
8	Design of Experiments in the Expansion Tube	98
8.1	Introduction	98
8.2	Expansion Tube Experiments	99
8.3	Computational Procedure	101
8.4	One-Dimensional Analysis	102
8.5	Two-dimensional Simulations	104
8.6	Nozzle Flow Simulations	106
8.7	Double-Cone Flow	111
8.8	Conclusions	111
9	Summary and Conclusions	107
9.1	Summary	113
9.2	Conclusions	114
9.3	Recommendations for Future Research	116
	Appendix A: Model Constants	117
	Appendix B: The Axisymmetric Finite Volume Formulation	119
	Appendix C: The Inviscid Flux Jacobians	126
	Appendix D: The Implicit Viscous Jacobians	130
	Appendix E: The Implicit Source Term Jacobians	133
	References	137

List of Tables

<i>Table</i>		<i>Page</i>
4.1 Free-stream and wall conditions for the 25°-55° sharp double-cone LENS experiments.	39	
6.1 Nominal and computed test-section conditions for Run 35 reservoir conditions.	65	
6.2 Nominal and computed test-section conditions for Run 28 reservoir conditions.	65	
6.3 Free-stream and wall conditions for the “1/2 density” (Run 4) and “1/3 density” (Run 5) 25°-55° sharp double-cone LENS experiments.	77	
7.1 Nominal free-stream and wall conditions for the 25-55° sharp double-cone high enthalpy experiments.	83	
7.2 Computed test-section conditions for the 25-55° sharp double-cone high enthalpy experiments.	93	
8.1 Initial experimental conditions for LENS-X.	101	
8.2 Computed free-stream conditions at the exit-plane of the nozzle for case A.	111	
A.1 Characteristic harmonic oscillator vibrational temperatures (K).	117	
A.2 Formation enthalpies for each species (J/kg).	117	
A.3 Viscosity Coefficients for the Blottner Model.	117	
A.4 Arrhenius coefficients for forward reaction rates.	118	
A.5 Constants for computing K_{eq}	118	

List of Figures

<i>Figure</i>	<i>Page</i>
1.1 Schematic diagram of a typical flow-field generated by a 25°-55° double-cone geometry placed in a Mach 12 free-stream. The flow is from left to right, and a slice is shown of flow that is circularly symmetric about the axis of the geometry.	4
4.1 Computed Mach number contours of the flow generated by a 25°-55° double-cone geometry at Run 28 conditions.	41
4.2 Experimental (a) and numerical (b) Schlieren images for LENS Run 28.	41
4.3 Computed surface pressure and experimental measurements plotted versus axial distance on the 25°-55° double-cone geometry at Run 28 conditions.	42
4.4 Computed heat transfer rate and experimental measurements plotted versus axial distance on the 25°-55° double-cone geometry at Run 28 conditions.	43
4.5 Computed Mach number contours of the flow generated by a 25°-55° double-cone geometry at Run 35 conditions.	44
4.6 Experimental (a) and numerical (b) Schlieren images for LENS Run 35.	44
4.7 Computed surface pressure and experimental measurements plotted versus axial length of the 25°-55° double-cone geometry at Run 35 conditions.	46

4.8	Computed heat transfer rate and experimental measurements plotted versus axial length of the 25°-55° double-cone geometry at Run 35 conditions.	47
5.1	Heat transfer rate for a perfect gas simulation computed on four different grids; (b) shows an enlargement near the point of separation.	51
5.2	Shock location ($T = 400$ K contour) computed with different flux evaluation methods on a 256×128 grid.	54
5.3	Shock location ($T = 400$ K contour) computed with the Roe scheme and different slope limiters on a 256×128 grid.	55
5.4	Surface pressure predictions on the double-cone computed with different flux evaluation methods on a 256×128 grid.	55
5.5	Surface pressure predictions on the double-cone computed with different flux evaluation methods on a 256×128 grid.	56
5.6	Surface pressure on the double-cone model computed with the Lax-Friedrichs scheme and different slope limiters on a 1024×512 grid.	57
5.7	Size of the recirculation zone versus the square of the inverse of the number of points in the streamwise direction.	58
6.1	Pitot pressure in the nozzle exit-plane compared with nozzle computation for Run 1302 (calibration for Run 35).	64
6.2	Heat transfer rate and surface pressure for nominal Run 35 conditions.	67
6.3	Heat transfer rate and surface pressure for nonequilibrium Run 35 conditions.	69
6.4	Heat transfer rate for nonequilibrium Run 35 conditions and $\sigma_v = 0.001$	70

6.5	Computed Mach number contours in the test-section and with double-cone flow solution superimposed.	71
6.6	Heat transfer rate for non-uniform Run 35 conditions and $\sigma_v = 0.001$	71
6.7	Heat transfer rate and surface pressure for nonequilibrium Run 28 conditions.	73
6.8	Heat transfer rate for nonequilibrium Run 28 conditions and $\sigma_v = 0.001$	74
6.9	Heat transfer rate for non-uniform Run 28 conditions and $\sigma_v = 0.001$	74
6.10	Heat transfer rate for (a) nominal and (b) nonequilibrium Run 28 conditions computed on the coarse grid (256×128).	76
6.11	Heat transfer rate for non-uniform Run 28 conditions with $\sigma_v = 0.001$ computed on the coarse grid (256×128).	77
6.12	Heat transfer rate for nonequilibrium Run 4 conditions with $\sigma_v = 0.5$ (solid line) and $\sigma_v = 0.001$ (dashed line).	79
6.13	Heat transfer rate for nonequilibrium Run 5 conditions with $\sigma_v = 0.5$ (solid line) and $\sigma_v = 0.001$ (dashed line).	79
7.1	Schematic of double-cone flow-field at high-enthalpy nitrogen free-stream conditions (Run 42).	84
7.2	Surface pressure (a) and heat transfer rate to the model (b) for high enthalpy nitrogen free-stream conditions (Run 42).	85
7.3	Surface pressure (a) and heat transfer rate to the model (b) for high enthalpy nitrogen free-stream conditions (Run 46).	86
7.4	Surface pressure (a) and heat transfer rate (b) to the model for high enthalpy air free-stream conditions (Run 43).	88

7.5	Shear layer Reynolds numbers at the edge of the separation region calculated based on the Birch and Keyes definition for Run 42 and Run 43. The low enthalpy Run 35 result is plotted for reference.	89
7.6	Predicted and measured Pitot pressure profiles for the calibration run in nitrogen (Run 187).	90
7.7	Velocity profiles of the nozzle wall boundary layer from the Run 42 calibration case plotted in wall variables.	91
7.8	Heat transfer rate predictions and measurements at the wall for Run 187 and Run 188.	91
7.9	Predicted and measured Pitot pressure profiles for the calibration run in air (Run 188).	92
7.10	Predicted surface pressure (a) and heat transfer rate (b) for Run 42 computed test-section conditions.	94
7.11	Predicted surface pressure (a) and heat transfer rate (b) for Run 43 computed test-section conditions.	95
8.1	Schematic of an expansion tube and its $x - t$ diagram.	100
8.2	Evolution of the 1-D flow in the expansion tube after rupture of (a) the primary diaphragm and (b) the secondary diaphragm for case A.	103
8.3	Snapshot of the 1-D flow in the expansion tube for case B.	104
8.4	Snapshot of the laminar (top) and fully turbulent (bottom) flows inside the expansion tube – temperature contours are shown.	106
8.5	State variables and species mass-fractions at the centerline of the tube for laminar (left) and fully turbulent (right) flow snapshots of Fig. (8.4).	107

8.6	Computed and measured time history of the Pitot pressure (left) and computed wall pressure (right) near the exit of the expansion section.	108
8.7	Computed time history of the Pitot pressure at the nozzle exit-plane.	109
8.8	Computed axial velocity (top), Mach number (middle), and Pitot pressure (bottom) at the nozzle exit-plane.	110

Chapter 1

Introduction

1.1 Motivations

There has been a great deal of interest in developing prototype re-entry vehicles and hypersonic air-breathing vehicles for access to space. These vehicles will be designed to operate in the high enthalpy regime, where the flow exhibits high enthalpy or “real-gas” effects. Real-gas effects are triggered by the high temperatures encountered in high enthalpy flows. These effects include excitation of the internal energy modes of the gas, as well as dissociation of polyatomic species and ionization. These physical phenomena occur over a range of time scales, and the flow is frequently in chemical and thermal nonequilibrium. Additionally, depending on the shape of the vehicle and the flight conditions, shock/shock interactions and viscous-inviscid interactions will likely occur during flight at hypersonic speeds. The combined effects of these phenomena and real-gas chemistry may dramatically alter the flight characteristics of the vehicle. Therefore, all of these effects must be taken into consideration in the development stage of future hypersonic vehicles.

The development and design of such vehicles is aided by the use of experimentation and numerical simulation. There are difficulties associated with both approaches. It is difficult to produce ground-based hypersonic flow experiments that are realistic in terms of the enthalpy and composition of the gas. It is also difficult to perform accurate numerical simulations, as the physics involved is not fully understood. For example, in the sudden expansion of high temperature air, the coupled vibrational relaxation and chemical recombination process is poorly understood. This is an example where modeling of the thermochemistry is important,

and uncertainty is introduced into the simulation through the chemical reaction rates. It also appears that critically important hypersonic flow phenomena such as shock/shock and viscous-inviscid interactions cannot be predicted accurately. Hypersonic flows with regions of separation induced by shock/shock interactions have been very difficult problems to tackle computationally. These flow phenomena are associated with a large range of length scales, particularly at high Reynolds numbers. In many cases, a large number of grid points is required in order to accurately predict the basic flow structure. This increases substantially the cost of numerical simulations.

It is clear that although there are different aspects of hypersonic flow – each exhibiting its own idiosyncrasies – the physical processes may not be separated and decoupled in numerical simulations for practical problems. Therefore it is important to get a perspective view on the reliability and versatility of numerical prediction techniques used in real-life applications. The accuracy of popular numerical methods used in computational fluid dynamics (CFD) codes must be assessed, along with the accuracy of existing nonequilibrium chemistry models. Furthermore, it is important to understand the limitations of the particular numerical methods and physical models. To achieve this, we typically require that the numerical simulation is tested against a problem for which the solution is known. For the complex problems of interest, analytical solutions cannot be obtained. As an alternative, numerical prediction techniques are required to reproduce experimental measurements at well characterized conditions.

1.2 Double-Cone Flows

Flows generated by double-cone geometries placed in hypersonic free-streams have been studied in the past. Earlier studies of these flows focused primarily on testing and improving nonequilibrium chemistry models. This is because the double-cone flows are sensitive to high enthalpy effects, and it has been speculated that their sensitivity to real-gas chemistry would allow for discriminating between

air chemistry models. The double-cone flows are also very difficult to simulate numerically, and thus they can be utilized as a comprehensive test of CFD codes.

The flow generated by a double-cone configuration placed in a hypersonic free-stream, exhibits strong viscous-inviscid and shock/shock interactions. The oblique shock generated by the first, shallow-angle cone, interacts with the shock generated by the second cone. When the second cone angle is larger than a critical angle, this shock is detached, and the interaction is very strong. A schematic of the flow generated by a double-cone in a nitrogen free-stream at a Mach number of about 12 is shown in Fig. (1.1). In this figure, the model has a first cone half-angle of 25° and a second cone half-angle of 55° . The shock structure and subsonic regions are outlined, and the shear layers are visualized. The oblique shock interacts with the bow shock generated by the second cone, and a transmitted shock is formed, which impinges on the surface downstream of the cone-cone juncture. The adverse pressure gradient at the cone-cone juncture causes the boundary layer to separate. The separated region that forms at the corner creates its own shock, which interacts with the bow shock. This shifts the point of interaction, which in turn alters the separation zone. This process feeds back on itself until the flow reaches steady state – if a steady state exists. A supersonic jet is formed along the surface of the second cone downstream of the impingement point, and it undergoes a series of isentropic compressions and expansions. The flow behind the strong bow shock is subsonic, and therefore the shape of the jet influences the shock structure.

The complex flow phenomena exhibited by double-cone geometries under hypersonic conditions make the flow very difficult to compute with CFD. This is mainly because of two reasons. First, there is a large range of scales that must be resolved. In particular, the boundary layer that grows along the first cone influences the location of the oblique shock. A large number of grid points with stretching near the wall is required to correctly resolve the boundary layer growth near the tip, the scale of which is much smaller compared to the size of the geometry.

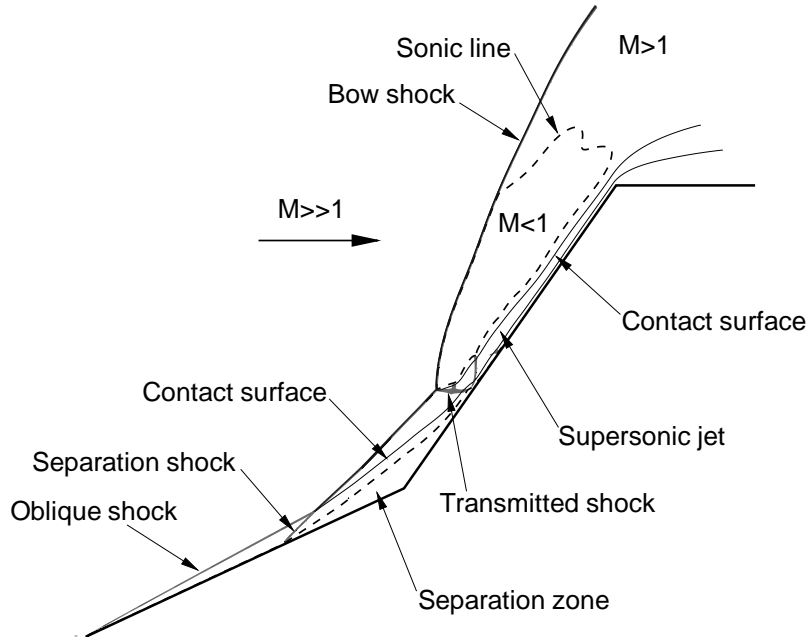


Fig. 1.1 Schematic diagram of a typical flow-field generated by a 25° - 55° double-cone geometry placed in a Mach 12 free-stream. The flow is from left to right, and a slice is shown of flow that is circularly symmetric about the axis of the geometry.

Also, the triple point and the point of re-attachment must be correctly resolved, because they directly influence the size of the separation zone. Thus, fine grid spacing is also required near the point of interaction and re-attachment. Therefore, a very fine mesh is required for double-cone simulations. Second, the presence of separation results in a feedback mechanism by which the separation zone continuously evolves, and this process takes a long time to reach steady state relative to the characteristic flow time. We refer to a *characteristic flow time* as the time it takes for a particle to travel the length of the geometry if it is moving at the free-stream velocity. Therefore, the combined requirements of having high grid resolution and having to simulate large amounts of physical time, make such simu-

lations extremely expensive. We may seek to reduce the number of grid points by making use of higher order low dissipation methods. Even in this case, an efficient implicit time-integration method is required in order to have reasonable turn-around times on a parallel computer. Therefore, despite the simplicity of the geometry, the double-cone flow is a stringent test for numerical methods and algorithms.

Under high enthalpy conditions, the chemical processes that take place in the flow are tightly coupled with the fluid motion through energy exchange mechanisms. In high enthalpy double-cone flows, dissociation takes place both in the high temperature region behind the bow shock, and inside the separation zone. In these regions, the highly energetic particles undergo collisions and lose some of their energy by causing dissociation of polyatomic species. By this process, energy is removed from the bulk flow and stored in the form of chemical energy. The rate at which this process takes place greatly impacts the mean flow. Thus, the size of the embedded region of separation is sensitive to chemical effects in the flow. Additionally, the size of the separation zone may be measured experimentally by surface measurements such as surface pressure and heat transfer rate. Thus, we can make direct comparisons between numerical predictions and experimental measurements. This is a desirable attribute for a flow that may be used as a test case for validating and improving nonequilibrium chemistry models. Therefore, provided that a given numerical method is able to accurately predict double-cone flows in the absence of flow-field chemistry, thermochemical models can be tested using double-cone flows of high enthalpy.

1.3 Review of Related Work

Hypersonic double-cone and double-wedge flows have been studied extensively both numerically and experimentally. In the 1990's, attempts were made to compare simulations results with experimental data for these interacting flows. The results of these studies showed good agreement in some cases, but in many cases the efforts were not as successful.

Olejniczak *et al.* (1999) made use of double-wedges placed in a hypersonic free-stream at the California Institute of Technology Free-Piston Shock Tunnel T5 to test different nonequilibrium chemistry models. They did not obtain good agreement in terms of the separation zone size and distribution of surface quantities, and they attributed this to inadequate modeling of the thermochemistry and flow physics. Around the same time, Olejniczak *et al.* (1997a) studied inviscid shock interactions on double-wedges and found that in many cases the gas dynamics have a dominant effect on the surface pressure distribution. This explained the pressure variations near the re-attachment point of the flow, which were thought to be due to real-gas effects. Attempts to reproduce double-cone experiments in high enthalpy nitrogen were also unsuccessful [Olejniczak *et al.* (1997b)]. These efforts were aimed at testing nonequilibrium chemistry models using hypersonic flows with shock interactions.

More recent simulations of double-cone flows by Wright *et al.* (2000) of experiments performed at the Princeton University Mach 8 Wind Tunnel showed good agreement with measurements. They showed that laminar simulations predicted the surface quantities at low Reynolds numbers. Also, for higher Reynolds numbers, where the flow was believed to be transitional, turbulent simulations showed good agreement.

1.4 Scope of the Current Study

In this work, we use computational fluid dynamics to study hypersonic double-cone flows. Double-cone flows under both low enthalpy and high enthalpy conditions are investigated. This work aims toward the validation of physical models and numerical methods that are employed in computational fluid dynamics codes. It serves as a starting point for code validation, and is intended to understand the extent to which numerical methods can predict hypersonic low-density flows with laminar regions of separation in the presence of chemical reactions. We attempt to systematically isolate each of the physical aspects that introduce uncertainty. For

example, the uncertainty in turbulence modeling is eliminated by ensuring that the Reynolds number is low enough such that the flow remains laminar. Also, high enthalpy, or “real-gas” effects are minimized in flows at low enough enthalpy, and for which perfect-gas numerical predictions can be made. The geometry considered is one that produces strong viscous-inviscid and shock/shock interactions, while the flow remains steady. We compare numerical simulation results with experimental data obtained in the Large Energy National Shock tunnel (LENS) facility, at the Calspan - University at Buffalo Research Center (CUBRC).

In chapters 2 and 3 we present the governing equations for the continuum flow of a gas in vibrational and chemical nonequilibrium. The Navier-Stokes equations for a chemically reacting and vibrationally relaxing air mixture are presented, as well as their numerical method of solution. We use standard numerical techniques which are popular among researchers and have been widely used for practical applications. In the same context, the standard models used for vibrational relaxation and chemical reaction rates are presented, as well as the models for the transport coefficients.

Chapter 4 focuses on low enthalpy hypersonic double-cone flows in inert environments. Comparisons between experimental measurements and *blind* simulation results are presented, with the aim to provide an objective assessment of the state of current simulation methods. Chapter 5 is concerned with the numerical aspects of these simulations, and presents sensitivity studies related to the discretization of the equations and the accuracy of the numerical methods. An assessment of the rate of convergence is also made for this particular class of flows.

Chapter 6 contains a more detailed analysis of the low enthalpy simulation results, and numerical simulations of the entire experiments are presented. These include simulations of the hypersonic facility nozzle, where comparisons are made between numerical predictions and measurements made by the Pitot pressure probes at the nozzle exit plane. As a result, an important idiosyncrasy of these low density flows is uncovered. Using this approach, the free-stream conditions are revisited

and additional characterization of the experimental facility is done using CFD. Further double-cone simulations and comparisons with experimental measurements are presented.

Chapter 7 discusses work on high enthalpy double-cone flows that was performed guided by the methodology developed by studying the low enthalpy experiments. Comparisons between experimental measurements and numerical predictions for high enthalpy air and nitrogen mixtures are presented.

Chapter 8 examines high enthalpy experiments performed using an expansion tube facility. This is done by using CFD to simulate the entire experiment. The objective is to help the design of future high enthalpy experiments with non-reacted free-streams. Using this approach, additional characterization of the facility is provided in terms of available test-time.

Chapter 2

Mathematical Formulation

2.1 Introduction

In this chapter, we introduce the set of coupled partial differential equations that describes the dynamics of the flow-field. For the high enthalpy flows of interest, the standard mass, momentum and energy equations are not sufficient to describe the thermochemical state of the gas and physics involved. The high temperatures inherent to these flows trigger a number of chemical and energy relaxation processes, or “real-gas” effects, and the flows are frequently in substantial nonequilibrium. We account for real-gas effects by introducing finite-rate chemical reactions and internal energy relaxation to the conservation equations.

The Navier-Stokes equation set has been extended so that it accurately describes the physics of a gas that is vibrationally excited and chemically reacting [Candler (1988), Olejniczak (1997)], and it is only briefly presented here. The equation of state of the gas is developed. The models used for the transfer of mass between different chemical species, transport of momentum, and the transfer of energy between different energy modes are discussed along with their underlying assumptions.

2.2 Basic Assumptions

The flowfields are assumed to be accurately described by a continuum formulation. For this assumption to be valid, the Knudsen number defined as the ratio of the mean free path to the length scale of the flow $\text{Kn} = \lambda/L$, must be small. For the flows of interest the Knudsen number is of the order of 0.1-0.001 based on the model size, and thus the flowfield is in the continuum regime. It is implicit in the

continuum formulation that there is little statistical variation at any point in the flow and therefore the continuum description of the viscous fluxes is consistent.

We restrict the formulation to non-ionized, chemically reacting flows. The rotational state of the gas typically equilibrates within a few collisions and we can assume that the translational and rotational states of the gas are in equilibrium at a common temperature. In this work we do not consider electronic excitation of the particles.

2.3 The Conservation Equations

For a chemically reacting mixture of ns species, of which nd are diatomic, there are ns species mass conservation equations of the form

$$\frac{\partial \rho_s}{\partial t} + \nabla \cdot (\rho_s \vec{u}) = -\nabla \cdot (\rho_s \vec{v}_s) + w_s , \quad 1.1$$

where ρ_s is the density of species s , \vec{v}_s is the species diffusion velocity, and w_s is the rate of production of the species due to chemical reactions. By summing the species density over all species we get the mixture density ρ . If we sum the species mass conservation equation over all species s , the source terms that appear on the right hand side sum identically to zero and we recover the traditional continuity equation. The models used to describe the diffusion velocities and the form of the source terms will be discussed in subsequent sections.

The conservation of linear momentum is expressed as

$$\frac{\partial(\rho \vec{u})}{\partial t} + \nabla \cdot (\rho \vec{u} \otimes \vec{u} + pI) = \nabla \cdot \tilde{\tau} , \quad 1.2$$

where p is the thermodynamic pressure and $\tilde{\tau}$ is the viscous stress tensor. This vector equation represents 3 momentum equations, one for each spatial dimensions of the problem. The above expression assumes that there are no external body forces exerted on the particles. Note that diffusion velocities do not appear in the momentum equation as their contributions sum identically to zero (see Olejniczak (1997) for the details of the calculation).

The conservation of total energy of the mixture is given by

$$\frac{\partial E}{\partial t} + \nabla \cdot ((E + p)\vec{u}) = \nabla \cdot (\tilde{\tau}\vec{u}) - \nabla \cdot (\vec{q}_t + \vec{q}_r + \vec{q}_v) - \nabla \cdot \sum_{s=1}^{ns} (\rho_s h_s \vec{v}_s) , \quad 1.3$$

where \vec{q}_t , \vec{q}_r , \vec{q}_v are the translational, rotational and vibrational heat flux vectors, and h_s is the total enthalpy per unit mass of species s . The terms present in the energy equation will be discussed separately.

In our formulation we assume that vibration-vibration energy coupling is very strong such that all vibrational modes are in equilibrium with each other. Thus the vibrational energy of the diatomic species can be described by a single vibrational temperature. This is a significant simplification as we only have one vibrational energy conservation equation, while in principle we need to have a separate equation for each of the polyatomic species. The equation for the vibrational energy per unit volume is given as

$$\frac{\partial E_v}{\partial t} + \nabla \cdot (E_v \vec{u}) = -\nabla \cdot \vec{q}_v - \nabla \cdot \sum_{s=1}^{nd} (\rho_s e_{vs} \vec{v}_s) + w_v , \quad 1.4$$

where e_{vs} is the vibrational energy per unit mass of species s . The source term appearing on the right hand side of the equation will be discussed in the subsequent sections.

2.4 Equations of State

In this section, we show how conserved variables relate to the primitive flow variables, such as temperature, and pressure that appears in the conservation equations. The total energy per unit volume of the gas is defined as

$$E = \sum_{s=1}^{ns} \rho_s C_{vs} T + \frac{1}{2} \rho |\vec{u}|^2 + \sum_{s=1}^{nd} e_{vs} \rho_s + \sum_{s=1}^{ns} h_s^\circ \rho_s ,$$

where C_{vs} is the translational-rotational specific heat at constant volume for species s , and is given by

$$C_{vs} = C_{vs}^{(tr)} + C_{vs}^{(rot)} .$$

The translational and rotational specific heats are given by

$$\begin{aligned} C_{vs}^{(tr)} &= \frac{3}{2} \frac{R}{M_s} \\ C_{vs}^{(rot)} &= \frac{R}{M_s} \quad s \leq nd, \end{aligned}$$

where R is the universal gas constant and M_s is the species molecular weight. Thus the first term in the energy corresponds to the internal energy of the gas due to thermal translational-rotational motion of particles. The second term represents the bulk kinetic energy of the gas. The third term represents the vibrational energy of the polyatomic species. The vibrational energy per unit mass e_{vs} of species s is related to the vibrational temperature T_v assuming a Boltzmann distribution exists. In this work, we use a simple harmonic oscillator model to represent the vibrational excitation of diatomic species and this internal energy is expressed as

$$e_{vs} = \frac{R}{M_s} \frac{\theta_{vs}}{\exp(\theta_{vs}/T_v) - 1},$$

where θ_{vs} is the characteristic temperature of vibration for species s . Note that it is not possible to solve this equation directly for T_v , and therefore the vibrational temperature must be computed iteratively for a given vibrational energy $E_v = \sum_{s=1}^{nd} \rho_s e_{vs}$. The final term in the expression for the total energy represents the chemical energy of formation associated with each species. The values of the formation enthalpies h_s° are given in the appendix.

The thermodynamic pressure p is related to the translational-rotational temperature through a perfect gas law and is obtained by Dalton's Law of partial pressures of the species as

$$p = \sum_{s=1}^{ns} p_s = \sum_{s=1}^{ns} \rho_s \frac{R}{M_s} T = \rho \bar{R} T, \quad \text{and} \quad \bar{R} \equiv \sum_{s=1}^{ns} \frac{\rho_s}{\rho} \frac{R}{M_s}.$$

The enthalpy per unit mass of species s is defined to be

$$h_s = C_{vs} T + \frac{p_s}{\rho_s} + e_{vs} + h_s^\circ.$$

2.5 The Diffusive Terms

In this section we describe the viscous, thermal and mass diffusion fluxes that appear in the conservation equations, and their constitutive relations.

The viscous stress tensor is formed assuming a Newtonian fluid and is given by

$$\tilde{\tau} = \mu(\nabla \vec{u} + (\nabla \vec{u})^T) + \lambda(\nabla \cdot \vec{u})I ,$$

with the Stokes hypothesis for the bulk viscosity

$$2\mu + 3\lambda = 0 ,$$

where μ is the kinematic viscosity of the mixture. The viscosity μ depends on the state of the fluid and its composition and will be discussed in detail below.

The heat fluxes are assumed to obey Fourier's Law and given by

$$\vec{q}_i = -\kappa_i \nabla T_i ,$$

where i represents *any* of the internal energy modes of the gas, with κ_i and T_i the corresponding conductivity and temperature. Since the translational and rotational states of the gas are in equilibrium at a common temperature, it is convenient to combine the corresponding heat fluxes into a sum of the conductivities times the temperature gradient as

$$\vec{q} = \vec{q}_t + \vec{q}_r = -(\kappa_t + \kappa_r) \nabla T .$$

The thermal conductivities for the translational, rotational, and vibrational energy modes are determined from an Eucken relation [Vincenti and Kruger (1986)] as

$$\kappa_{ts} = \frac{5}{2}\mu_s C_{vs}^{(tr)} , \quad \kappa_{rs} = \mu_s C_{vs}^{(rot)} , \quad \kappa_{vs} = \mu_s C_{vs}^{(vib)} ,$$

where μ_s and κ_s are the species viscosities and thermal conductivities. The vibrational specific heat is computed directly using

$$C_{vs}^{(vib)} = \frac{\partial e_{vs}}{\partial T_v} .$$

Mass diffusion is driven by gradients of concentration, pressure, and temperature. However, for the flows of interest only the terms due to concentration gradients are significant. Thermal diffusion is important in regions where gradients are large, but in these regions the fundamental continuum assumption is typically invalid and we can no longer apply the Navier-Stokes equations [Boyd *et al.* (1995)]. The barodiffusion terms are negligible. Therefore, for this work the mass diffusion is solely based on concentration gradients and Fick's Law is used. The mass diffusion flux is

$$\rho_s \vec{v}_s = -\rho \mathcal{D}_s \nabla \left(\frac{\rho_s}{\rho} \right) .$$

The multicomponent diffusion coefficients \mathcal{D}_s are replaced with a single binary diffusion coefficient \mathcal{D} , which is derived assuming a constant Lewis number, Le, defined as

$$\text{Le} = \mathcal{D} \frac{\rho C_p}{\kappa} ,$$

where C_p is the translational-rotational specific heat at constant pressure and κ is the thermal conductivity of the mixture. The effects of multicomponent diffusion have been neglected, however they should be included if light species, such as hydrogen, are present in the flow.

It now remains to provide expressions for the mixture viscosity, the thermal conductivity and the species viscosities. The mixture viscosity μ and thermal conductivity κ are obtained from the species viscosities and conductivities μ_s , κ_s using Wilke's semi-empirical mixing rule [Wilke (1950)]

$$\mu = \sum_s \frac{X_s \mu_s}{\phi_s}, \quad \kappa = \sum_s \frac{X_s \kappa_s}{\phi_s} ,$$

where

$$X_s = \frac{c_s M}{M_s}, \quad M = \left(\sum_s \frac{c_s}{M_s} \right)^{-1} ,$$

$$\phi_s = \sum_r X_r \left[1 + \sqrt{\frac{\mu_s}{\mu_r}} \left(\frac{M_r}{M_s} \right)^{1/4} \right]^2 \left[\sqrt{8 \left(1 + \frac{M_s}{M_r} \right)} \right]^{-1} ,$$

and $c_s = \rho_s / \rho$ is the mass fraction of species s . The model of Blottner is used for the species viscosities μ_s , which are calculated from curve fits of the form

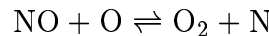
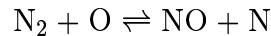
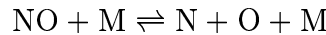
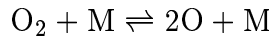
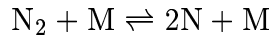
$$\mu_s = 0.1 \exp[(A_s \ln T + B_s) \ln T + C_s] ,$$

where A_s , B_s , and C_s are constants given in the appendix. This model is valid for a large range of temperature (to about 10,000 K), and is suitable for this work.

2.6 The Chemical Source Terms

Each of the source terms w_s that appear in the mass conservation equations represents the rate of production and destruction of species s due to chemical reactions. In this section we present the chemical source terms that appear in the mass conservation equations.

In the high enthalpy flows that we examine in this work, two different gases are used: nitrogen and air. The treatment of nitrogen can be considered as a special case of the air gas, and thus the set of conservation equations for nitrogen flows is a subset of the equation set that describes air flows. For high temperature air with no ionization, there are five chemical reactions that are important, involving five species: N₂, O₂, NO, N, and O. The chemical reactions involved are



The reactions are presented so that they are endothermic in the forward direction. The first three reactions represent dissociation of the diatomic species N₂, O₂, and NO due to collisions. In these reactions, M is arbitrary and represents the collision partner which provides the energy to break the chemical bond. The three corresponding reverse reactions are three-body recombination, during which the collision

partner M absorbs the energy released during the formation of chemical bonds. The two remaining reactions are the Zeldovich exchange reactions, which are the primary source of nitric oxide (NO) in a hypersonic flow.

The rates of the forward and backward reactions take an Arrhenius form governed by the forward and backward rate coefficients k_{fr_m} and k_{br_m} respectively. We may write the rate of each reaction as a sum of the forward and backward rates

$$\begin{aligned}\mathcal{R}_1 &= \sum_m \left[k_{b1m} \frac{\rho_N}{M_N} \frac{\rho_N}{M_N} \frac{\rho_m}{M_m} - k_{f1m} \frac{\rho_{N_2}}{M_{N_2}} \frac{\rho_m}{M_m} \right] \\ \mathcal{R}_2 &= \sum_m \left[k_{b2m} \frac{\rho_O}{M_O} \frac{\rho_O}{M_O} \frac{\rho_m}{M_m} - k_{f2m} \frac{\rho_{O_2}}{M_{O_2}} \frac{\rho_m}{M_m} \right] \\ \mathcal{R}_3 &= \sum_m \left[k_{b3m} \frac{\rho_N}{M_N} \frac{\rho_O}{M_O} \frac{\rho_m}{M_m} - k_{f3m} \frac{\rho_{NO}}{M_{NO}} \frac{\rho_m}{M_m} \right] \\ \mathcal{R}_4 &= k_{b4} \frac{\rho_{NO}}{M_{NO}} \frac{\rho_N}{M_N} - k_{f4} \frac{\rho_{N_2}}{M_{N_2}} \frac{\rho_O}{M_O} \\ \mathcal{R}_5 &= k_{b5} \frac{\rho_{O_2}}{M_{O_2}} \frac{\rho_N}{M_N} - k_{f5} \frac{\rho_{NO}}{M_{NO}} \frac{\rho_O}{M_O}\end{aligned}$$

The chemical source terms can now be expressed in terms of the individual reaction rates

$$\begin{aligned}w_{N_2} &= M_{N_2} (\mathcal{R}_1 + \mathcal{R}_4) \\ w_{O_2} &= M_{O_2} (\mathcal{R}_2 - \mathcal{R}_5) \\ w_{NO} &= M_{NO} (\mathcal{R}_3 - \mathcal{R}_4 + \mathcal{R}_5) \\ w_N &= M_N (-2\mathcal{R}_1 - \mathcal{R}_3 - \mathcal{R}_4 - \mathcal{R}_5) \\ w_O &= M_O (-2\mathcal{R}_2 - \mathcal{R}_3 + \mathcal{R}_4 + \mathcal{R}_5)\end{aligned}$$

We note that the sum of all the source terms is identically zero, so that conservation of total mass is satisfied, and elemental conservation of atomic nitrogen and oxygen is also satisfied.

The forward and backward reaction rate coefficients are in general affected by the level of thermal nonequilibrium in the flow. In this work we use the model of Park (1986) for vibration-dissociation coupling. The Park model has been used extensively, since it is simple to implement and has been shown to give satisfactory results for a variety of flow conditions [Olejniczak (1997)]. The Park model assumes

that the reaction rates are functions of an effective temperature, and therefore we represent the forward reaction rate coefficients by the modified Arrhenius form

$$k_{f_m} = C_{f_m} T_{\text{eff}}^{\eta_m} \exp(-\theta_m/T_{\text{eff}}) ,$$

where C_{f_m} , η_m , and θ_m are found from curve fits to experimental data. In this work, the values recommended by Park (1988) are used. The coefficients are given in the appendix. The effective temperature T_{eff} that appears in the expression is some function of the translational-rotational and vibrational temperatures. Park recommends that the geometric average of the translational and vibrational temperatures is used for the forward rates of the dissociation reactions, as

$$T_{\text{eff}} = \sqrt{T T_v} .$$

The backward reaction rate coefficients are related to the forward reaction rate coefficients through the equilibrium constant defined as their ratio

$$K_{\text{eq}_m}(T) = \frac{k_{f_m}(T_{\text{eff}})}{k_{b_m}} .$$

The equilibrium constant, K_{eq} , is also a curve fit to experimental data, and is a function only of T

$$K_{\text{eq}_m} = C_m \exp(A_{1m} + A_{2m}Z + A_{3m}Z^2 + A_{4m}Z^3 + A_{5m}Z^4) ,$$

where $Z = 10,000/T$. The constants that appear in the expression for K_{eq_m} are given by Park (1985), and are included in the appendix.

2.7 Vibrational Energy Source Term

The source term that appears on the right hand side of the vibrational energy equation (w_v) is presented here. This source term is due to the exchange of energy between the translational-rotational and vibrational modes of the gas. Additionally, the creation of diatomic molecules, due to recombination reactions, contributes to the vibrational energy source term.

There are many energy exchange mechanisms between the different internal energy modes of the gas, including exchange between translational and vibrational modes, exchange between rotational and vibrational modes, and exchange between vibrational modes of the separate species. In this work, we have assumed that the vibration-vibration exchanges are very fast, and thus the vibrational modes of the gas are in equilibrium at the same vibrational temperature T_v . The vibration-translation and vibration-rotation energy exchange rates are combined in a single energy exchange rate Q_{t-v} , and the Landau-Teller model is used [Vincenti and Kruger (1986)]. The energy exchange rate is given as

$$Q_{t-v}^{(LT)} = \rho_s \frac{e_{v_s}^* - e_{v_s}}{\langle \tau_s \rangle} ,$$

where $e_{v_s}^*$ is the vibrational energy per unit mass of species s evaluated at the translational temperature (equilibrium), and $\langle \tau_s \rangle$ is the molar averaged Landau-Teller relaxation time, and is given by Lee (1985) as

$$\langle \tau_s \rangle = \frac{\sum_r X_r}{\sum_r X_r / \tau_{sr}} ,$$

where X_r has been defined previously and τ_{sr} is Landau-Teller inter-species relaxation time given by Millikan and White (1963), as

$$\begin{aligned} \tau_{sr} &= \frac{1}{p} \exp[A_{sr}(T^{-1/3} - 0.015\mu_{sr}^{1/4}) - 18.42] , \quad (p \text{ in atm}) \\ A_{sr} &= 1.16 \times 10^{-3} \mu_{sr}^{1/2} \theta_{v_s}^{4/3}, \\ \mu_{sr} &= \frac{M_s M_r}{M_s + M_r} . \end{aligned}$$

Part of the vibrational energy source terms is due to the creation and destruction of diatomic species in chemical reactions. For this work, we assume that the molecules that are recombining and molecules that dissociate carry vibrational energy given by the local vibrational temperature. Therefore, the rate of production of vibrational energy due to chemical reactions is just

$$Q_{v_s} = w_s e_{v_s} .$$

The vibrational energy source term w_s is simply the sum of the contributions of the two processes, namely recombination and translation-vibration energy exchange, and is given by

$$w_v = \sum_{s=1}^{nd} Q_{t-v}^{(LT)} s + \sum_{s=1}^{nd} w_s e_{vs} .$$

2.8 Boundary Conditions

In this work, we use slip and no-slip velocity boundary conditions at the wall. We impose either isothermal wall conditions, or we allow the internal modes of the gas to "slip" (or "jump") at the wall, based on the phenomenological model approach of Gökçen (1989). The standard Maxwell model [Schaaf & Chambre, (1966) pp. 34-35] for velocity slip and temperature jump at the surface of the body is

$$\begin{aligned} v_{t\text{slip}} &= \frac{2 - \sigma}{\sigma} \lambda \left. \frac{\partial v_t}{\partial n} \right|_{\text{wall}} \\ T_{\text{slip}} - T_{\text{wall}} &= \frac{2 - \sigma_T}{\sigma_T} \frac{2\gamma}{(\gamma + 1)Pr} \lambda \left. \frac{\partial T}{\partial n} \right|_{\text{wall}} \end{aligned}$$

where $v_{t\text{slip}}$ and T_{slip} are the tangential velocity and temperature near the surface (the "slip" conditions), T_{wall} is the temperature of the surface, and λ is the mean-free-path. σ and σ_T are the accommodation coefficients and are taken to be 0.85. It should be noted that only the component of the velocity tangential to the surface is allowed to slip when velocity slip conditions are imposed. The component of the bulk velocity normal to the wall is always zero.

We also model the possible jump of vibrational energy at the surface. This is done with a simple extension of the Maxwell model based on the approach of Gökçen (1989). The vibrational energy jump is

$$e_{v\text{slip}} - e_{v\text{wall}} = \frac{2 - \sigma_v}{\sigma_v} \lambda_v \left. \frac{\partial e_v}{\partial n} \right|_{\text{wall}}$$

where σ_v is the accommodation coefficient for vibration and λ_v is the mean-free-path that characterizes transport of vibrational energy. Because the vibrational energy is not correlated with the translational energy modes, we use the value of

mean-free-path for the transport of momentum, namely $\lambda_v = \lambda = 2\mu/\rho\bar{c}$, where $\bar{c} = \sqrt{8RT/\pi}$ is the mean thermal speed of the gas. The value of the vibrational energy accommodation coefficient is not well known, although Meolans *et al.* (2002) suggest adiabatic conditions ($\sigma_v = 0$). Measurements made by Black *et al.* (1974) give different values of σ_v for different materials. The double-cone model used in this work is made of stainless steel, for which they measure values of either $1.0 \pm 0.2 \times 10^{-3}$ or $1.2 \pm 0.3 \times 10^{-3}$. In our calculations, we use 0.5 and 1.0×10^{-3} for σ_v to assess the effect of vibrational energy accommodation, as discussed in chapter 6. Based on theory and measurements the lower value is more accurate.

In general, the wall is assumed to be non-catalytic, which implies that there is zero normal concentration gradient at the wall for all species, and thus the diffusive flux is zero at the wall. Fully catalytic boundary conditions are also employed in certain cases, and we state explicitly when these are used. Assuming that a wall is fully catalytic implies that atomic species recombine at the wall to form molecular oxygen and nitrogen.

Chapter 3

The Numerical Method

3.1 Introduction

In this chapter we present the numerical method we use to solve the coupled partial differential equations that describe the flows of interest. The conservation laws presented in the previous chapter were expressed in their strong form. However, we obtain numerical solutions to this set of conservation equations by considering the weak form of the equations. We use a standard finite volume method to discretize the governing equations in the approximation space.

We introduce the finite volume formulation, and the methods we use to evaluate the inviscid and viscous terms. The implicit method employed for time advancement is also briefly presented. We will restrict the remaining of this chapter to the two-dimensional case in order to simplify the calculations, but it should be noted that it is straightforward to extend the numerical method to three dimensions.

3.2 The Finite Volume Method

In this section, we introduce the finite volume method of discretization. We begin with the strong form of the equations presented in the previous chapter. We write the vector of conserved variables as

$$U = (\rho_1, \dots, \rho_{ns}, \rho u, \rho v, E_v, E)^T ,$$

and the conservation equations can now take the compact form

$$\frac{\partial U}{\partial t} + \nabla \cdot \vec{F} = W ,$$

where \vec{F} is the corresponding total flux vector and W is the vector of source terms

$$W = (w_1, \dots, w_{ns}, 0, 0, w_v, 0)^T .$$

The total flux can be split into the convective (inviscid) and diffusive flux vectors

$$\vec{F} = \vec{F}_I + \vec{F}_v .$$

The Cartesian components of the convective and diffusive flux vectors are

$$F_I = \begin{pmatrix} \rho_1 u \\ \rho_2 u \\ \vdots \\ \rho_{ns} u \\ \rho u u + p \\ \rho v u \\ E_v u \\ (E + p) u \end{pmatrix}, \quad G_I = \begin{pmatrix} \rho_1 v \\ \rho_2 v \\ \vdots \\ \rho_{ns} v \\ \rho u v \\ \rho v v + p \\ E_v v \\ (E + p) v \end{pmatrix},$$

$$F_v = \begin{pmatrix} \rho_1 u_1 \\ \rho_2 u_2 \\ \vdots \\ \rho_{ns} u_{ns} \\ -\tau_{xx} \\ -\tau_{xy} \\ q_{vx} + \sum_{s=1}^{nd} (\rho_s e_{vs} u_s) \\ q_x + q_{vx} - (\tilde{\tau} \vec{u})_x + \sum_{s=1}^{ns} (\rho_s h_s u_s) \end{pmatrix},$$

$$G_v = \begin{pmatrix} \rho_1 v_1 \\ \rho_2 v_2 \\ \vdots \\ \rho_{ns} v_{ns} \\ -\tau_{yx} \\ -\tau_{yy} \\ q_{vy} + \sum_{s=1}^{nd} (\rho_s e_{vs} v_s) \\ q_y + q_{vy} - (\tilde{\tau} \vec{u})_y + \sum_{s=1}^{ns} (\rho_s h_s v_s) \end{pmatrix}.$$

In the finite volume formulation, the weak form of the conservation equations is obtained by integrating over an arbitrary control volume Ω , which, for the purposes of this work, is assumed to be fixed in space. Green's Theorem is applied to convert

the volume integral containing the flux vector, to a surface integral over the surface that encloses Ω . The resulting weak form of the equation is

$$\frac{\partial \bar{U}}{\partial t} + \frac{1}{V} \oint_{\partial\Omega} (\vec{F} \cdot \hat{n}) dS = \bar{W},$$

where V is the total volume, \hat{n} is the outward-pointing normal to the surface, and \bar{U} , \bar{W} are averaged over Ω . We discretize physical space by dividing it into a series of volume elements, which can be arbitrary polygons. We do this by building a regular mesh over the domain of interest, resulting in a structured grid. The grid directions are defined such that i index increases in the ξ -direction and j increases in the positive η -direction. Each of the volume elements in the two-dimensional domain is a quadrilateral, and represents a cell in computational space. Flow variables are stored at the cell centers rather than the nodes. Quantities at the cell faces are computed from the solution reconstruction based on the cell-centered data. The time rate of change of \bar{U} in the 2-D volume element i,j is represented as a sum of the fluxes over the four cell faces and the generation of U within the volume

$$\begin{aligned} \frac{\partial \bar{U}_{i,j}}{\partial t} = & -\frac{1}{V_{i,j}} \left[(\vec{F} \cdot \hat{n})_{i+\frac{1}{2},j} S_{i+\frac{1}{2},j} - (\vec{F} \cdot \hat{n})_{i-\frac{1}{2},j} S_{i-\frac{1}{2},j} \right. \\ & \left. + (\vec{F} \cdot \hat{n})_{i,j+\frac{1}{2}} S_{i,j+\frac{1}{2}} - (\vec{F} \cdot \hat{n})_{i,j-\frac{1}{2}} S_{i,j-\frac{1}{2}} \right] + \bar{W}_{i,j}. \end{aligned}$$

The $\pm 1/2$ indices on the flux and surface area terms indicate that quantities should be evaluated at the appropriate cell face. This expression is the discretized form of the conservation equations for a two-dimensional domain. The extension of the formulation to three dimensions, where the volume elements are hexahedra, is straightforward and results in an analogous expression. The axisymmetric formulation, however, is non-trivial, and ultimately yields an expression similar to that of the two-dimensional case. Integrating the conservation equations over an axisymmetric domain introduces extra terms that appear as sources in the forcing vector W . The details of the calculation are included in the appendix.

3.3 Evaluation of the Fluxes

In this section we present the methods we use for evaluating the fluxes that

appear on the right hand side of the discretized form of the conservation equations. We have decomposed the fluxes into the convective part (which consists of the advection terms and the pressure) and diffusive part. This decomposition is useful because we treat the convective and diffusive fluxes differently. The inviscid terms make the system of equations hyperbolic, while the viscous terms are diffusive in nature, and make the system parabolic when combined with the transient term. This complicates the evaluation of the right hand side of the conservation equations. The elliptic nature of the diffusive terms allows for a simple central difference scheme to be used [Hirsch (1991)]. A more sophisticated approach is necessary for the calculation of the inviscid terms, in order to maintain stability of the numerical scheme.

In the computation of the inviscid terms, we make use of the fact that in hyperbolic systems of equations, information propagates along definable characteristic directions in space-time. This is commonly referred to as upwind biasing. We employ a modified form of the Steger-Warming (1981) flux-vector splitting, a method widely used due to its robustness, which is based on characteristic theory. We present the application of this method specifically to the set of conservation equations relevant to this work (see also Wright (1997)), but it should be noted that the method has been implemented for more complex sets of conservation equations.

We consider the inviscid flux through a face

$$F'_I = \vec{F}_I \cdot \hat{n} = \begin{pmatrix} \rho_1 u' \\ \rho_2 u' \\ \vdots \\ \rho_{ns} u' \\ \rho u u' + p s'_x \\ \rho v u' + p s'_y \\ E_v u' \\ (E + p) u' \end{pmatrix}$$

where s'_x, s'_y are the components of the unit vector normal to the surface in question, and u' is the component of the velocity normal to the surface. We observe that the

flux F'_I is linear and homogeneous in the vector of conserved variables U , i.e.,

$$F'_I(\lambda U) = \lambda F'_I(U) ,$$

where λ is an arbitrary scalar. This can be shown if we express the inviscid flux F'_I in terms of the components of U . The homogeneity of the flux allows us to express it exactly in terms of the linearization

$$F'_I(U) = \frac{\partial F'_I}{\partial U} U = A' U ,$$

where A' is the inviscid flux Jacobian matrix in the direction of \hat{n} . We follow the approach of Steger and Warming to split the inviscid fluxes into positively-moving and negatively-moving components using an upwind biasing scheme. The partitioning is performed by diagonalizing A' , and the fluxes are split according to the sign of the eigenvalues of the Jacobian. The diagonalization of $\frac{\partial F'_I}{\partial U}$ is rather cumbersome, but we can simplify the operation by breaking the Jacobian into components, as

$$A' = \frac{\partial U}{\partial V} \frac{\partial V}{\partial U} \frac{\partial F'_I}{\partial V} \frac{\partial V}{\partial U} ,$$

where V is a vector of primitive variables, introduced for convenience. The choice of V is not unique, but for the particular inviscid fluxes it is convenient to use

$$V = (\rho_1, \rho_2, \dots, \rho_{ns}, u, v, e_v, p)^T ,$$

where e_v is the total vibrational energy per unit mass. The transformation matrices between primitive and conservative variables are denoted by S^{-1} and S , which are given in the appendix. We should, in principle, be able to diagonalize using a similarity transformation

$$\frac{\partial V}{\partial U} \frac{\partial F'_I}{\partial V} = C_{A'}^{-1} \Lambda_{A'} C_{A'} ,$$

where $\Lambda_{A'}$ is a diagonal matrix of eigenvalues, $C_{A'}^{-1}$ is the matrix of eigenvectors of A' , and $C_{A'}$ such that $C_{A'}^{-1}C_{A'} = I$. The diagonalization process has now been simplified, however the resulting expressions for the eigenvectors, although mathematically correct, may exhibit singularities and are not suitable for use in a numerical algorithm. Therefore, we introduce an orthogonal transformation R , which transforms the momenta from a coordinate system locally aligned with the face in question, to the Cartesian system. We can now write the Jacobian matrix as

$$A' = S^{-1}R^{-1}C_A^{-1}\Lambda_{A'}C_AR S ,$$

where C_A , R and their inverses are given in the appendix. The diagonal components of $\Lambda_{A'}$ are the convection speeds of the characteristic variables. The flux vector can now be split into the positively and negatively moving components defined by

$$\begin{aligned} F'_+ &= S^{-1}R^{-1}C_A^{-1}\Lambda_+C_AR S U = A'_+U \\ F'_- &= S^{-1}R^{-1}C_A^{-1}\Lambda_-C_AR S U = A'_-U , \end{aligned}$$

where Λ_+ and Λ_- are the split eigenvalue matrices consisting of the positive and negative eigenvalues respectively. The total inviscid flux vector through the face in question can be expressed as the sum of positively and negatively moving components

$$F'_I = F'_+ + F'_- .$$

In this basic discretization, the split fluxes at each cell face are evaluated using

$$\begin{aligned} F'_{+i+\frac{1}{2},j} &= A'_{+i,j}U_{i,j} , \\ F'_{-i+\frac{1}{2},j} &= A'_{-i+1,j}U_{i+1,j} , \end{aligned}$$

where A'_{\pm} and U are evaluated based on the upwind cell data. MacCormack and Candler (1989) proposed a modification to this method, which reduces the amount of numerical dissipation of the original method. Their modification suggests that the Jacobian matrix should be evaluated at the cell face, rather than using the upwind cell data. This approach works well in regions of weak gradients, but additional

dissipation is required to capture strong gradients and shock waves. In this work, we use a hybrid method, in which we use pressure weighted average quantities between adjacent cells to evaluate the Jacobian. The method smoothly switches from modified to true Steger-Warming in regions of large pressure gradients. This flux evaluation method as originally formulated is only first order accurate in space, however it is possible to achieve higher order of accuracy. Higher order accurate schemes can produce more resolved solutions on a given computational mesh. We use up to second order accurate fluxes in this work. We obtain higher order of accuracy by extrapolating the conserved variables to the cell face based on the purely upwind cell data. We detect the presence of shock waves by identifying pressure jumps greater than 50% of the smallest pressure involved in the flux evaluation stencil, in which case we switch the stencil to first order. For the details of this formulation see Druguet *et al.* (2003).

If we substitute the split fluxes into the discretized form of the conservation equations, we get the upwind finite volume formulation of the inviscid equations

$$\begin{aligned} \frac{\partial \bar{U}_{i,j}}{\partial t} = & -\frac{1}{V_{i,j}} \left[(A'_{+i+\frac{1}{2},j} S_{i+\frac{1}{2},j} U_{i,j} - A'_{+i-\frac{1}{2},j} S_{i-\frac{1}{2},j} U_{i-1,j}) \right. \\ & - (A'_{-i-\frac{1}{2},j} S_{i-\frac{1}{2},j} U_{i,j} - A'_{-i+\frac{1}{2},j} S_{i+\frac{1}{2},j} U_{i+1,j}) \\ & + (B'_{+i,j+\frac{1}{2}} S_{i,j+\frac{1}{2}} U_{i,j} - B'_{+i,j-\frac{1}{2}} S_{i,j-\frac{1}{2}} U_{i,j-1}) \\ & \left. - (B'_{-i,j-\frac{1}{2}} S_{i,j-\frac{1}{2}} U_{i,j} - B'_{-i,j+\frac{1}{2}} S_{i,j+\frac{1}{2}} U_{i,j+1}) \right] + \bar{W}_{i,j} , \end{aligned}$$

where we have implicitly defined A' and B' to denote the inviscid flux Jacobians in the ξ and η directions respectively.

The elliptic nature of the viscous fluxes makes their evaluation possible with a simple finite difference scheme. The viscous flux vector is evaluated at the required cell faces using central differencing. The viscous fluxes integrated over a face take the simple form

$$\begin{aligned} F'_{v i+\frac{1}{2},j} S_{i+\frac{1}{2},j} &= (\vec{F}_v \cdot \hat{n})_{i+\frac{1}{2},j} S_{i+\frac{1}{2},j} \\ G'_{v i,j+\frac{1}{2}} S_{i,j+\frac{1}{2}} &= (\vec{F}_v \cdot \hat{n})_{i,j+\frac{1}{2}} S_{i,j+\frac{1}{2}} . \end{aligned}$$

The contribution of the viscous fluxes is summed over the four cell faces and added to the right hand side of the discretized form of the conservation equations. The required derivatives that appear in the viscous fluxes are taken with respect to the general curvilinear coordinate system ξ - η , and are then transformed to the Cartesian system. The calculation of these terms can be found in Hirsch (1991).

3.4 Time Advancement

In this section we discuss how the solution is integrated in time to its steady state. We are interested solely in the steady state solution, if one exists, and thus time accuracy is not important for our computations. Therefore, we employ an implicit method, which allows for large time steps to be taken, while maintaining stability of the numerical scheme. We give a short description of the implicit formulation here. We first introduce the explicit method of solution, and then we extend it to the implicit formulation.

We discretize the transient term that appears in the conservation equations, in order to time-march the solution toward the steady state. We use simple first-order Euler backward differencing, in which the time derivative becomes

$$\frac{\partial U_{i,j}}{\partial t} = \frac{U_{i,j}^{n+1} - U_{i,j}^n}{\Delta t} + \mathcal{O}(\Delta t^2) \simeq \frac{\Delta U_{i,j}^n}{\Delta t}$$

and the superscript denotes the time level in the temporal discretization. This expression is substituted directly into the discretized form of the conservation equations, and the solution is marched forward in time by discrete time steps. The explicit formulation of the inviscid problem is

$$\begin{aligned} \Delta U_{i,j}^n = & -\frac{\Delta t}{V_{i,j}} \left[(A'_{+i+\frac{1}{2},j} S_{i+\frac{1}{2},j} U_{i,j} - A'_{+i-\frac{1}{2},j} S_{i-\frac{1}{2},j} U_{i-1,j}) \right. \\ & - (A'_{-i-\frac{1}{2},j} S_{i-\frac{1}{2},j} U_{i,j} - A'_{-i+\frac{1}{2},j} S_{i+\frac{1}{2},j} U_{i+1,j}) \\ & + (B'_{+i,j+\frac{1}{2}} S_{i,j+\frac{1}{2}} U_{i,j} - B'_{+i,j-\frac{1}{2}} S_{i,j-\frac{1}{2}} U_{i,j-1}) \\ & \left. - (B'_{-i,j-\frac{1}{2}} S_{i,j-\frac{1}{2}} U_{i,j} - B'_{-i,j+\frac{1}{2}} S_{i,j+\frac{1}{2}} U_{i,j+1}) \right]^n + \Delta t W_{i,j}^n , \end{aligned}$$

where $\Delta U_{i,j}^n$ is the explicit change in the solution vector (residual) at cell i,j at time step n . The solution is updated to the next time level using

$$U_{i,j}^{n+1} = U_{i,j}^n + \Delta U_{i,j}^n .$$

We call this an explicit method because the solution in the next time level $n+1$, is computed explicitly by evaluating the right hand side at the current time level n . The solution at any point at time level $n+1$ is independent of the solution at other points at the same time level.

With a fully implicit method, the time-step limitations inherent to explicit solvers can be overcome. The use of an implicit solver can allow, in general, for time steps much larger than the stable explicit time step. In an implicit method, the solution at any point depends on the solution of all other points at the time level $n+1$. Therefore, in order to employ implicit time advancement, it is necessary to evaluate the right hand side of the conservation equations at time level $n+1$. We express the fluxes that appear on the right hand side in terms of the linearization

$$\begin{aligned} F_I'^{n+1} &= F_I'^n + \frac{\partial F_I'}{\partial U} \Big|_n (U^{n+1} - U^n) + \mathcal{O}(\Delta t^2) \\ &\simeq F_I'^n + A'^n \delta U^n \end{aligned}$$

where we have defined the vector $\delta U^n = U^{n+1} - U^n$ and we have frozen the variation of the inviscid flux Jacobian A'^n between time steps. We apply this linearization to the split fluxes and source vector to obtain the fully implicit upwind formulation of the inviscid problem

$$\begin{aligned} \delta U_{i,j}^n + \frac{\Delta t}{V_{i,j}} &\left[(A'_{+i+\frac{1}{2},j} S_{i+\frac{1}{2},j} \delta U_{i,j} - A'_{+i-\frac{1}{2},j} S_{i-\frac{1}{2},j} \delta U_{i-1,j}) \right. \\ &- (A'_{-i-\frac{1}{2},j} S_{i-\frac{1}{2},j} \delta U_{i,j} - A'_{-i+\frac{1}{2},j} S_{i+\frac{1}{2},j} \delta U_{i+1,j}) \\ &+ (B'_{+i,j+\frac{1}{2}} S_{i,j+\frac{1}{2}} \delta U_{i,j} - B'_{+i,j-\frac{1}{2}} S_{i,j-\frac{1}{2}} \delta U_{i,j-1}) \\ &\left. - (B'_{-i,j-\frac{1}{2}} S_{i,j-\frac{1}{2}} \delta U_{i,j} - B'_{-i,j+\frac{1}{2}} S_{i,j+\frac{1}{2}} \delta U_{i,j+1}) \right]^n \\ &- \Delta t C_{i,j}^n \delta U_{i,j}^n = \Delta U_{i,j}^n , \end{aligned}$$

where $C_{i,j}^n$ is the Jacobian of W with respect to U . In this implicit equation, $\Delta U_{i,j}^n$ is the explicit residual as defined previously.

We include the implicit approximation of the viscous terms in the implicit equation by applying the linearization to the viscous fluxes. We define $\delta F_v'^n$ and $\delta G_v'^n$ such that

$$\begin{aligned} F_v'^{n+1} &= F_v'^n + \delta F_v'^n \\ G_v'^{n+1} &= G_v'^n + \delta G_v'^n . \end{aligned}$$

Therefore, we only need to find expressions for $\delta F_v'$ and $\delta G_v'$. We note that F_v' and G_v' are functions of U and its spatial derivatives. The derivatives are taken with respect to the general curvilinear coordinate system, and then transformed to the Cartesian system using the operators

$$\frac{\partial}{\partial x} = \frac{\partial \xi}{\partial x} \frac{\partial}{\partial \xi} + \frac{\partial \eta}{\partial x} \frac{\partial}{\partial \eta}, \quad \frac{\partial}{\partial y} = \frac{\partial \xi}{\partial y} \frac{\partial}{\partial \xi} + \frac{\partial \eta}{\partial y} \frac{\partial}{\partial \eta} .$$

We apply the thin-layer assumption to the derivatives in the implicit viscous terms. In this way, we selectively retain derivatives depending on which viscous flux we wish to approximate. For example, in the approximation of $\delta G_v'$ we compute the derivatives by

$$\frac{\partial}{\partial x} \simeq \frac{\partial \eta}{\partial x} \frac{\partial}{\partial \eta}, \quad \frac{\partial}{\partial y} \simeq \frac{\partial \eta}{\partial y} \frac{\partial}{\partial \eta} .$$

Similarly, derivatives with respect to ξ are retained when approximating $\delta F_v'$. If we assume that the terms not involving derivatives are locally constant, we can write F_v' and G_v' as a function of the derivatives of the flow variables with respect to ξ or η only, as

$$\delta F_v' = M_\xi \frac{\partial}{\partial \xi}(\delta \mathbf{V}), \quad \delta G_v' = M_\eta \frac{\partial}{\partial \eta}(\delta \mathbf{V}),$$

and we introduce for convenience the vector of non-conserved variables

$$\mathbf{V} = (c_1, c_2, \dots, c_{ns}, u, v, e_v, T)^T .$$

The matrices M_ξ and M_η are given in the appendix. We ultimately express the implicit viscous fluxes in terms of δU by mapping from $\delta \mathbf{V}$ to δU using the Jacobian $N = \frac{\partial \mathbf{V}}{\partial U}$, and we obtain the final form

$$\delta F'_v = M_\xi \frac{\partial}{\partial \xi} (N \delta U) , \quad \delta G'_v = M_\eta \frac{\partial}{\partial \eta} (N \delta U) ,$$

We should emphasize here that all of the viscous derivatives are retained in the computation of F'_v^n and G'_v^n , and thus all of the viscous terms influence the converged solution. With this treatment of the viscous terms, the implicit equation for the inviscid problem away from solid boundaries will be unchanged if we simply replace the inviscid Jacobians A' and B' with \tilde{A} and \tilde{B} , where.

$$\begin{aligned} \tilde{A}_+ &= A_+ - M_\xi N & \tilde{A}_- &= A_- + M_\xi N \\ \tilde{B}_+ &= B_+ - M_\eta N & \tilde{B}_- &= B_- + M_\eta N \end{aligned}$$

The implicit formulation involves the solution of a linear system of equations, which has a strong diagonal dominance due to the nature of the Steger-Warming Jacobians. In principle, we can solve exactly for the $\delta U_{i,j}^n$ by a direct inversion of the operator.

3.5 The Data-Parallel Line-Relaxation

In this section we briefly present the method of solution of the implicit equation. We use the Data-Parallel Line Relaxation method of Wright *et al.* (1998). This method was developed to take advantage of parallel computing machines, and appears to be superior to other implicit methods [Wright (1997)]. Only a brief description of this method is given here. Details on the performance of the method can be found in Wright (1997) and Wright *et al.* (1998).

The standard implicit upwind formulation of the Navier-Stokes equations for a reacting gas is essentially a linear system of equations. The solution of such system can, in principle, be obtained directly by inversion of a large block banded matrix. This becomes very computationally intensive, as such an inversion must be performed at every time step until convergence is achieved. Therefore, most

implicit methods seek to make simplifications in order to make the solution of the problem less expensive. Such simplifications are possible only on the left-hand side of the equations, which resembles the *numerics*. The right-hand side of the equation (residual) should be unaltered.

It is convenient to introduce some additional notation in order to group terms on the left-hand side of the implicit equation. We let

$$\begin{aligned}\hat{A}_{i,j} &= \frac{V_{i,j}}{\Delta t} I + \left(A'^n_{+i+\frac{1}{2},j} S_{i+\frac{1}{2},j} - A'^n_{-i-\frac{1}{2},j} S_{i-\frac{1}{2},j} \right. \\ &\quad \left. + B'^n_{+i,j+\frac{1}{2}} S_{i,j+\frac{1}{2}} - B'^n_{-i,j-\frac{1}{2}} S_{i,j-\frac{1}{2}} \right) - V_{i,j} C^n_{i,j} \\ \hat{B}_{i,j} &= B'^n_{-i,j+\frac{1}{2}} S_{i,j+\frac{1}{2}} \\ \hat{C}_{i,j} &= B'^n_{+i,j-\frac{1}{2}} S_{i,j-\frac{1}{2}} \\ \hat{D}_{i,j} &= A'^n_{-i+\frac{1}{2},j} S_{i+\frac{1}{2},j} \\ \hat{E}_{i,j} &= A'^n_{+i-\frac{1}{2},j} S_{i-\frac{1}{2},j}.\end{aligned}$$

We can simplify the operator if we assume that the physical problem is strongly coupled in the η direction. Then, we can move some of the off-diagonal terms to the right-hand side of the implicit equation, keeping only constant i terms on the left-hand side. In this way, it is possible to solve for all j points at each i location as a series of fully coupled block tri-diagonal systems aligned in the η direction. We relax the off-diagonal terms by updating the unknowns on the right-hand side of the equation with the $\delta U_{i,j}$ we have just computed. We do not need to obtain an exact solution to the implicit equation, but rather to maintain stability, and thus only a few iterations are required per time step. The solution procedure is as follows. First, the implicit terms on the right-hand side are neglected and the resulting block tri-diagonal system is factored and solved for $\delta U^{(0)}$ according to:

$$\hat{B}_{i,j} \delta U_{i,j+1}^{(0)} + \hat{A}_{i,j} \delta U_{i,j}^{(0)} - \hat{C}_{i,j} \delta U_{i,j-1}^{(0)} = \Delta U_{i,j}^n$$

where the superscript denotes the sub-iteration number (zero denotes the initialization). Then, a series of k_{max} relaxation steps is performed, where we solve

$$\hat{B}_{i,j} \delta U_{i,j+1}^{(k)} + \hat{A}_{i,j} \delta U_{i,j}^{(k)} - \hat{C}_{i,j} \delta U_{i,j-1}^{(k)} = -\hat{D}_{i,j} \delta U_{i+1,j}^{(k-1)} + \hat{E}_{i,j} \delta U_{i-1,j}^{(k-1)} + \Delta U_{i,j}^n,$$

and the superscript $k - 1$ indicates that data from the previous relaxation step is used. Finally, the solution is obtained by

$$\delta U_{i,j}^{n+1} = \delta U_{i,j}^{(k_{max})}.$$

There are two advantages to this method of solution. First, the method can be implemented efficiently on a distributed memory parallel computer. This is because we can split the problem among processors in the i direction, effectively assigning a series of i -columns to each processor. Therefore, each relaxation step can be performed simultaneously as there are no data dependencies, while the boundary data can be efficiently transferred. Secondly, there is no bias in the solution procedure, which has been shown to impose a bias in the solution itself.

3.6 Boundary Conditions

In this section we describe the boundary conditions used for both the explicit residual and the implicit operator, and how they are implemented in the numerical algorithm.

In the finite volume method, explicit boundary conditions are imposed using “dummy” cells. An extra layer of cells is included around the grid that represents physical space, in which variables are stored in order to impose the appropriate boundary conditions for the problem. The dummy cells are constructed in such a way that derivatives taken in terms of the curvilinear body-fitted coordinate system are consistent with the type of boundary condition of the viscous fluxes. Because we split the fluxes into the viscous and inviscid parts, we treat the boundary conditions separately.

In the explicit formulation, we simulate no-slip conditions by setting the velocity at the wall to zero, and extrapolating the velocity components at the boundary cell $i,1$ based on the values at the cell $i,2$. We simulate isothermal wall conditions in a similar fashion. The slip conditions require that we have a model for how the velocity component tangent to the wall is computed based on the interior values.

The details of the model employed were presented in chapter 2. Once the slip velocity has been determined, we extrapolate values to the dummy cells, as we did for the no-slip case. We impose internal energy jumps at the wall in exactly the same fashion. The non-catalicity of the wall is imposed by setting the values of the species densities at the dummy cells equal to the interior values, effectively imposing a zero mass-fraction gradient. Similarly, fully catalytic boundary conditions are imposed by extrapolating mass-fractions to the dummy cell assuming the mass-fractions of atomic species is zero at the wall. Subsequently, the mass flux of polyatomic species at the wall is corrected such that we have elemental conservation during this process.

The implicit treatment of the boundary conditions is analogous to that of the explicit method. In the implicit formulation, however, it is not the variables at dummy cells that are set to a certain value, but their effect on the implicit operator which we construct. Specifically, the boundary conditions are folded into the implicit operator by making a modification to the $\hat{A}_{i,j}$ matrix where appropriate. For example, the inviscid boundary conditions at the wall are included by adding the matrix $\hat{C}_{i,2}E_w$ to $\hat{A}_{i,2}$, where $\hat{C}_{i,j}$ was defined previously, and E_w is an operator that reflects the momentum normal to the wall and is given in the appendix. Similarly, the approximate implicit viscous Jacobian M_η is modified at solid boundaries. The details of the implicit treatments of boundaries are described in Candler (1988) and Gökçen (1989). Note that the viscous wall implicit boundary conditions are folded into the block matrix $\hat{A}_{i,2}$ and should not be included in $\hat{C}_{i,2}$.

3.7 Other Flux Evaluation Methods

The inviscid flux evaluation method discussed earlier is one of many methods suitable for gasdynamic simulations. There are several methods used widely in numerical algorithms, and these are of variable degree of sophistication and complexity. Different flux evaluation methods exhibit different properties in terms of accuracy and computational cost. Most importantly, the amount of numerical dissipation that is associated with a numerical scheme depends largely on the choice

of flux evaluation and solution reconstruction methods. In general, a scheme with little numerical dissipation produces more accurate results on a given computational mesh.

It is beyond the scope of this work to make comparisons between different flux evaluations methods. However, it is important to assess how well the numerical method of choice performs in comparison with other methods. Therefore, chapter 5 discusses in more detail results of simulations made using several other methods of evaluating the inviscid fluxes. These flux evaluation methods are not covered in great detail, and are only presented briefly.

3.8 Second Order Spatial Accuracy

Higher order accurate inviscid fluxes can be obtained through appropriate reconstruction of the solution using cell-centered data. Based on the choice of the reconstruction method, the accuracy of the inviscid fluxes may differ. In this section, we briefly present the methods used in this work.

The flux evaluation method discussed previously is first order accurate when data from adjacent cells are used to calculate the flux. The method can become second order accurate with a simple modification. Consider the Steger-Warming flux for the inviscid equations in one spatial dimension:

$$F = F_+(U_i) + F_-(U_{i+1}) .$$

In this form, the split fluxes use upwind data from adjacent cells. A higher order numerical flux H may be obtained if we replace the arguments of F_+ and F_- with a left state U^L and a right state U^R as:

$$\begin{aligned} H &= F_+(U^L) + F_-(U^R) \\ &= A_+U^L + A_-U^R , \end{aligned}$$

where U^L and U^R are extrapolated conserved quantities based on pure upwind data. It should be noted that this simple extrapolation is not suitable for regions of the flow that exhibits large gradients in U , such as shock waves. Therefore, we

need to detect the presence of a shock, and use no extrapolation in that case. Our implementation uses pressure jumps across cell faces in order to detect the presence of shocks, as discussed earlier.

The MUSCL variable extrapolation method may also be used to construct higher order Steger-Warming and modified Steger-Warming fluxes. In this case, the left and right states U^L , U^R are constructed based on non-linear functions of the ratio of adjacent slopes of U computed based on cell-centered data. Details on slope limiters and their use in the MUSCL variable extrapolation can be found in Hirsch (1991) and Laney (1998).

Chapter 4

Low Enthalpy Double-Cone Experiments

4.1 Introduction

In this chapter we present simulations of double-cone experiments performed at low enthalpy conditions, and we show *blind* comparisons between the experimental measurements and numerical predictions. The term *blind* implies that there was no prior knowledge of the measurements obtained experimentally when the simulations were performed. The experimentalists had not released the results before the simulations were completed, and only the free-stream conditions and the model geometry specification were provided. In this chapter, we also briefly describe how the experiments were performed, and give a short description of the experimental facility.

The experiments were part of a blind validation exercise, that was conducted under the auspices of the NATO Research and Technology Organization (RTO) Working Group 10 [Holden *et al.* (2001) & Harvey *et al.* (2001)]. This exercise was part of a large coordinated effort by the working group to assess the ability of popular CFD codes to reproduce hypersonic flows that closely resemble what is encountered during actual flight. This effort is based on a *building block* approach, where different aspects of the simulation are tested and validated progressively. In particular, the numerical methods and the ability of simulations to accurately reproduce complex shock interaction phenomena in essentially perfect-gas flows were investigated first. Then, depending on the outcome of the first step, more complex hypersonic flow phenomena requiring modeling of physical processes were examined. One of the objectives of the working group was to build a database of experimental

measurements for flows that exhibit various physical phenomena – such as high enthalpy effects and turbulence – along with *benchmark* numerical predictions by continuum and particle-based methods. The low enthalpy experiments presented here are part of validation efforts focusing on the numerical aspect of simulations, and aim to address issues of numerical accuracy versus computational cost.

4.2 Low Enthalpy LENS Experiments

The experiments presented in this section are of hypersonic flows of nitrogen over a 25°-55° double-cone at free-stream specific enthalpies of about 3.5 MJ/kg and nominal Mach numbers of about 10. The experiments were performed in the Large Energy National Shock tunnel (LENS) facility at Calspan - University at Buffalo Research Center (CUBRC), using the LENS Leg I reflected shock tunnel. The tunnel consists of a shock tube connected to a hypersonic nozzle leading to the test-section. A diaphragm divides the shock tube into two compartments. The first compartment contains the driver gas, which can be helium or hydrogen. The second compartment contains the test gas. The test gas is shock heated twice; first by the normal shock that is formed when the diaphragm raptures, and then as the shock reflects from the end of the tube. The stagnant gas behind the reflected shock breaks the secondary diaphragm, escapes through the nozzle throat and expands in the nozzle to hypersonic conditions. Measurements are made throughout the experiment, both inside the shock tube and at the exit-plane of the nozzle. Based on these measurements, the free-stream conditions are computed by expanding the measured reservoir (stagnation) conditions assuming quasi one-dimensional flow.

These experiments were designed to result in low free-stream Reynolds numbers, in order to exhibit fully laminar flow over the double-cone model. Additionally, the free-stream enthalpy is low enough such that there is no dissociation. We present simulations for two experimental conditions of several available – Run 28 and Run 35. These two sets of conditions are of nitrogen flows at similar Reynolds numbers, but they differ in the free-stream Mach numbers. The free-stream and

wall conditions for these cases are tabulated in Table (4.1).

Case	Run 28	Run 35
M_∞	9.59	11.30
Re_m ($10^3/m$)	130.9	133.3
T_∞ (K)	185.56	138.89
T_{wall} (K)	293.33	296.11
ρ_∞ ($10^{-3}\text{ kg}/\text{m}^3$)	0.6545	0.5515
u_∞ (m/s)	2663.9	2712.7

Table. 4.1 Free-stream and wall conditions for the 25° - 55° sharp double-cone LENS experiments.

The available data for making comparisons between numerical results and the experiments are surface quantities and Schlieren images. The surface quantities are surface pressure and heat transfer rate, measured at several locations along the model. There are approximately 25 pressure measurements and 40 heat transfer rate measurements for each of the two cases. This large number of measurements makes these experiments the highest resolution data obtained over double-cone flows. It should be noted that such a large number of measurements is desirable because it enables us to get an accurate estimate of the separation zone size.

4.3 Computations of the Experiments

In this section we present results from numerical simulations of the LENS low enthalpy experiments and we make direct comparisons with the experimental data. We emphasize that the results presented in this section are compared against the experimental measurements in a *blind* manner, as there had been no prior knowledge of the experimental results when the simulations were performed. The experimental data were released after completion of the simulations, and after the first comparisons were made by a third party (see Harvey *et al.* (2001)).

We simulated the flow assuming that the free-stream was in equilibrium, and we allowed for vibrational excitation and nonequilibrium nitrogen dissociation based on the Park model. We observed a very small degree of vibrational excitation, which accounted for a small fraction of the energy. There was essentially no dissociation in

the flow. We also performed a grid convergence study and found that we obtained grid-independent results with a mesh of at least 1024×512 points in the streamwise and wall-normal directions. Therefore, we used a 1024×512 point mesh for these simulations. The simulations were performed on a cluster of DEC/Compaq high-performance XP-1000 Alpha workstations connected with a Myrinet interconnect. We obtained perfect scaling on the finest mesh up to the 16 available processors. These simulations required about 24 hours of simulation time.

Fig. (4.1) shows computed Mach number contours under Run 28 conditions. The flow in this figure is circularly symmetric about a horizontal axis passing through the tip of the geometry. The darkest contour shade indicates regions of the domain where the flow is subsonic. The oblique shock originating from the sharp tip is visible. The shock generated by the separated region of the flow interacts with the bow shock, and the triple point is clearly defined. Also shown is the subsonic region behind the strong bow shock, as well as the supersonic jet. A small kink is visible along the bow shock. The peak temperature is observed behind the bow shock near the triple point, where the flow goes through, essentially, a normal shock. The free shear-layer that forms at the edge of the separation is highlighted by the change in the Mach number across the flow direction.

Fig. (4.2) shows an experimental and numerical Schlieren image of the flow over the double cone for Run 28. Because of the large size of the model, the experimental Schlieren image shows only the upper part of the double cone. The numerical Schlieren was constructed by simply visualizing the second gradient of the density field along the axisymmetric domain. The shock structure is visible in the experimental image. Some detail of the shock structure at the point of interaction is also visible. Although the numerical image looks qualitatively similar to the experimental image, it appears that the triple point is shifted downstream in the computed result. Furthermore, the shock shape is slightly different in the vicinity of the triple point.

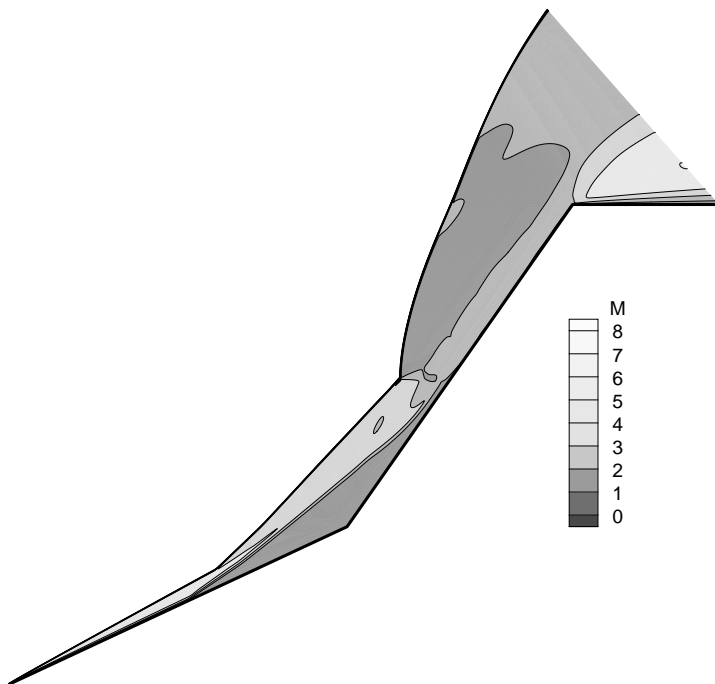


Fig. 4.1 Computed Mach number contours of the flow generated by a 25° - 55° double-cone geometry at Run 28 conditions.

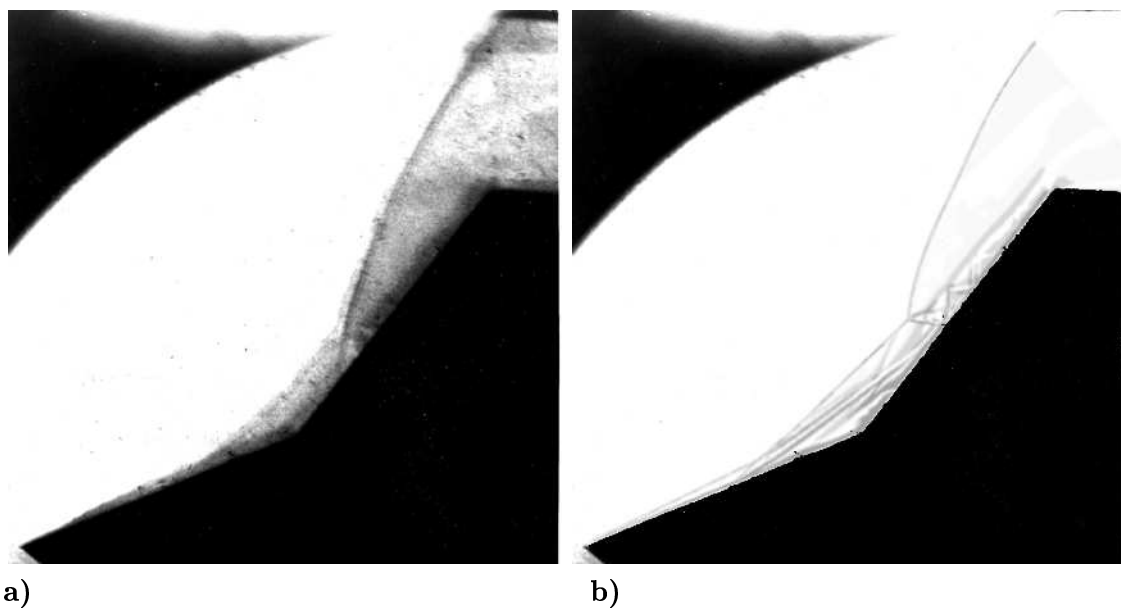


Fig. 4.2 Experimental (a) and numerical (b) Schlieren images for LEN5 Run 28.

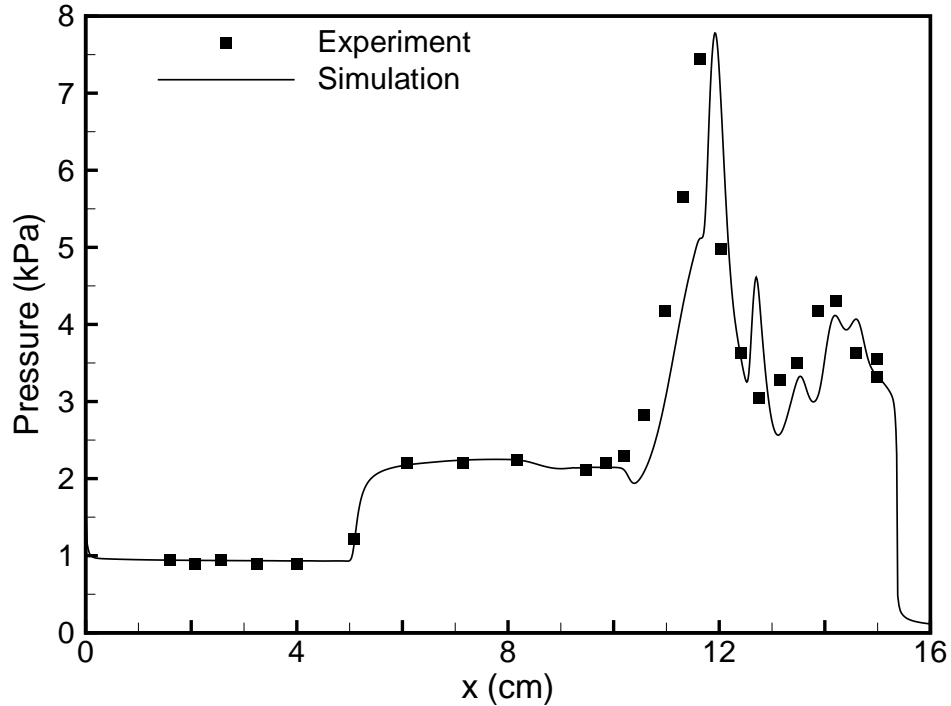


Fig. 4.3 Computed surface pressure and experimental measurements plotted versus axial distance on the 25° - 55° double-cone geometry at Run 28 conditions.

Direct comparisons between the numerical predictions and the measurements are made by plotting surface quantities. Fig. (4.3) shows computed surface pressure and experimental measurements plotted versus the axial distance on the model. We see a region of constant pressure along the first cone where the flow is attached. The sharp increase in surface pressure indicates separation. In this case, the flow separates at about half the length of the first cone. There is a pressure plateau inside the separation zone, which is followed by a very large increase at the point where the transmitted shock impinges on the surface of the second cone. The fluctuations in surface pressure downstream of the point of interaction are due to the compression and expansion of the jet near the surface. The constant pressure region along the first cone is predicted by the simulation to within 5% of the measurements. This is well within the experimental uncertainty. The pressure is also matched inside the

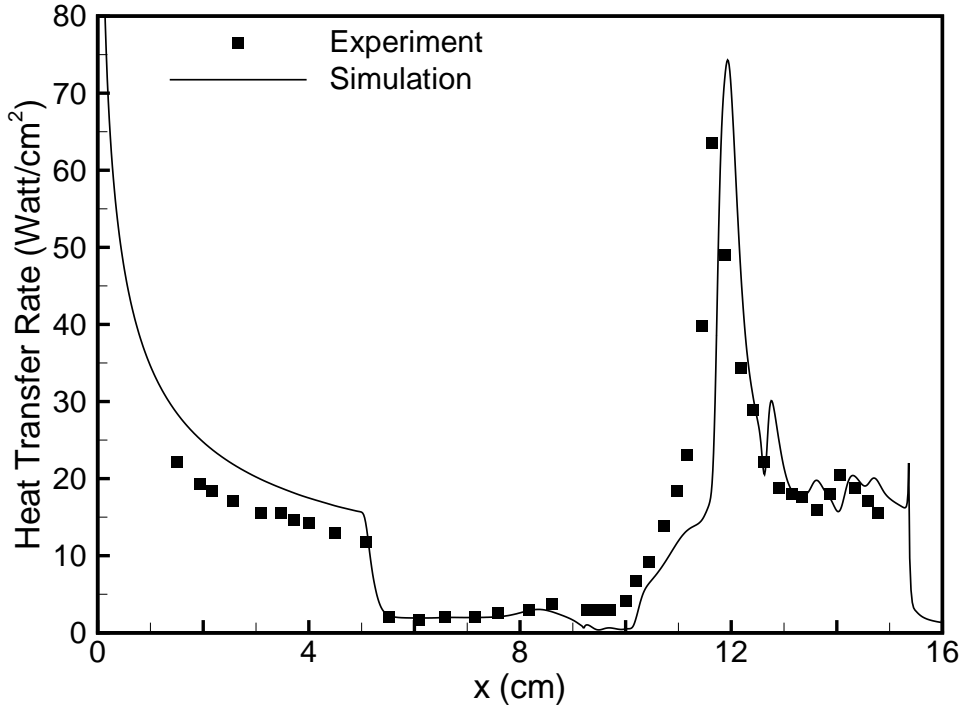


Fig. 4.4 Computed heat transfer rate and experimental measurements plotted versus axial distance on the 25° - 55° double-cone geometry at Run 28 conditions.

separation zone, and the peak pressure at the point of interaction agrees well with the experimental data. The general trend and level of pressure fluctuation after re-attachment are also reproduced, but are not exactly matched. This is because the location of the point of interaction is not predicted exactly. We observe similar results with the heat transfer rate data, which is shown in Fig. (4.4). The simulation reproduces the level of heat transfer rate everywhere, with the exception of the attached region of the flow near the tip. In this region, the heat transfer rate is over-predicted by the simulation by about 20%. Also, it is not clear whether the separation point is predicted exactly, however the computed result is at most within 4 mm of that observed based on the pressure and heat transfer rate data.

The results of the simulations under Run 35 conditions are similar to the results of Run 28. Computed Mach number contours for Run 35 are shown in Fig. (4.5). The basic flow is similar to Run 28, however the separated region

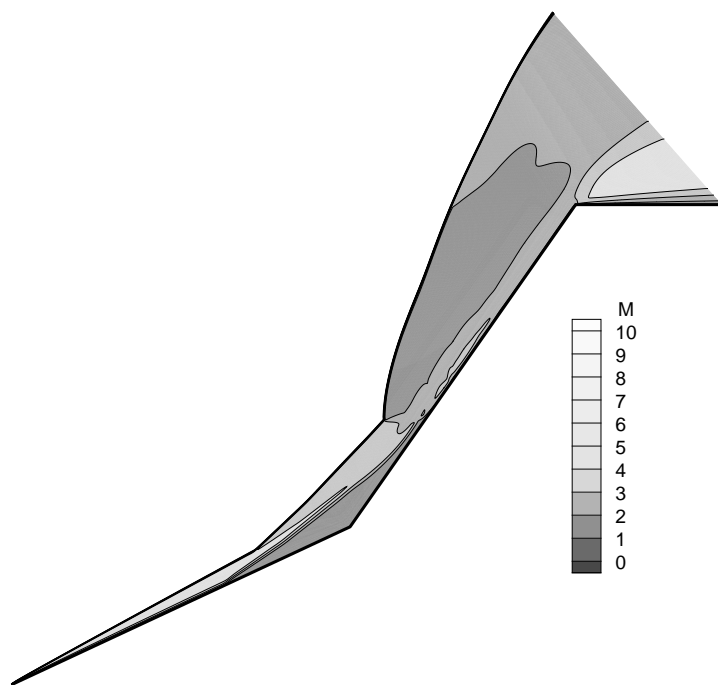


Fig. 4.5 Computed Mach number contours of the flow generated by a 25° - 55° double-cone geometry at Run 35 conditions.

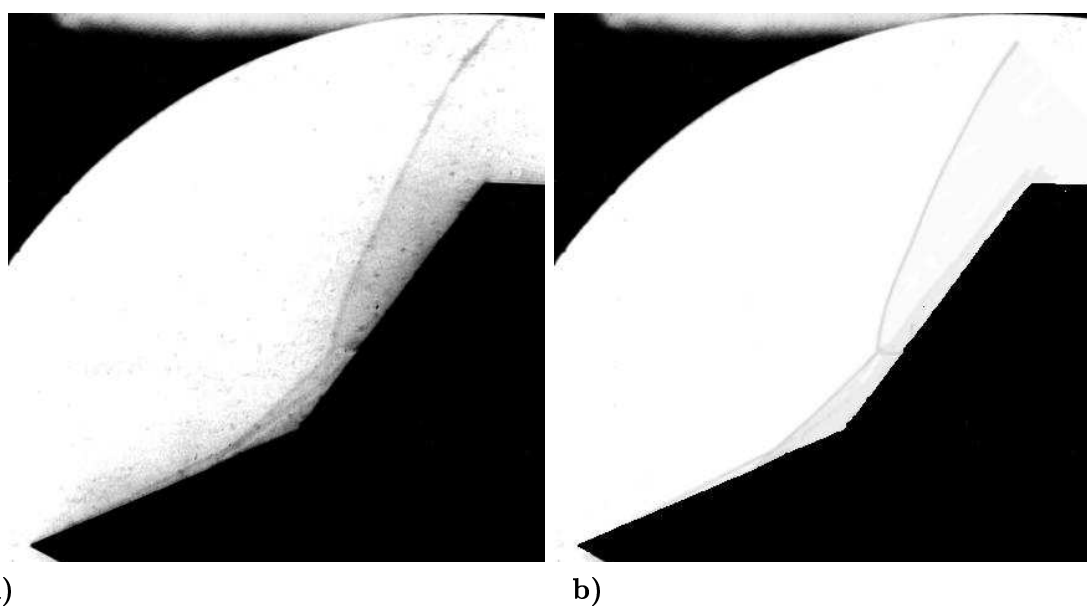


Fig. 4.6 Experimental (a) and numerical (b) Schlieren images for LENS Run 35.

is significantly smaller for this case. The darkest contour level indicates subsonic flow, and this is seen behind the strong bow shock and in the separation zone. The shape of the supersonic jet and the kink in the bow shock are also visible. Fig. (4.6) shows the corresponding experimental and numerical Schlieren images of the flow over the double cone for Run 35. The shock shapes in these images look remarkably similar. The location of the kink in the bow shock is predicted very well. Also, the shock structure near the triple point and the transmitted shock look the same, to the level of detail and the extent of comparison that can be made using this image.

Fig. (4.7) plots computed surface pressure for Run 35 together with experimental measurements versus axial distance. The pressure in the attached region along the first cone is slightly under-predicted by the simulation, but is within the 5% quoted experimental uncertainty. However, the level of pressure inside the separation zone is not reproduced. The difference in this region is approximately 10% of the measured values. It is not clear whether the peak pressure is over-predicted, or the large discrepancy observed is because of not having predicted correctly the location of the interaction point. The pressure distribution is predicted reasonably well along the second cone after reattachment. Also, the separation zone size is over-predicted by about 2 mm.

The heat transfer rate for Run 35 is plotted in Fig. (4.8). We observe good agreement with the measurements made inside the separation zone and after reattachment, but the heat transfer rate is substantially over-predicted along the first cone. This difference is about 20%, and this is consistent with Run 28. Also, the location of the peak in heat transfer rate is not predicted exactly.

4.4 Remarks on Blind Comparisons

The simulations of Run 28 and Run 35 from the low enthalpy LENS experiments presented in the previous section showed good overall agreement with the experimental measurements. The numerical predictions were obtained using a

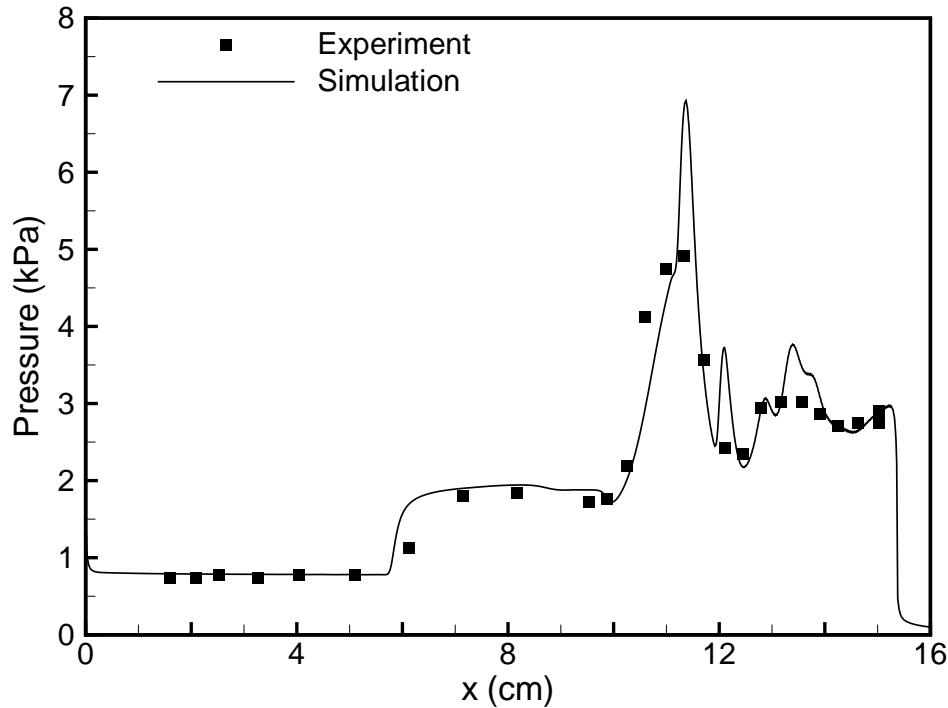


Fig. 4.7 Computed surface pressure and experimental measurements plotted versus axial length of the 25°-55° double-cone geometry at Run 35 conditions.

nonequilibrium formulation, which allowed for vibrational energy excitation and nitrogen dissociation. However, because there was essentially no dissociation and there was little vibrational energy excitation, the present results can be reproduced using a perfect-gas simulation.

The simulations required a relatively large number of grid points in order to achieve grid-convergence. A carefully constructed grid of at least 1024×512 points produced grid-independent results. This is consistent with earlier work on flows over double-cones by Wright *et al.* (1999). The study by Gaitonde *et al.* (2002) shows similar grid convergence. They also conducted a careful time convergence study, and showed that the solution does not converge until at least 100 characteristic flow times have been established. The simulations presented here are consistent with their findings, and we simulate our flows to a minimum of 150

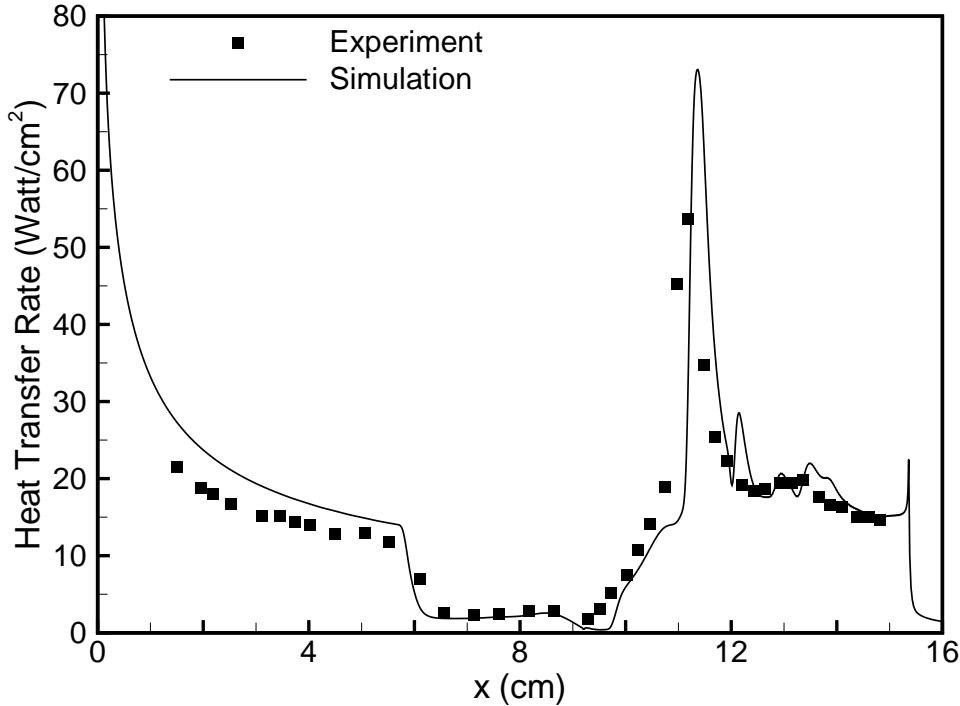


Fig. 4.8 Computed heat transfer rate and experimental measurements plotted versus axial length of the 25° - 55° double-cone geometry at Run 35 conditions.

flow times. It should be noted that such simulations on a grid of the size required for grid-convergence are very expensive.

The simulations assume that the flow is laminar, which is consistent with the experiments. If the flow were transitional or turbulent, the simulations would under-predict the heat transfer rate measurements. Also, we expect the flow to be laminar because the Reynolds number based on the free-stream conditions and model diameter is at most 40,900 for the cases considered. Additionally, the free shear-layer that forms at the edge of the separation zone – and is the most unstable region in the flow – remains steady. The shear-layer Reynolds number computed based on the Birch and Keyes (1972) definition for free shear-layers formed by shock interactions, is under 20,000, and is expected to be stable.

The blind comparisons made in this work illustrate that numerical methods

are capable of reproducing double-cone flows, and this is done within a reasonable amount of time. However, it is necessary to use an efficient implicit solver. The surface pressure predictions in regions where the pressure is constant are at most within 10% of the measurements, and the heat transfer rate predictions exhibit a similar trend. However, the heat transfer rate along the first cone is overpredicted in both cases by about 20%. These results are consistent with the findings of other researchers who have simulated these flows [Gaitonde *et al.* (2002), Gnoffo (2001), & Roy *et al.* (2001)]. In the following chapters we perform more detailed simulations of the entire experiment, to determine the source of the discrepancies.

Chapter 5

Effects of Numerics on Double-Cone Flows

5.1 Introduction

In this chapter, we address the numerical aspects of the simulation of double-cone flows. The main issue that is addressed concerns the effect of the numerics on the interaction between the shocks and the separation zone. We show that the shock interaction and the separation zone are very sensitive to the numerical dissipation. The numerical dissipation depends on the accuracy of the numerical scheme used in the discretization of the equations, and on the refinement of the mesh. For the purposes of this analysis we examine only one case, Run 35, from the LENS experiments presented in the previous chapter. This work was done in collaboration with Dr. Marie-Claude Druguet of IUSTI - École Polytechnique Universitaire de Marseille.

As discussed in chapter 1, the influence of the shock angles on the recirculation zone is very important. In the context of numerical simulation, this translates to being able to predict correctly the shock locations and the location of the triple point. Thus, it is critical to resolve the initial boundary layer growth near the model leading edge, and also to resolve the finer flow structure at the point of interaction. Therefore, several levels of grid refinement are used until grid convergence is achieved. We show that grids of 1/2 million points give accurate results.

To investigate the effect of the numerical dissipation of the schemes, several flux evaluation methods are used. We compare the results obtained with different schemes by displaying physical characteristics of the flow and by monitoring the evolution of the surface quantities. We show that the computed results are very

sensitive to the numerical flux evaluation method used. We find that when the grid is fine enough, all the flux evaluation schemes give the same results. However, this may require a very large number of points for the most dissipative schemes. The less dissipative schemes give the final, grid converged, result on a coarser mesh, and therefore are less costly. We also show that since a large number of grid points is needed, it is necessary to employ an implicit solver for these computations.

5.2 Grid Size Requirements

We performed a grid convergence study on the double-cone flow under Run 35 conditions. At each level of grid refinement, the number of points in each directions was doubled. For these simulations, we used the second order accurate modified Steger-Warming flux evaluation method presented in chapter 3. We performed perfect gas simulations of the flow at several levels of grid refinement. The finest mesh used contained 2048×1024 points in the streamwise and wall-normal directions. The results are plotted in Fig. (5.1), which plots heat transfer rate on the double-cone model. We see that the heat transfer rates computed on the 1024×512 and 2048×1024 grids are virtually identical. Thus, the results obtained on the 1024×512 grid are converged.

5.3 Importance of Time Integration Method

Careful time convergence studies by Gaitonde *et al.* (2002) showed that for this particular test case the solution does not converge until at least 100 characteristic flow times have been computed. The characteristic flow time has been defined as the time it takes for a particle to travel the length of the geometry, if it is moving at the free-stream velocity, $\tau_{\text{char}} = L/u_\infty$. The relatively long time scale of $100 \times \tau_{\text{char}}$ allows the separation zone to become fully established. In this work, we simulate the flow for at least 150 flow times before considering that the solution has reached a steady state.

We achieve grid converged results on a grid of 1024×512 points, and the characteristic size of the smallest cell on this mesh, Δy_{\min} is of the order of $0.1 \mu\text{m}$.

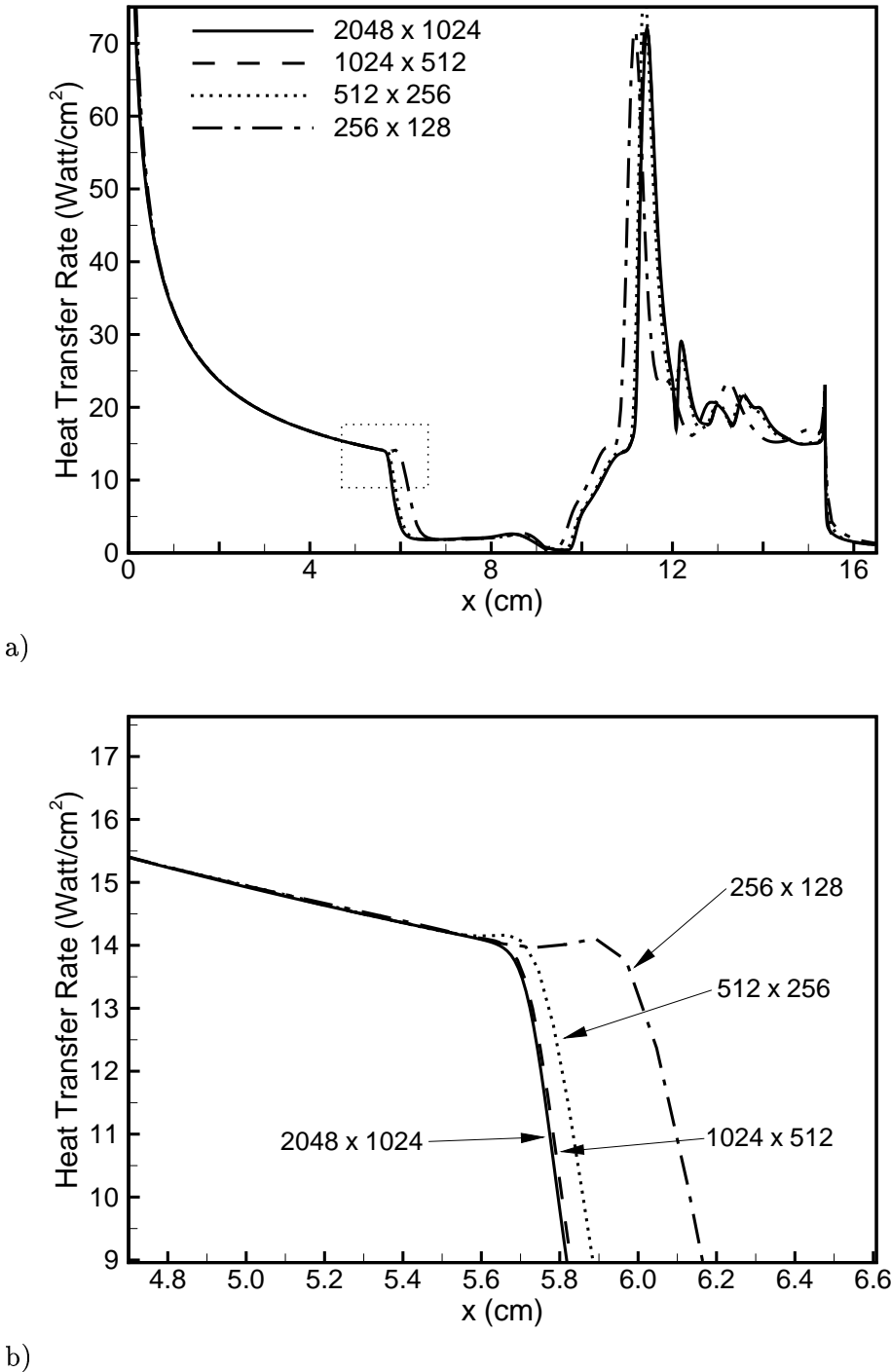


Fig. 5.1 Heat transfer rate for a perfect gas simulation computed on four different grids; (b) shows an enlargement near the point of separation.

In order to maintain stability of the numerical scheme, the computational time allowed on such a mesh is $\tau_{\text{expl}} \approx \text{CFL}_{\text{expl}} \times \Delta y_{\min} / u_{\infty}$, where $\text{CFL}_{\text{expl}} < 0.4$ for second-order schemes. Then, to reach the steady state solution with an explicit method of time integration, $N_{\text{expl}} = 150\tau_{\text{char}}/\tau_{\text{expl}}$ iterations must be performed. The double-cone geometry is approximately 0.18 m in length, and therefore, N_{expl} is of the order 10^8 . Performing such a large number of iterations would require an enormous amount of physical time, thus making the simulation of the double-cone flows impossible. Therefore, it is necessary to employ an implicit method of time integration, which allows for a time step much larger than τ_{expl} to be taken.

5.4 Flux Evaluation Methods

Several flux evaluation methods are employed in this work, with the purpose to examine the effect of numerical dissipation on the solution of double-cone flows. In addition to the modified Steger-Warming method discussed in chapter 3, the Roe method with the H entropy correction [Sanders *et al.* (1998)], the Lax-Friedrichs (LF) method, the Harten-Lax-van Leer (HLL) and Harten-Lax-van Leer Contact (HLLC) methods are employed. These methods are well documented in the literature [Toro (1997)]. Also, higher order of spatial accuracy of the flux evaluation is achieved using the MUSCL variable extrapolation method, where the conserved variables are extrapolated to the cell faces using a second order reconstruction scheme. Non-linear limiters are commonly used to prevent oscillations, and the minmod, van Albada, van Leer, and superbee limiters are employed in this work. For a discussion on slope limiters see Hirsch (1991). More details regarding limiters can be found in Laney (1998).

The fluxes computed using the different flux evaluation methods must be accurately linearized in time in order to be used in conjunction with an implicit solver. The linearization procedure depends on the flux evaluation method, and in some cases increases the computational cost associated with the original method. The linearization procedure presented in chapter 3 can be applied directly to split flux

methods, but the same approach can be taken to obtain flux Jacobians for other methods [Druguet *et al.* (2003)]. Furthermore, the implicit equation remains unchanged for the inviscid problem.

5.5 Time Convergence

We are interested in obtaining the steady state solution with each of the different numerical methods, thus we may start the simulation with any physically acceptable initial condition. We typically start the simulation by initializing the flow to the free-stream conditions everywhere. However, we may also start from any solution already obtained using any of the flux evaluation methods, and iterate until the solution reaches steady state. This may result in considerable savings in computational time.

Because we use an implicit solver, we take the largest possible time step in order to obtain results in the smallest computational time. However, if the time step is too large, the computation does not converge as fast to the steady result as with a smaller time step. If the time step is even larger, the simulation may enter a limit cycle, where the solution keeps oscillating among states, and the residual never decreases. This is commonly referred to as *ringing* of the solution. This may be particularly important for flows with shock interactions and recirculation regions. Therefore, the convergence rate depends highly on the time step size. Also, simulations with different numerical flux evaluation methods converge differently. For example, the HLL and HLLC methods require more iterations than the Roe scheme to converge. Additionally, simulations performed with the Roe scheme and the minmod limiter converge much faster than simulations performed with the same scheme and less dissipative limiters, such as the van Albada and superbee.

5.6 Results on Coarse Grids

In this section we present results of simulations performed on the coarsest mesh (256×128) used in this work. We show the shock location by plotting the $T = 400$ K temperature contour in Fig. (5.2). The numerical results were computed with different second order flux evaluation methods (mod SW,

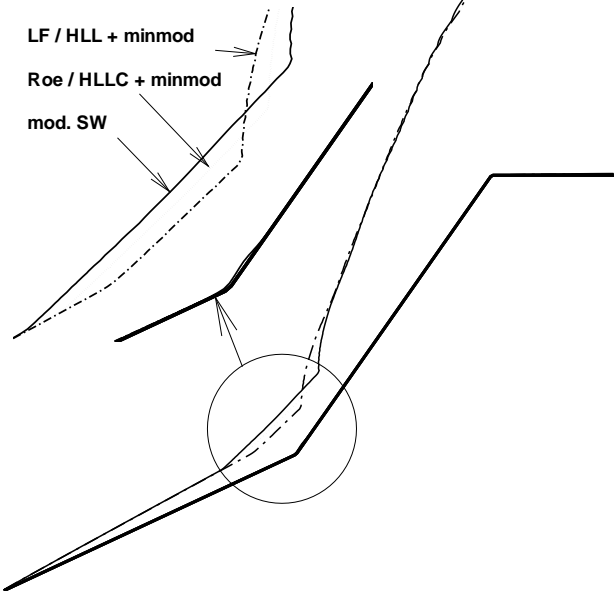


Fig. 5.2 Shock location ($T = 400$ K contour) computed with different flux evaluation methods on a 256×128 grid.

LF, Roe, HLL, and HLLC). These computed results, with the exception of the one computed with the modified Steger-Warming method, use a solution reconstruction scheme where the slopes are limited with the minmod limiter. This limiter is known to be dissipative. From this figure, we see that the size of the separation zone depends on the method used. The more dissipative schemes (LF and HLL) produce a much smaller separation zone than the less dissipative schemes (mod SW and Roe). The solution computed with the modified Steger-Warming method gives the largest separation zone because the scheme used for variable extrapolation is much less dissipative than the minmod limiter. When the Roe scheme is used with a slope limiter less dissipative than minmod, it results in a larger separation zone. This is shown in Fig. (5.3), which plots the shock location computed with different slope limiters for the variable extrapolation. Interestingly, when we rank the results from the smallest to the largest size of separation, the list corresponds to the classification of the slope limiters according to decreasing dissipation [Toro (1997)]. These results show that the less dissipative the numerical scheme,

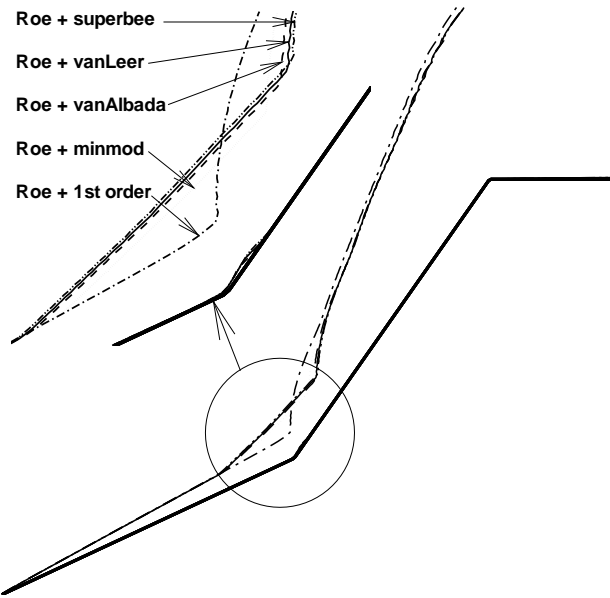


Fig. 5.3 Shock location ($T = 400$ K contour) computed with the Roe scheme and different slope limiters on a 256×128 grid.

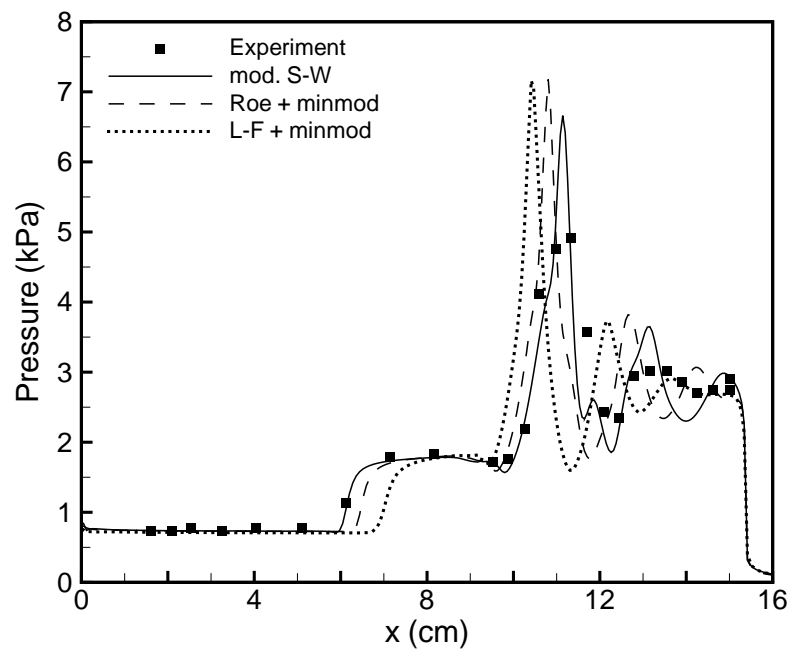


Fig. 5.4 Surface pressure predictions on the double-cone computed with different flux evaluation methods on a 256×128 grid.

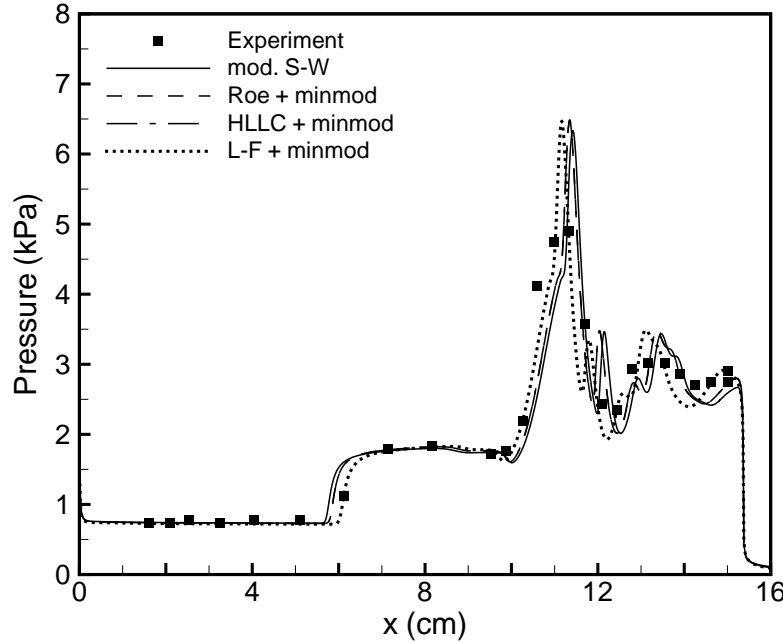


Fig. 5.5 Surface pressure on the double-cone computed with different flux evaluation methods on a 1024×512 grid.

the larger the separation zone. Furthermore, these results are reflected in the plots of the surface quantities; the pressure is shown in Fig. (5.4).

5.7 Results on Fine Grids

In this section, we show results obtained on a fine mesh. Fig. (5.5) shows the surface pressure computed on a 1024×512 grid using four different schemes (mod. SW, Roe with minmod, HLLC with minmod, and LF with minmod). These results are much closer to one another than the results obtained on the coarse grid, shown in Fig. (5.4). The results obtained using the Roe and HLLC schemes with the minmod slope limiter are identical on this mesh. The most dissipative scheme (LF+ minmod) still does not give the same results as the other methods, because it has not yet reached grid convergence. The size of the separation zone obtained with the less dissipative Roe scheme is still smaller than what is obtained with the modified Steger-Warming method. This is because the minmod limiter is too dissipative.

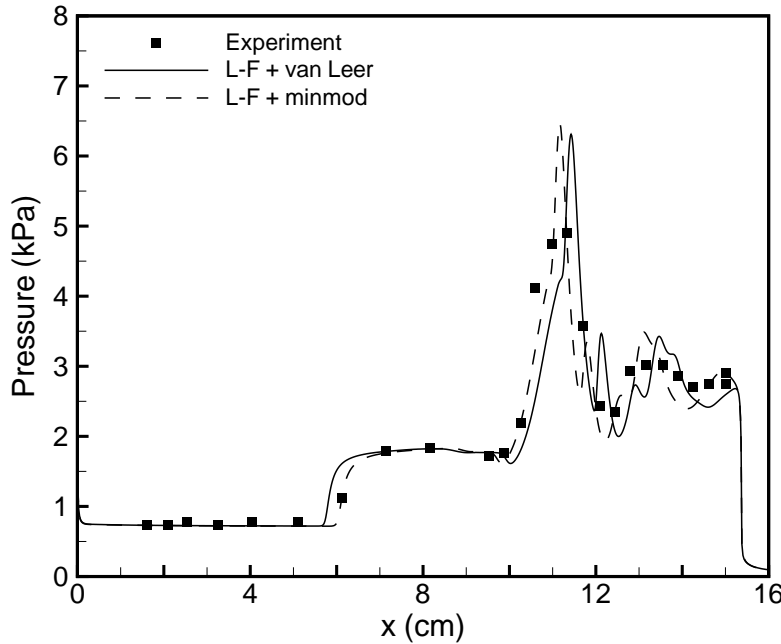


Fig. 5.6 Surface pressure on the double-cone model computed with the Lax-Friedrichs scheme and different slope limiters on a 1024×512 grid.

There is noticeable improvement in the results when a less dissipative slope limiter is used for variable extrapolation, especially when the solver itself is very dissipative. This is shown in Fig. (5.6), which plots the surface pressure computed using the Lax-Friedrichs scheme, and two different limiters (minmod and van Leer). Also, if we compare the Roe and Lax-Friedrichs solutions computed with the van Leer limiter in both cases, we see that the results are very similar.

5.8 Evolution of the Separation Zone Size

It is very useful to know how different numerical schemes perform by looking at a single scalar quantity, as opposed to distributions of surface quantities. In earlier sections we showed how the size of the recirculation zone depends greatly on the amount of numerical dissipation of the numerical scheme. Thus, we can get a measure of the dissipation by comparing the size of the separation zone that is predicted when a particular scheme is employed. Additionally, we can obtain information about grid convergence by plotting the size of the separation zone

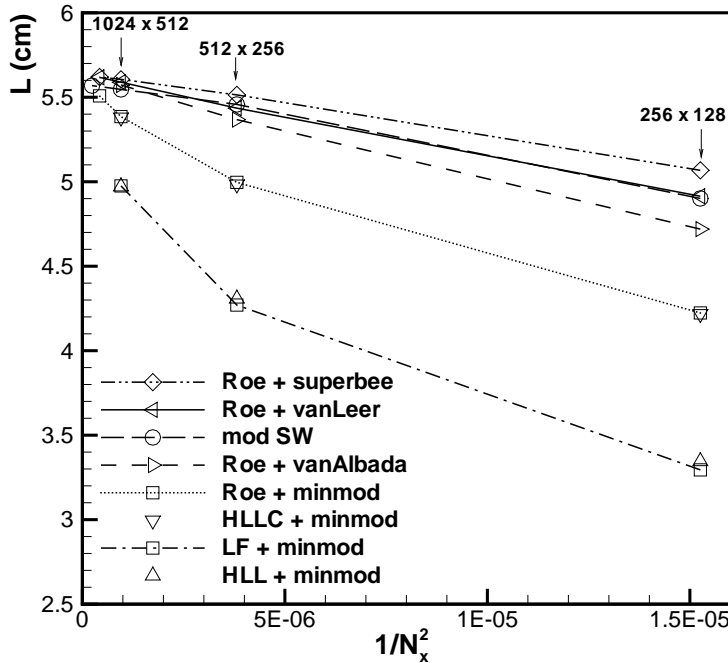


Fig. 5.7 Size of the recirculation zone versus the square of the inverse of the number of points in the streamwise direction.

versus the size of the mesh. First, we need to define how we measure physically the size of the recirculation region. We define the size of the recirculation L , as the length between the point of detachment on the first cone, and the point of reattachment on the second cone. It is easy to obtain this information from numerical solutions by plotting the surface skin friction coefficient C_f . The detachment point is where the skin friction coefficient becomes negative, and the re-attachment point is where the C_f becomes positive again. Note that in certain cases there can be multiple, small-scale, bubbles of separated flow inside the large recirculation zone.

Fig. (5.7) plots the size of the recirculation zone obtained with different schemes, versus the square of the inverse of the number of points in the streamwise direction N_x . This figure allows us to show the evolution of the size of the recirculation zone as the grid is refined, when different numerical schemes are employed. The results obtained on the coarsest grid are further to the right. As the grid is refined,

$1/N_x$ decreases, and the results converge toward the same value. When the grid is refined to 2048×1024 points, the result obtained with the modified Steger-Warming method remains the same as on the 1024×512 grid. This shows that our results are grid converged.

5.9 Conclusions

This study shows that numerical predictions of hypersonic flow over the double-cone model are very sensitive to the numerical flux evaluation method. All schemes give the same results when grid convergence is reached, however on coarse meshes different flux evaluation schemes give different results. The least dissipative flux evaluation methods examined in this work (modified Steger-Warming, Roe with van Leer limiter, and HLL-Contact with van Leer limiter) give grid converged results on a 1024×512 grid. The more dissipative schemes (Lax-Friedrichs, Harten-Lax-van Leer) and schemes that employ the minmod limiter for variable extrapolation do not converge at this level of grid refinement.

It is important to note that the grid-converged results obtained on the 1024×512 mesh using the least dissipative method do not match the experimental data. Most importantly, the size of the separation zone appears to be over-predicted by the most numerically accurate solution. This is not due to numerical error, and it is because of inadequate modeling of the flow physics, as we will see in chapter 6.

Because the double-cone flow takes a long time to reach its steady state, large amounts of physical time must be simulated. Therefore, an implicit time integration method is required for simulating these flows within a reasonable time frame.

Finally, the dissipation properties of a numerical scheme can be assessed and compared with other methods by using the double-cone flow. In particular, by measuring the size of the recirculation zone from a given numerical solution, a direct assessment can be made of the quality of the numerics employed in the simulation. Furthermore, this can be done without having to perform a complete grid convergence study.

Chapter 6

Characterization of Experiments

6.1 Introduction

In chapter 4 we presented results of simulations over two double-cone flows, and we made comparisons with the experimental data. We observed good overall agreement between numerical predictions and experimental measurements, with the exception of the heat transfer rate on the first cone near the tip. This discrepancy was common to both cases presented, and these results are consistent with simulations performed by other researchers. Therefore, the purpose of this chapter is to present a study of the source of this discrepancy. We do this by examining the way the experiments are performed, and in particular how the free-stream conditions are obtained. We also examine possible non-continuum effects on solid boundaries.

We assess the accuracy of the nominal test-section conditions by using CFD to compute the flow in the LENS facility nozzle, including the effects of vibrational nonequilibrium. We also investigate the accuracy of the conventional no-slip boundary condition at solid walls for these relatively low-density flows. Finally, we use our computed test-section conditions to study the effect of slight free-stream non-uniformity on the computed separation zone size. When all these effects are included in the simulation of the double-cone flow of interest, improved agreement between computations and experiments is obtained.

6.2 Vibrational Nonequilibrium

The specification of the free-stream conditions is an important aspect of hypersonic flow experiments. In a reflected shock hypersonic wind tunnel such as LENS Leg I, high temperature and pressure gas is expanded from the reservoir conditions

through a contoured nozzle to high Mach number. It is well known that the vibrational modes of the gas may freeze near the nozzle throat conditions. Vibrational freezing is particularly important in nitrogen at relatively low pressure reservoir conditions, as is the case in the present experiments.

In this section, we discuss how vibrational freezing affects the inferred test conditions in the LENS facility for this particular class of experiments. In the experiments, calibration runs are performed before the tests to verify the uniformity of the flow section. Subsequently, the actual experiments are performed at the same nominal conditions as the calibration runs. In an impulse facility such as LENS, the pressure and enthalpy in the reservoir region behind the reflected shock are known. The Pitot pressure in the test-section can be measured easily, as well as the heat transfer rate to a reference probe. Additional Pitot pressure measurements are made during the experiment to verify that the test conditions are consistent with the calibration run.

To determine the free-stream conditions, a quasi-one-dimensional code is run using the measured reservoir stagnation conditions. Although the exact geometrical specification of the nozzle is known, the effective area ratio is not known due to the wall boundary layer displacement. Therefore, the code is run to the point where the computed Pitot pressure matches the pressure measured by the Pitot probe at the exit-plane of the nozzle. Then, the test conditions are taken to be those given by the quasi-one-dimensional code. This analysis assumes vibrational equilibrium during the expansion, and has been successfully used for a long time, but usually in air at pressures higher than considered in the present experiments.

To illustrate how the free-stream conditions are inferred, consider the Rayleigh Pitot pressure formula

$$\frac{p_{\infty 2}}{p_{\infty}} = \frac{\gamma + 1}{2} M_{\infty}^2 \left(\frac{\frac{\gamma+1}{2} M_{\infty}^2}{\frac{2\gamma}{\gamma+1} M_{\infty}^2 - \frac{\gamma-1}{\gamma+1}} \right)^{1/(\gamma-1)}$$

which in the hypersonic limit reduces to

$$\begin{aligned} p_{o2} &= \frac{\gamma+1}{2} \left(\frac{(\gamma+1)^2}{4\gamma} \right)^{1/(\gamma-1)} p_\infty M_\infty^2 \\ &= \frac{\gamma+1}{2\gamma} \left(\frac{(\gamma+1)^2}{4\gamma} \right)^{1/(\gamma-1)} \rho_\infty u_\infty^2 \end{aligned}$$

where p_{o2} is the measured Pitot pressure and ∞ denotes the free-stream conditions. Thus, the Pitot pressure is effectively a measurement of the kinetic energy per unit volume in the free-stream.

Now consider an ideal, adiabatic expansion from the reservoir to hypersonic conditions. The total enthalpy of the reservoir is converted to free-stream kinetic energy conserved according to

$$h_o = C_p T_\infty + \frac{1}{2} u_\infty^2 \simeq \frac{1}{2} u_\infty^2$$

where we have assumed that $\frac{1}{2} u_\infty^2 \gg C_p T_\infty$. Therefore, given the reservoir enthalpy, we have the value of u_∞^2 in the inviscid portion of the nozzle flow. Then, with a measurement of the Pitot pressure, we effectively measure the free-stream density for the ideal expansion.

Now consider what happens if there is vibrational energy frozen in the flow during the expansion. We have

$$\frac{1}{2} u_\infty^2 \simeq h_o - e_v^*$$

where e_v^* is the vibrational energy per unit mass frozen in the flow. Thus, the kinetic energy will be lower than in an ideal expansion, and to obtain the same measured Pitot pressure, the free-stream density must be larger. Thus, the effect of vibrational freezing in the nozzle is to lower the axial velocity and increase the density relative to an equilibrium analysis. To first-order, the surface pressure scales with $\rho_\infty u_\infty^2$ and the heat transfer rate with $\rho_\infty u_\infty^3$. Thus, we do not expect vibrational freezing to affect the measured surface pressure, but it should reduce the measured heat transfer rate due to the lower value of u_∞ .

In this analysis we have assumed that the Rayleigh Pitot pressure formula is valid under conditions of vibrational nonequilibrium. We have simulated the flow over the Pitot probe used in the experiments using a finite-rate relaxation model for nitrogen. These calculations show that under the conditions of interest, the Rayleigh Pitot pressure formula gives the correct value of Pitot pressure, and the above analysis is valid.

6.3 Nozzle Flow Simulations

The preceding elementary analysis shows that vibrational freezing reduces the measured heat transfer rate. However, a more complete analysis is required to determine how much vibrational freezing occurs and to assess the additional non-ideal effects in the nozzle flow. Thus, we have performed a series of CFD simulations of the nozzle flows. In these simulations, we have used the numerical method presented in chapter 3 with the Baldwin-Lomax (1978) and the Spalart-Allmaras (1992) turbulence models for the nozzle wall boundary layer.

The nozzle grids are constructed directly from the CAD files of the nozzle contours. Typical grids use 1788 points in the axial direction and 128 points in the surface normal direction, with stretching at the surface. The nozzle throats are elongated, making the specification of the sonic line difficult. Thus, the flow is computed from the constant diameter driven tube section, through the throat, and to the test-section. Thermo-chemical equilibrium was assumed at the inflow, and subsonic inflow conditions were implemented so that total enthalpy is conserved in the computed flow.

Initial simulations of the nozzle flow showed a significant over-prediction of the centerline Pitot pressure. This is caused by the Baldwin-Lomax turbulence model over-predicting the boundary layer displacement thickness at the nozzle exit-plane. This results in higher velocity in the inviscid region, and also high Pitot pressure. The strong favorable pressure gradient in the nozzle reduces the effect of turbulent transport through the boundary layer, reducing the rate of boundary layer growth.

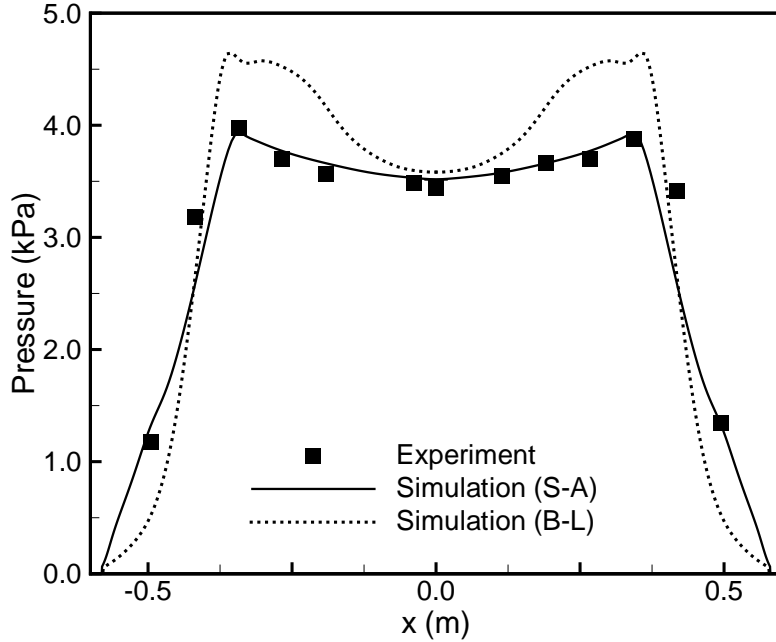


Fig. 6.1 Pitot pressure in the nozzle exit-plane compared with nozzle computation for Run 1302 (calibration for Run 35).

This mechanism is not included in any algebraic turbulence models. Thus, we recognized that the results obtained using the algebraic turbulence model were not realistic. Therefore, we implemented the one-equation turbulence model of Spalart and Allmaras, with the compressibility correction suggested by Catris and Aupoix (2000), to perform additional simulations. This model allows for suppression and amplification of turbulence based on the local flow characteristics. Implementation of this model requires the solution of an additional conservation equation. We simulated the flow in the nozzle using this model and found that the simulation matched the measured Pitot pressure profile. This is shown in Fig. (6.1), which plots the measured Pitot pressure for the calibration run for Run 35 ($p_o = 3.55 \text{ MPa}$, $h_o = 3.71 \text{ MJ/kg}$) with the results of two nozzle simulations.

We ran a nozzle simulation with the actual Run 35 reservoir conditions ($p_o = 3.77 \text{ MPa}$, $h_o = 3.83 \text{ MJ/kg}$). From the simulation, we obtain the free-stream

conditions at the test-section. The results of this simulation are tabulated in Table (6.1) along with those provided by Holden (2000) using the equilibrium quasi-one-dimensional analysis. Note that the vibrational temperature is predicted to freeze at 2562 K, which is close to the throat temperature. The resulting dynamic pressure and kinetic energy flux are also given. The computed value of the dynamic pressure is lower than that derived from the nominal conditions because we have matched the Pitot pressure profile, rather than a single mean value of Pitot pressure. Also note that $\rho_\infty u_\infty^3$ is 12.4% lower in the nonequilibrium simulations due to the 6.7% lower value of Pitot pressure and the 6.2% lower value of axial velocity. A similar analysis was carried out for Run 28, and the results are given in Table (6.2). In this case, the predicted Pitot pressure is 2.5% higher and the resulting kinetic energy flux is reduced by only 2.6%.

Case	Nominal	Nonequilibrium
T_∞ (K)	138.9	98.27
$T_{v\infty}$ (K)	138.9	2562
ρ_∞ (g/m ³)	0.5515	0.5848
u_∞ (m/s)	2713	2545
M_∞	11.30	12.59
$\rho_\infty u_\infty^2$ (Pa)	4059	3788
$\rho_\infty u_\infty^3$ (W/cm ²)	1101	964

Table. 6.1 Nominal and computed test-section conditions for Run 35 reservoir conditions.

Case	Nominal	Nonequilibrium
T_∞ (K)	185.6	140.0
$T_{v\infty}$ (K)	185.6	2589
ρ_∞ (g/m ³)	0.6545	0.7372
u_∞ (m/s)	2664	2538
M_∞	9.50	10.5
$\rho_\infty u_\infty^2$ (Pa)	4645	4749
$\rho_\infty u_\infty^3$ (W/cm ²)	1237	1205

Table. 6.2 Nominal and computed test-section conditions for Run 28 reservoir conditions.

6.4 Results

In the previous sections, we quantified the effect of nonequilibrium in the nozzle and obtained nonequilibrium free-stream conditions by performing simulations of the nozzle flow. In this section, we use the nonequilibrium conditions as free-stream specification to recompute the flows over double-cone models and make comparisons with the measured surface quantities. We show that under nonequilibrium free-stream conditions the heat transfer rate to the first cone is reduced. However, this reduction does not result in complete agreement with the experimental measurements. We also consider non-continuum effects, and in particular the effect of partial accommodation of incident particles at solid boundaries. We examine the effect of velocity slip and temperature “jump” at the surface of the model, as well as possible jump of vibrational energy. We employ the standard Maxwell model for velocity slip and temperature jump, with a simple extension to include jump of vibrational energy as described in chapter 2. In this model, σ , σ_T are the accommodation coefficients for velocity and temperature respectively, and are taken to be 0.85. The value of the vibrational energy accommodation coefficient is not well known, and a value of 0.5 was used initially. This value of σ_v results in nearly complete vibrational accommodation. However, Meolans *et al.* (2002) suggest adiabatic conditions ($\sigma_v = 0$), and Black *et al.* (1974) measure values of the order 10^{-3} for stainless steel. We show that when the slip model is included in the simulations under nominal free-stream conditions the results are very similar to the no-slip results. Under nonequilibrium conditions and with $\sigma_v = 1.0 \times 10^{-3}$ we see a substantial decrease in heat transfer rate to the first cone. Finally, we investigate how small levels of test-section flow non-uniformity in the free-stream affect the flow. We focus on Run 35, and present more limited results for Run 28.

The effect of slip at Run 35 nominal conditions is shown in Fig. (6.2). In this computation, the accommodation coefficients for velocity and temperature were 0.85, while a value of 0.5 was used for vibrational energy. We see that slip has

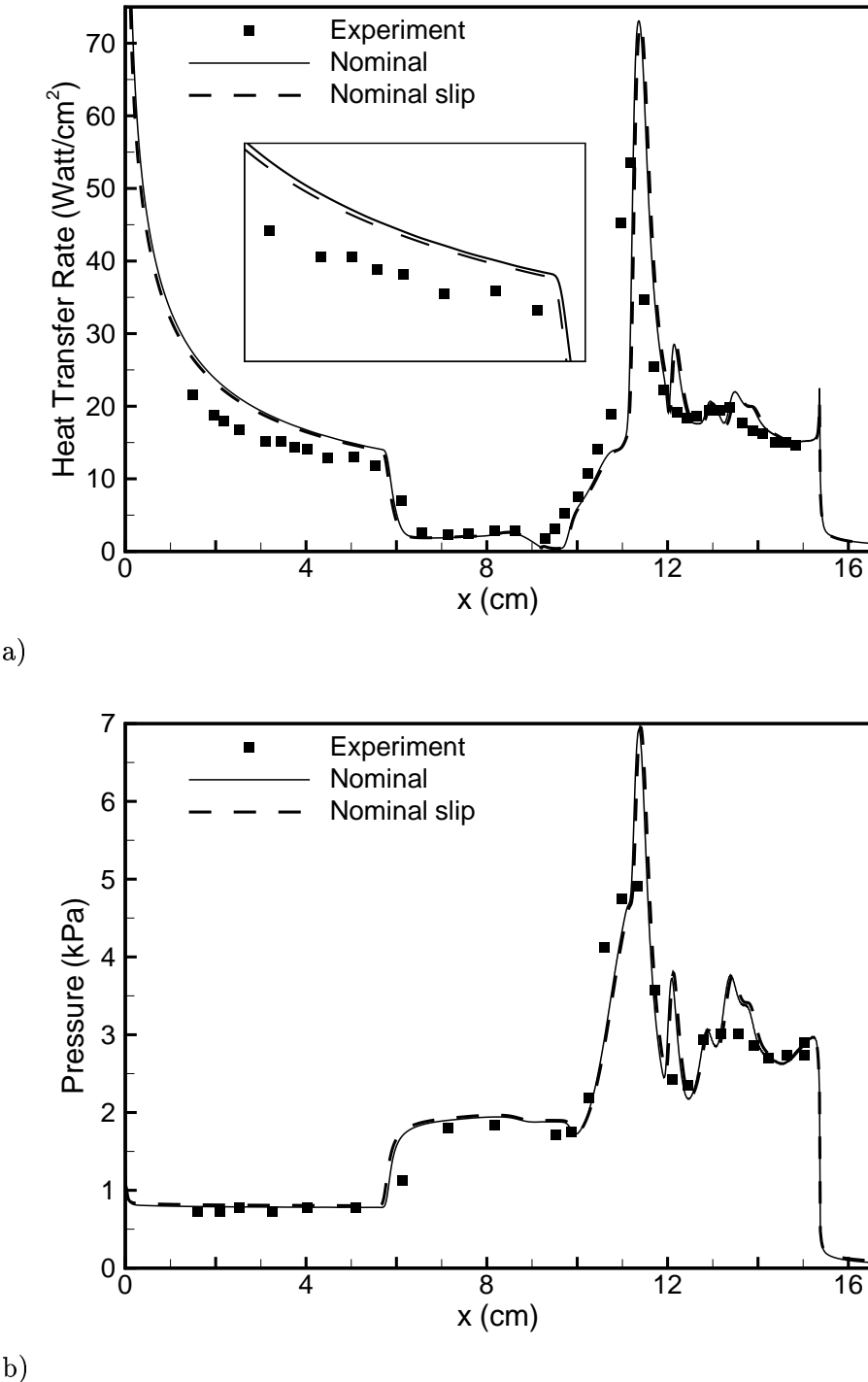


Fig. 6.2 Heat transfer rate and surface pressure for nominal Run 35 conditions.

little effect, with the largest difference being the heat transfer to the first cone, which decreases by less than 3%. Therefore, slip is not by itself responsible for the over-prediction of heat transfer to the first cone.

We observe a more significant decrease in heat transfer rate at the first cone when the computed nonequilibrium test-section conditions are employed, as shown in Fig. (6.3). The heat transfer rate decreases by 9.8% on the first cone, and the surface pressure decreases by 4.7% in that region, better matching the experimental data. The pressure in the separation zone is also reduced (by 6.3%), improving the agreement with the experiment. Note that the separation point and the locations of the peak heat transfer and pressure do not change substantially. However, the heat transfer rate and pressure on the last 2 cm of the second cone are reduced by 11% and 8.1%, respectively. We also employed the slip model using the nonequilibrium test-section conditions with the same accommodation coefficients. There is no significant difference in surface properties, with heat transfer being reduced by less than 2.0%. Thus, including both vibrational nonequilibrium in the nozzle and surface slip, the heat transfer to the first cone is reduced by 12%, and the difference is still greater than the experimental uncertainty.

Note that at the predicted nonequilibrium test-section conditions, the vibrational temperature is highly elevated. Therefore, the gradient of vibrational energy at the room-temperature surface is large, and the modeling of vibrational energy accommodation is important. Theory and experiments suggest that the vibrational energy accommodation coefficient should be much smaller than the value of 0.5 used in the previous simulations. Therefore, we simulated Run 35 with the nonequilibrium conditions and $\sigma_v = 0.001$; the results are plotted in Fig. (6.4). The pressure distribution and separation zone size are unaffected. But the predicted heat transfer rate on the first cone decreases by an additional 7.0%, to within the 5% uncertainty in the data. Interestingly, the predicted heat transfer to the back half of the second cone is now below the measurements.

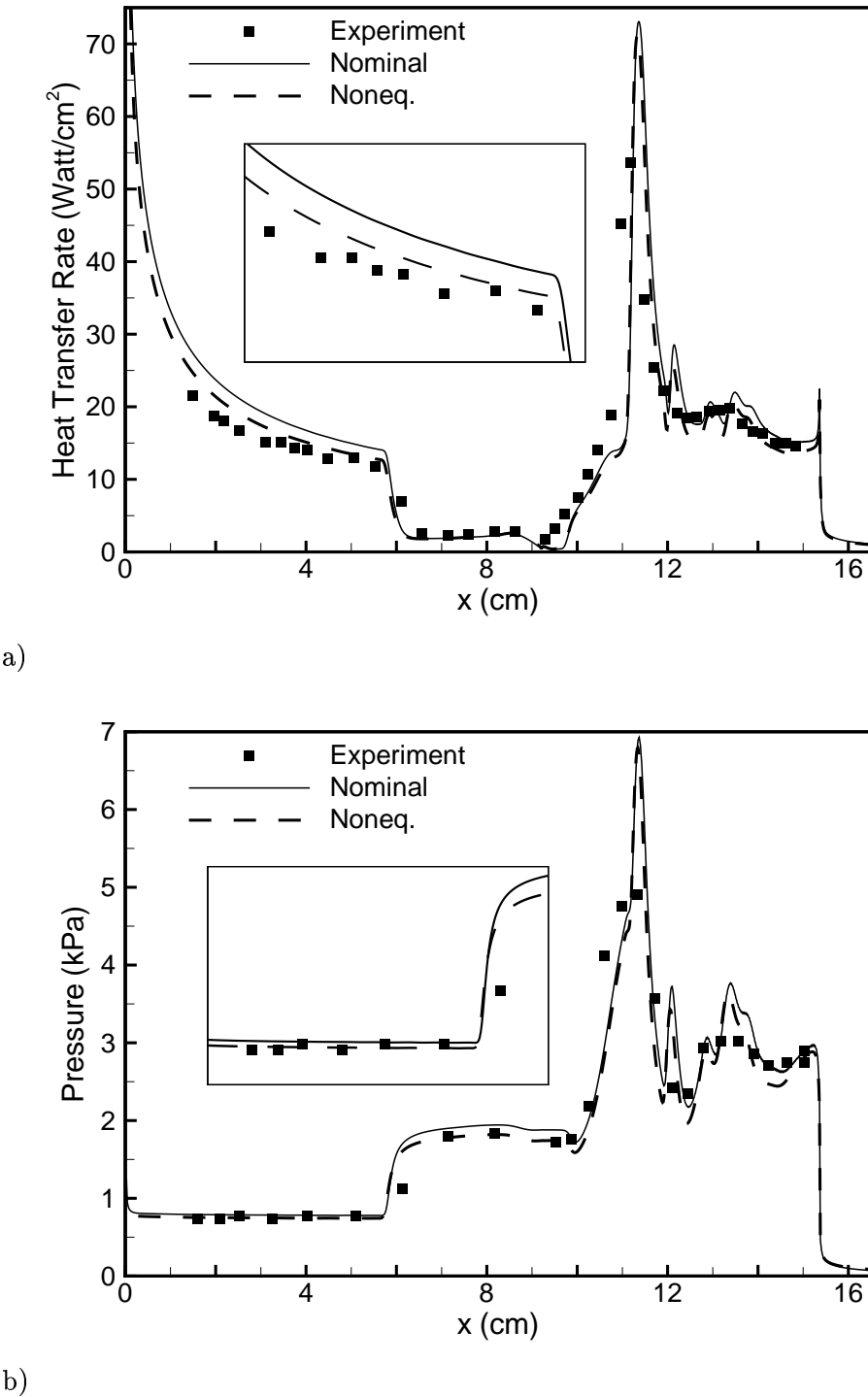


Fig. 6.3 Heat transfer rate and surface pressure for nonequilibrium Run 35 conditions.

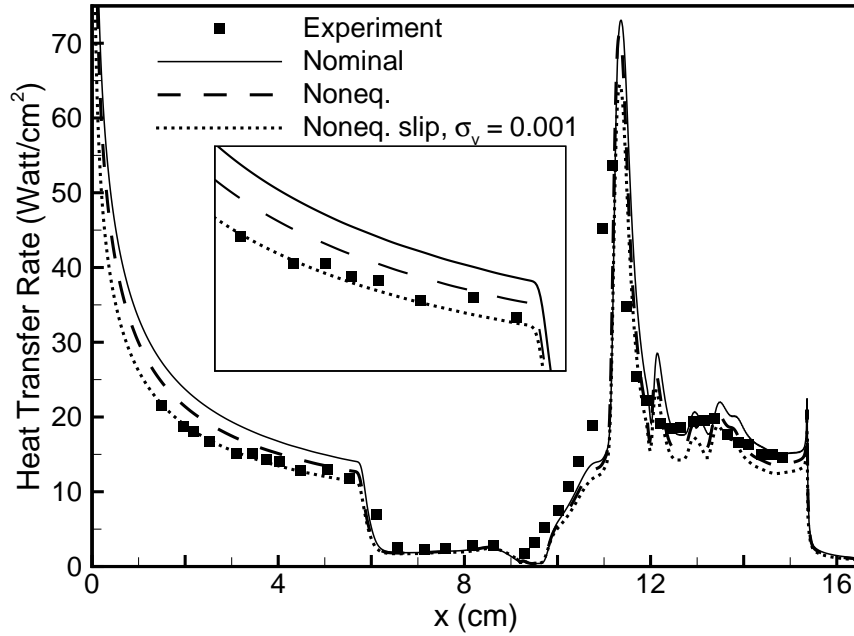


Fig. 6.4 Heat transfer rate for nonequilibrium Run 35 conditions and $\sigma_v = 0.001$.

Clearly vibrational nonequilibrium plays an important role in these flows. It affects the test-section conditions by reducing the flux of kinetic energy. And because of weak vibrational accommodation, a large fraction of the free-stream vibrational energy is not transferred to the surface near the tip.

An additional non-ideal effect is the weak non-uniformity in the test-section flow. Fig. (6.5) plots the computed Mach number contours in the test-section, with the double-cone flow field superimposed at the test location. To assess the effect of the flow non-uniformity, we extract flow conditions along a line that corresponds to the location of the inflow boundary condition for the double-cone simulation. Fig. (6.6) compares this calculation with the previous $\sigma_v = 0.001$ result. The free-stream non-uniformity reduces the size of the separation zone by 3.6 mm, shifting the heat transfer peak upstream in better agreement with the data. Also note improved agreement on either side of the peak.

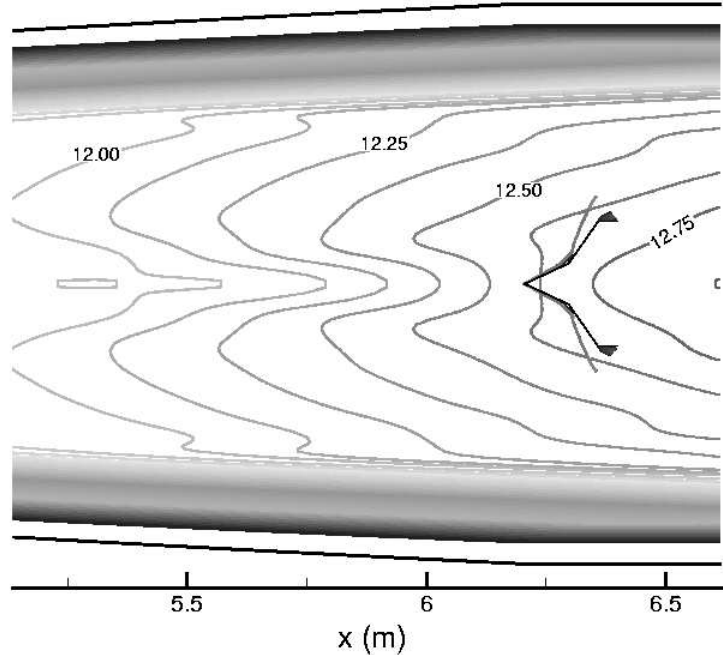


Fig. 6.5 Computed Mach number contours in the test-section and with double-cone flow solution superimposed.

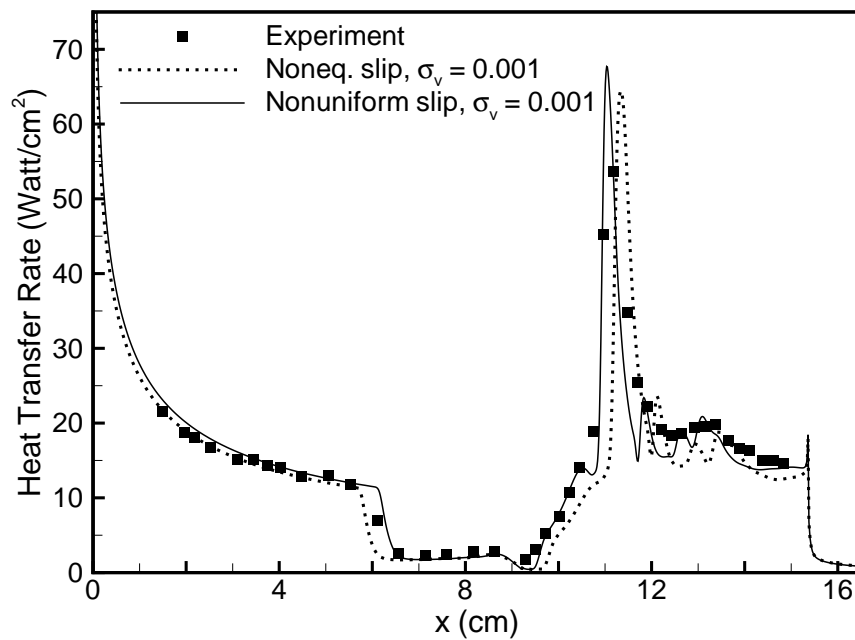


Fig. 6.6 Heat transfer rate for non-uniform Run 35 conditions and $\sigma_v = 0.001$.

Now consider the analysis of Run 28. At nominal test conditions, slip has little effect, as in Run 35. Fig. (6.7) shows that when we use the computed nonequilibrium test-section conditions, the heat transfer rate to the first cone is reduced by just 2.1%, which is consistent with the small (2.6%) reduction in the kinetic energy flux for this case. Fig. (6.7) also shows that the nonequilibrium conditions produce a significantly larger separation zone, apparently worsening the agreement with experiment. Fig. (6.8) shows that vibrational energy slip decreases the heat transfer rate by 11%, bringing it within about 8.7% of the measurements. However, the size of the separation zone increases. Fig. (6.9) shows the effect of test-section non-uniformity for Run 28. The simulations now agree well with the data, due to a smaller predicted separation zone and a slightly reduced heat transfer rate to the first cone.

These results show that including vibrational energy freezing in the nozzle, weak vibrational accommodation to the model surface, and test-section non-uniformity gives excellent agreement between computations and experiments. It should be noted that these experiments were run in pure nitrogen at low pressures, which tends to enhance the effects of vibrational nonequilibrium. Also the non-uniformity of the test-section is likely increased by the low pressure conditions, which result in thicker boundary layers and non-ideal nozzle performance. Therefore, it is likely that under the usual operating conditions of the LENS facility (air at orders of magnitude larger pressure) these effects will be diminished. However further studies are required to quantify this statement.

6.5 Under-resolved Solutions

In this section we discuss the effect of grid resolution on the double-cone flows, and show that if the flow field is under-resolved it is possible to obtain good agreement with experiments for the wrong reason. The computations presented in the previous section are computationally demanding because the recirculation zone develops slowly and a large physical time must be simulated to reach steady state.

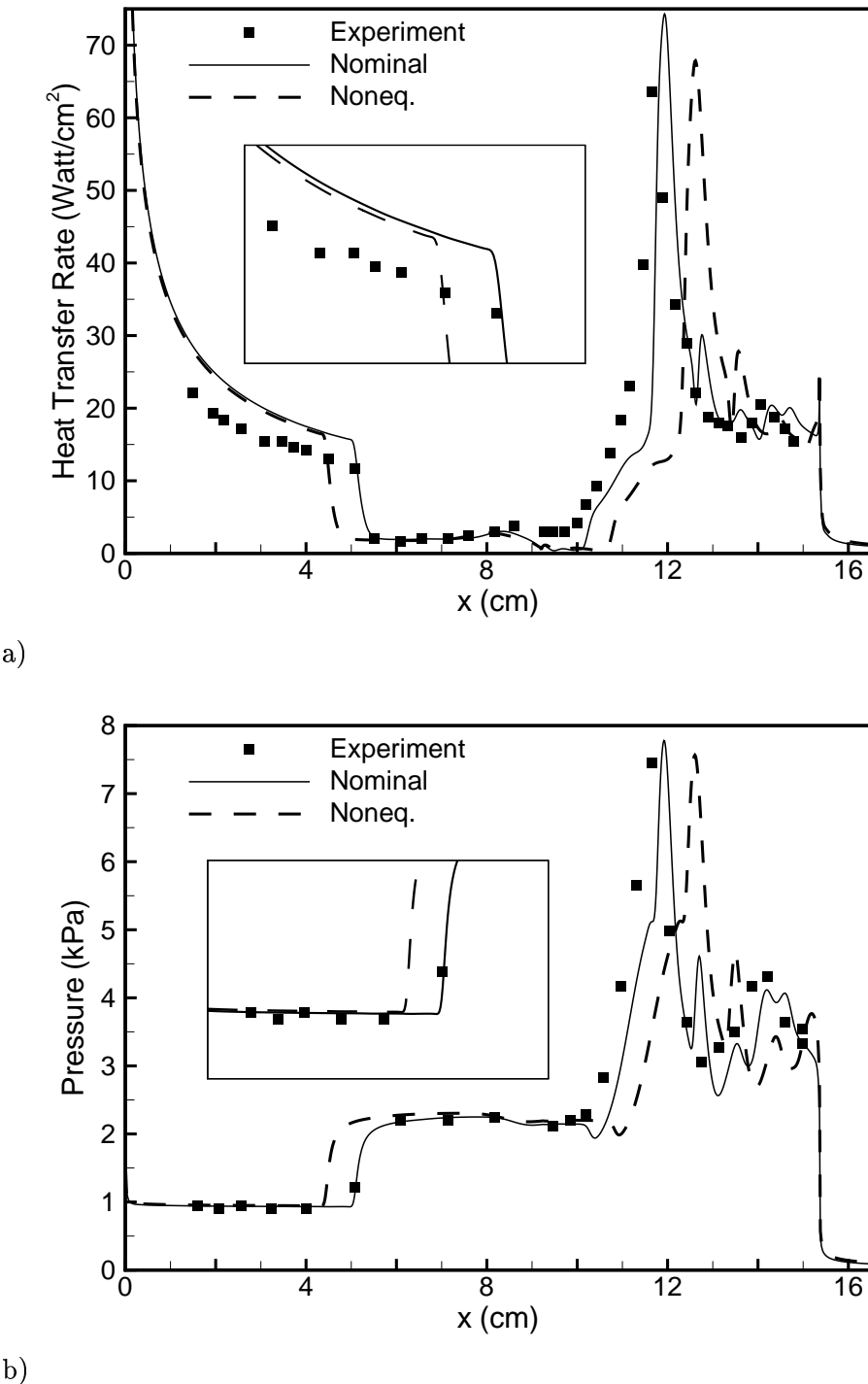


Fig. 6.7 Heat transfer rate and surface pressure for nonequilibrium Run 28 conditions.

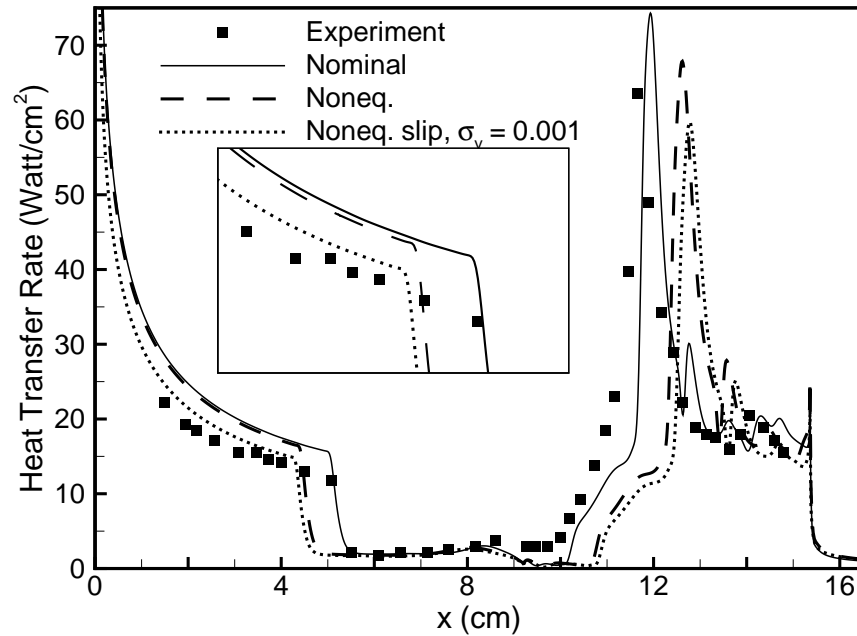


Fig. 6.8 Heat transfer rate for nonequilibrium Run 28 conditions and $\sigma_v = 0.001$.

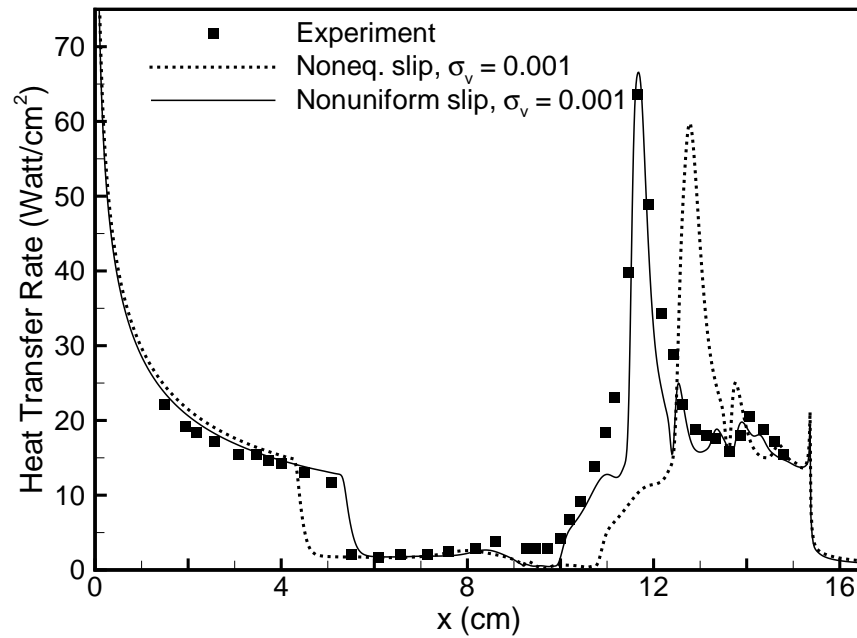


Fig. 6.9 Heat transfer rate for non-uniform Run 28 conditions and $\sigma_v = 0.001$.

In addition, large finely-spaced grids must be used to ensure grid-converged results. For example, to capture the initial boundary layer growth at the cone tip, our first grid point is located $0.1 \mu\text{m}$ from the surface.

Let us study how the solution varies when the flow is under-resolved. Fig. (6.10) plots the heat transfer rate at nominal and nonequilibrium conditions for Run 28 using a 256×128 grid. The coarse grid solutions produce smaller separation zones, and as a result the nonequilibrium calculation appears to give the “correct” extent of separation. However, Fig. (6.11) shows that when we include the additional effects of small vibrational energy accommodation and flow non-uniformity, the coarse grid no longer agrees so well with the experiments. This is an excellent illustration of the importance of performing a rigorous grid convergence study, preferably without knowledge of the data.

6.6 Results for Low Density Experiments

In this section we present simulation results of double-cone experiments performed at very low density nitrogen and specific enthalpy approximately equal to that of Run 35. These low density double-cone experiments were performed following the initial blind comparisons with experimental data, and were designed to be used as validation cases for particle-based methods such as the Direct Simulation Monte Carlo (DSMC) method. The reason for performing additional double-cone experiments with substantially lower free-stream densities is to make the problem more tractable for the DSMC codes by reducing the computational cost. The cost of particle-based simulations increases with the number of computational particles that must be simulated. The existing double-cone experiments were designed to be in the continuum regime. This, combined with the large amount of physical time that must be simulated for the double-cone flow to reach steady state make the DSMC simulation prohibitively expensive.

We present simulation results for two low density cases: Run 4 and Run 5. The experimental conditions for these cases were designed to result in low density

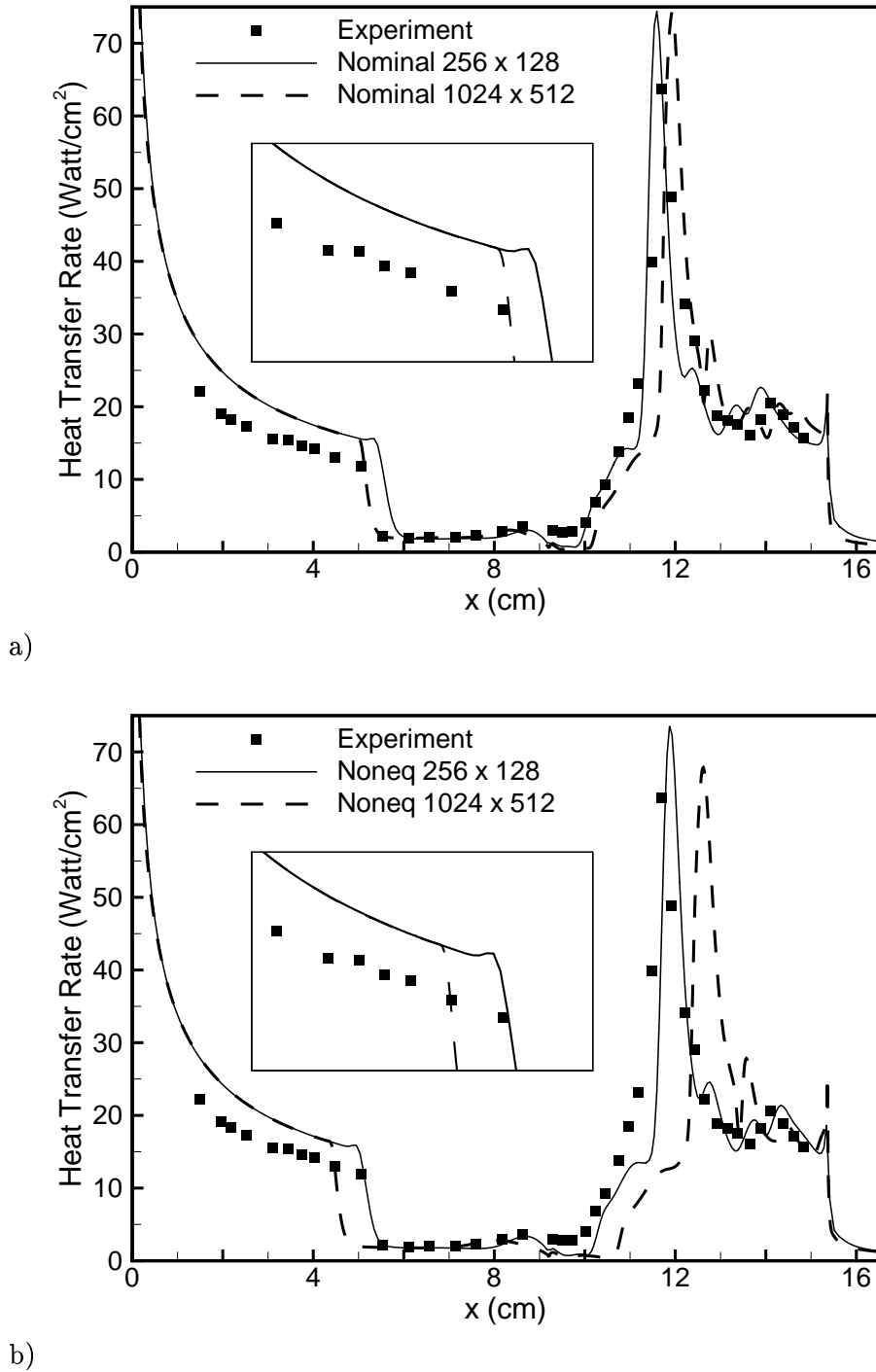


Fig. 6.10 Heat transfer rate for (a) nominal and (b) nonequilibrium Run 28 conditions computed on the coarse grid (256 x 128).

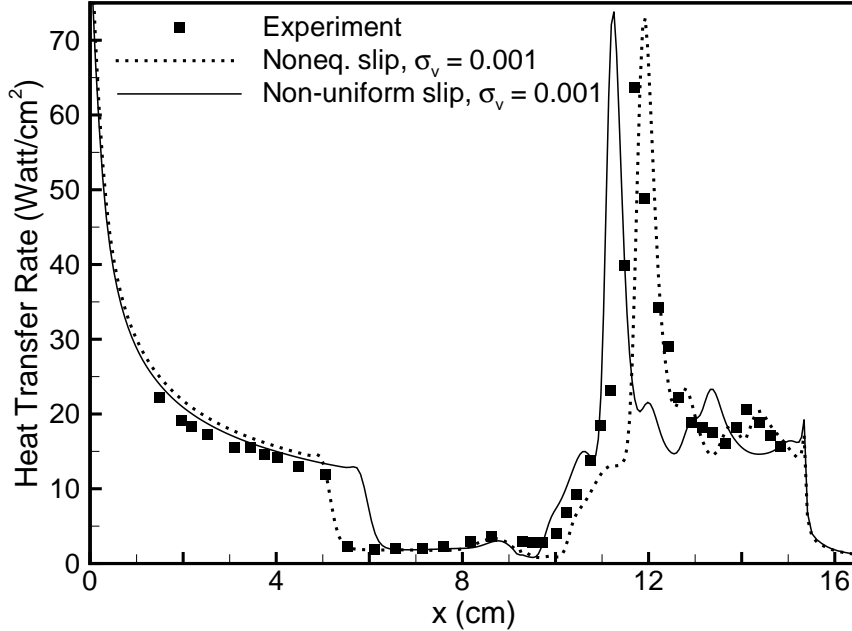


Fig. 6.11 Heat transfer rate for non-uniform Run 28 conditions with $\sigma_v = 0.001$ computed on the coarse grid (256×128).

free-streams, with approximately 1/2 and 1/3 the free-stream density of Run 35. These are Run 4 and Run 5, corresponding to the 1/2 density and 1/3 density conditions respectively. The free-stream conditions for these cases are listed in Table (6.3). The free-stream conditions were obtained assuming vibrational nonequilibrium in the nozzle flow, and we see that there is vibrational energy frozen in the flow as was the case for Run 28 and Run 35.

Case	Run 4 “1/2 density”	Run 5 “1/3 density”
M_∞	15.90	15.27
Re_m ($10^3/m$)	109.0	55.5
T_∞ (K)	46.58	52.99
$T_{v\infty}$ (K)	2027.1	2128.4
T_{wall} (K)	294.48	292.78
ρ_∞ (10^{-3} kg/m ³)	0.3020	0.1606
u_∞ (m/s)	2213.6	2266.4

Table. 6.3 Free-stream and wall conditions for the “1/2 density” (Run 4) and “1/3 density” (Run 5) 25° - 55° sharp double-cone LENS experiments.

Fig. (6.12) shows the results of simulations for Run 4, and the heat transfer rate to the body is plotted for two simulations along with the experimental measurements. The simulation under free-stream conditions with vibrational nonequilibrium included shows good agreement with the measurements everywhere, with the exception of the heat transfer rate to the first cone. This result is consistent with our previous analysis of Run 35 and Run 28. When the effects of slip are included in the simulation and the accommodation coefficient for vibrational energy is set to a very small value (0.001), the heat transfer rate to the first cone is reduced by approximately 10%, and good agreement is observed for the 1/2 density case. It is also interesting to note that there is very good agreement between both simulations and the measurements on either side of the peak in heat transfer rate and on the second cone. However, it is surprising that the location of the peak heating is predicted correctly, while the separation zone size is under-predicted by about 2 mm. This is probably due to slight non-uniformity in the test-section, as was the case for Run 35.

Fig. (6.13) plots similar heat transfer rate results for Run 5. The separation zone size is predicted correctly, and the separation region is much smaller for this case than the higher density case (Run 4). This is because the free-stream Reynolds number is much lower for this case, and this result is consistent with results of previous studies. The heat transfer rate to the first cone is over-predicted by about 10% with the no-slip simulation. However, the heat transfer rate to the first cone is lowered and is within the experimental 5% uncertainty when slip effects with weak vibrational energy accommodation to the surface are modeled.

From these simulation results we see that the effect of vibrational nonequilibrium in the free-stream and non-continuum effects on the surface are present in double-cone flows of different free-stream Mach and Reynolds numbers. This shows that we have correctly identified the source of the initial discrepancies and our analysis is valid.

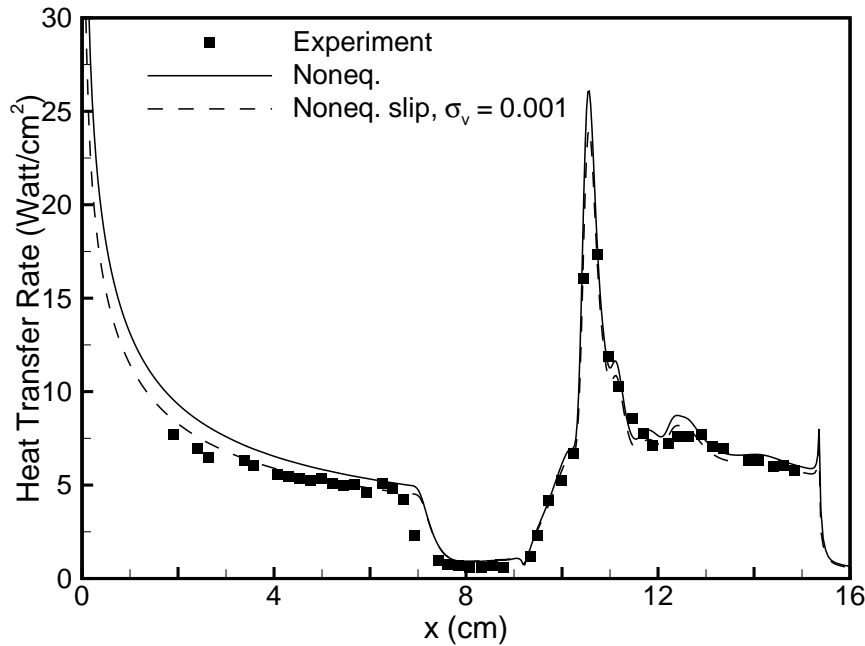


Fig. 6.12 Heat transfer rate for nonequilibrium Run 4 conditions with $\sigma_v = 0.5$ (solid line) and $\sigma_v = 0.001$ (dashed line).

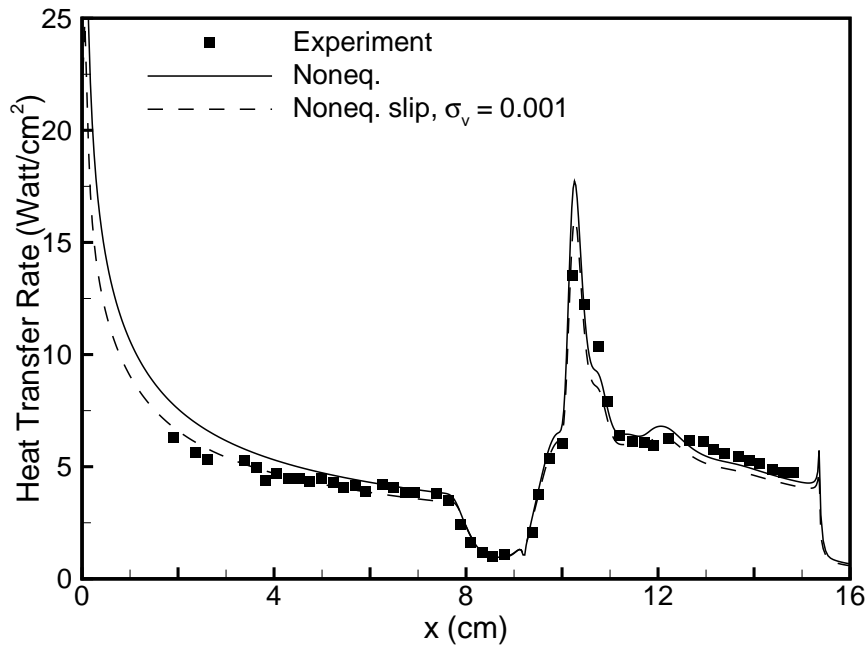


Fig. 6.13 Heat transfer rate for nonequilibrium Run 5 conditions with $\sigma_v = 0.5$ (solid line) and $\sigma_v = 0.001$ (dashed line).

6.7 Conclusions

In order to understand why discrepancies were observed between initial numerical simulations and the experiments presented in chapter 4, we investigated effects of vibrational nonequilibrium, slip at the model surface, and weak flow non-uniformity. We simulated the flow within the facility nozzle, and found that under the low pressure conditions of the experiment, the vibrational energy freezes near the throat temperature. This reduces the kinetic energy flux in the nozzle test-section, reducing the heat transfer to the model. However, the heat transfer rate was still over-predicted. Therefore, we considered the failure of the no-slip boundary condition at the model surface. We found that the computed heat transfer rate is sensitive to the vibrational energy accommodation coefficient. Using experimental values, the heat transfer to the first cone is predicted to within the 5% measurement uncertainty. Finally, we used the results of our nozzle flow field predictions as inflow to the double-cone flow solution. These simulations accounted for small levels of flow non-uniformity in the test-section, and show an improvement in the size of the separation zone and the heat transfer rate to the second cone.

In this study, we also illustrated the importance of conducting careful grid convergence studies. Because the computed separation zone size depends on the grid resolution, it is possible to obtain spurious “agreement” with experiments due to poor grid resolution and inadequate modeling of the flow physics.

Chapter 7

High Enthalpy Double-Cone Experiments

7.1 Introduction

In this chapter we present simulations of double-cone flow experiments at high enthalpy free-stream conditions performed at the LENS facility. These experiments were conducted through a joint computational and experimental effort, based on the methodology for characterizing experiments that was presented in the previous chapter. This approach was successful in developing improved test conditions and physical models for low enthalpy nitrogen experiments.

The present experiments are of high enthalpy hypersonic flows, characteristic of flight at a Mach number of about 14. New experiments have been performed using the LENS Leg I tunnel at these conditions for both nitrogen and air. The flow in the facility nozzle is simulated, and flows over double-cones are computed at the nominal test conditions, and at the conditions predicted by the nozzle simulations.

7.2 Design of High Enthalpy Experiments

In previous work [Nompelis *et al.* (2003a)], we performed simulations of the flow of air in the nozzle near the maximum LENS Leg I enthalpy conditions ($h_o = 11.5$ MJ/kg, $p_o = 59$ MPa). We systematically lowered the reservoir pressure, keeping the total enthalpy constant, and simulated the flow in the nozzle from the driven section to the nozzle exit-plane. We obtained computed free-stream conditions for four different reservoir conditions; the existing conditions of $p_o = 7380$ psi and three additional cases (6000, 4000, and 2000 psi). Then, we simulated the flow over the double-cone model under the corresponding computed test-section conditions that we obtained from the nozzle flow simulations. In order to determine whether flows

under these proposed conditions are laminar, we examined the shear layer that forms at the edge of the separation, which is the most unstable region of the flow. We compared the shear layer Reynolds numbers with the Birch and Keyes criterion for transition in free shear layers formed by shock interactions [Birch and Keyes, (1972)]. Based on this analysis, we found that the double-cone flows generated under the two lowest stagnation pressure conditions will likely be laminar. These results are consistent with previous laminar double-cone flows under low enthalpy conditions.

Experiments were performed at the proposed lower pressure conditions in the LENS I facility and measurements were made over the re-instrumented double-cone model. Under these low-pressure conditions, we anticipated that there would be some level of chemical reaction and vibrational nonequilibrium in the free-stream. Thus, the effects of chemical reactions and energy relaxation in the nozzle were taken into consideration when inferring the free-stream conditions. Determination of the free-stream conditions involves performing measurements of the Pitot pressure at the nozzle exit-plane using Pitot probes. We performed simulations including real-gas effects of the flow around the Pitot probes and found that the Pitot pressure is measured accurately by the probe under high enthalpy conditions. Once the Pitot pressure at the test-section is known, a quasi one-dimensional code is used to expand the reservoir conditions and match the Pitot pressure. Finite-rate chemistry with vibrational relaxation of the gas has been integrated in this algorithm. The vibrational state of the gas is computed based on a vibrational state-specific model for nitrogen and a vibrational equilibrium model for air. This assumption of vibrational equilibrium is based on previous experience at Calspan with high enthalpy shock tunnel flows and because of the difficulty of predicting coupled vibrational relaxation and recombination in expanding air. The free-stream conditions for high enthalpy experiments in pure nitrogen and air are listed in Table (7.1). Note that there is a substantial degree of vibrational nonequilibrium in the nitrogen flow.

Also in the air flow, there is some NO and O in the free-stream as predicted by this analysis, and therefore chemical energy is stored in the gas.

Case	Run42 (nitrogen)	Run 46 (nitrogen)	Run 43 (air)
M_∞	11.52	11.54	8.87
Re_m ($10^3/m$)	333.4	439.4	306.6
T_∞ (K)	268.7	281.7	576.0
$T_{v\infty}$ (K)	3160	3072	576.0
T_{wall} (K)	294.7	296.3	296.2
ρ_∞ (g/m ³)	1.468	1.958	2.134
u_∞ (m/s)	3849.3	3946.9	4218.1
c_{N_2}	1.00000	0.99842	0.73704
c_{O_2}	-	-	0.17160
c_{NO}	-	-	0.06477
c_N	0.00000	0.00158	0.00000
c_O	-	-	0.02659

Table. 7.1 Nominal free-stream and wall conditions for the 25-55° sharp double-cone high enthalpy experiments.

7.3 High Enthalpy Double-Cone Flows

We simulated the flow over the double-cone model under the nominal conditions for the nitrogen and air cases. A schematic of the high enthalpy double-cone flow in nitrogen (Run 42) is shown in Fig. (7.1). The interacting shocks create a massive region of separation that extends to about half the length of the first cone. The shear layer that forms at the edge of the separation is about 6 cm in length. A supersonic jet is formed near the surface of the second cone. Interestingly, there are two regions behind the bow shock where the flow is subsonic. Fig. (7.2) plots the surface pressure and heat transfer rate for Run 42. In general, agreement between the simulation and the experimental measurements is very good. The size of the separation zone is almost exactly reproduced, as well as the location of the pressure peak on the second cone. Surprisingly, the pressure is under-predicted along the first cone and in the separation region, by 10% and 5% respectively. The heat transfer is also under-predicted along the first cone and at the peak. Also, the heat transfer peak in the experiments appears to be wider than the simulation predicts.

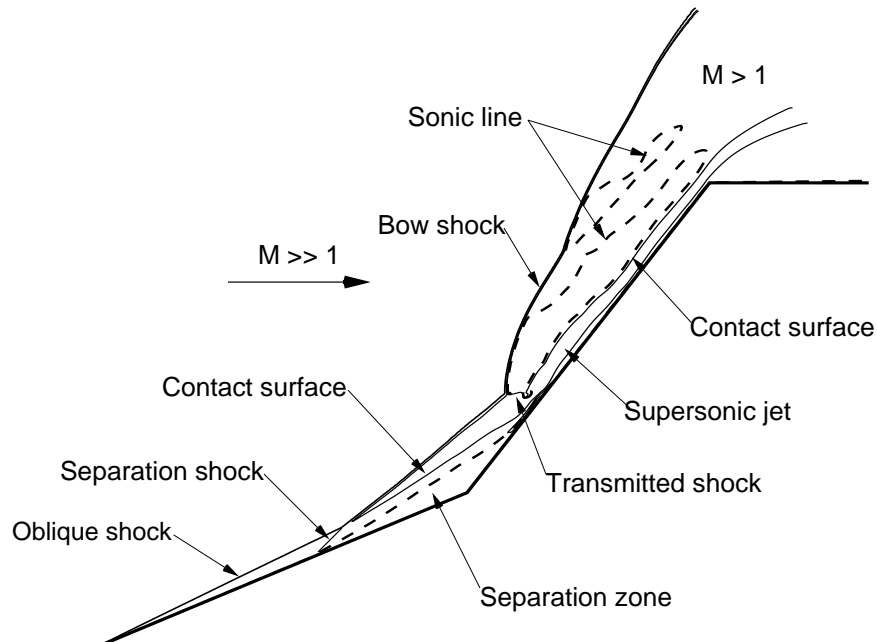
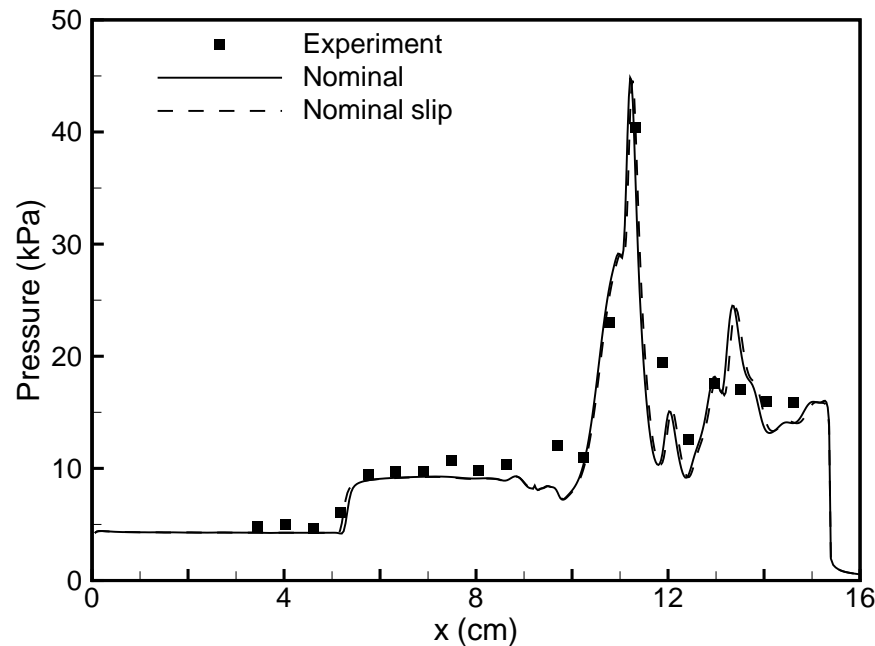


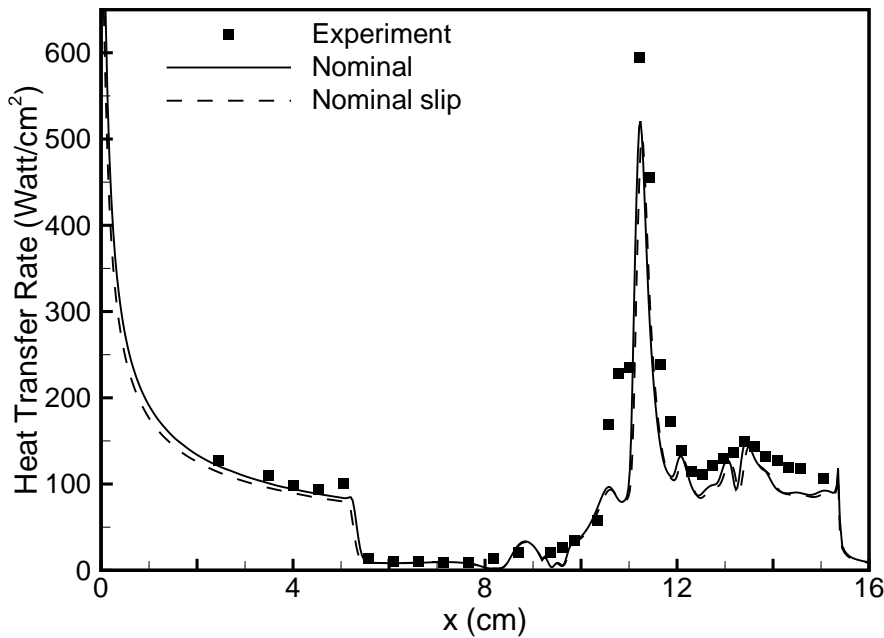
Fig. 7.1 Schematic of double-cone flow-field at high enthalpy nitrogen free-stream conditions (Run 42).

The effect of slip on the heat transfer rate is more pronounced along the first cone, while the pressure is unaffected. This result is consistent with the low enthalpy Run 35 results.

Fig. (7.3) plots the results for Run 46, which is nitrogen at a 40% higher stagnation pressure than Run 42. The higher Reynolds number results in a slightly larger separation zone, as expected. We see that the agreement is good. However we under-predict the size of the separation zone, and in general the predicted heat transfer and pressure is slightly low. It is unlikely that this difference is due to transition to turbulence, because the flow at the forebody is certainly laminar, and heat transfer rate is predicted to be low there.



a)



b)

Fig. 7.2 Surface pressure (a) and heat transfer rate to the model (b) for high enthalpy nitrogen free-stream conditions (Run 42).

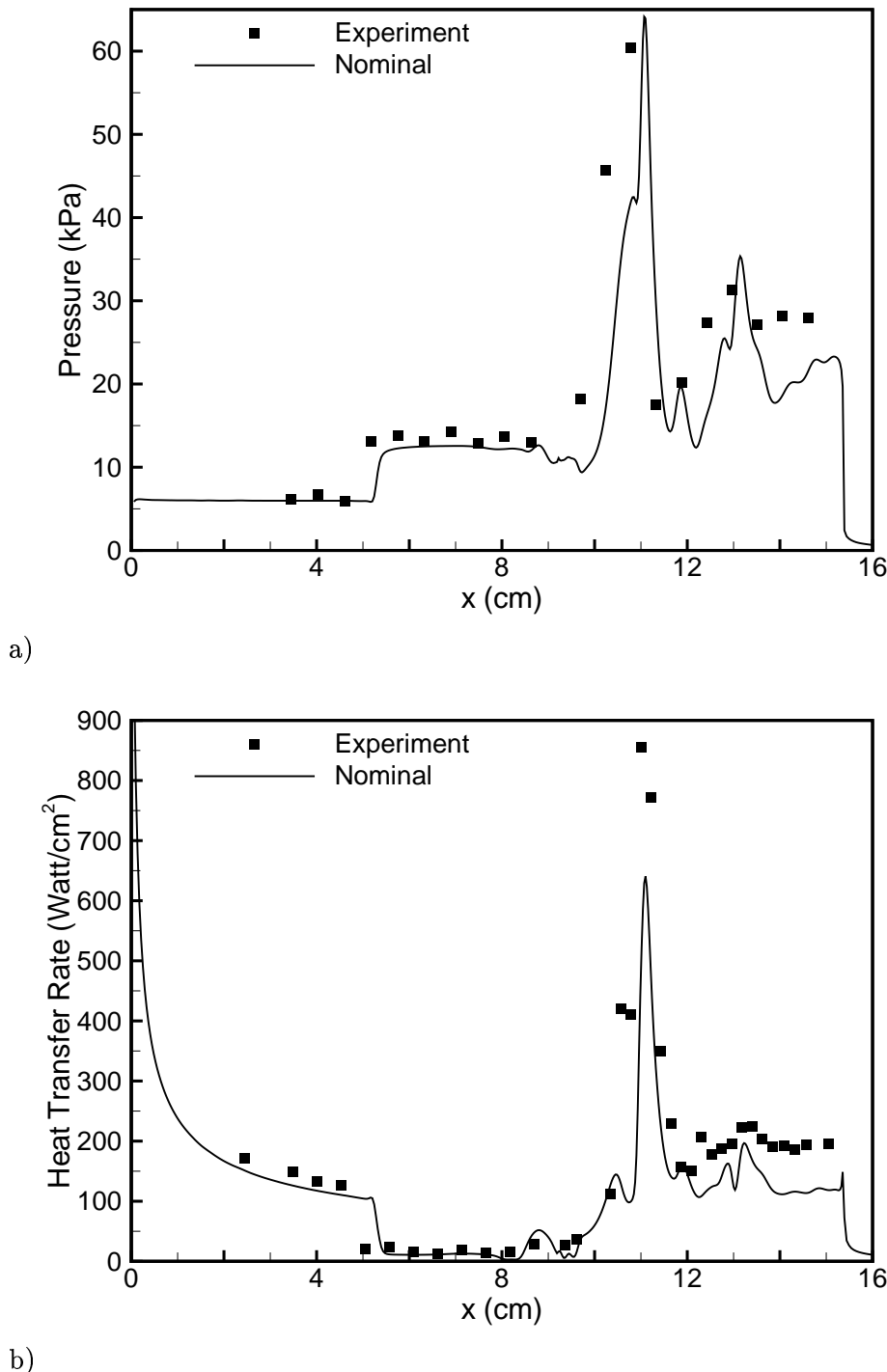
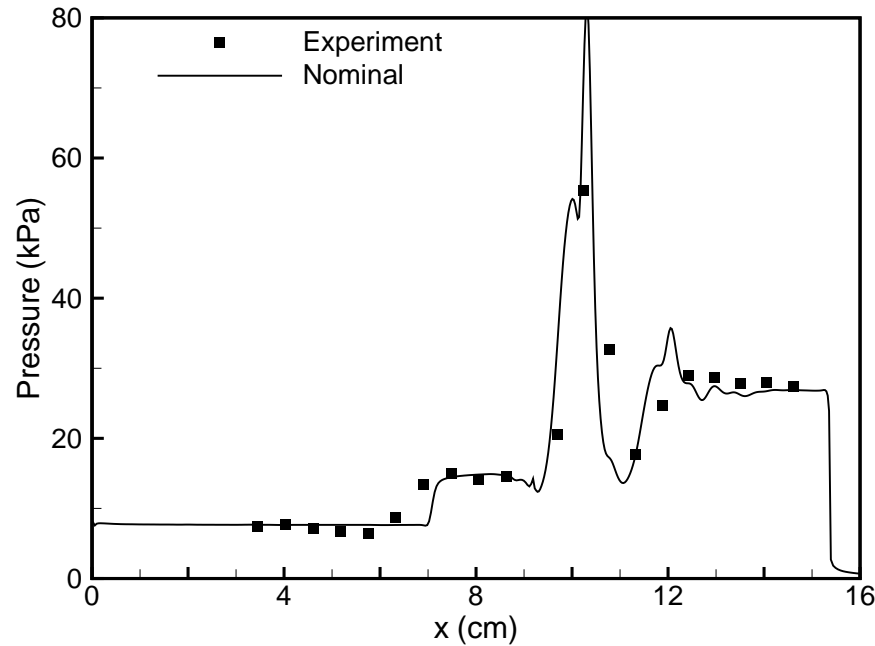


Fig. 7.3 Surface pressure (a) and heat transfer rate to the model (b) for high enthalpy nitrogen free-stream conditions (Run 46).

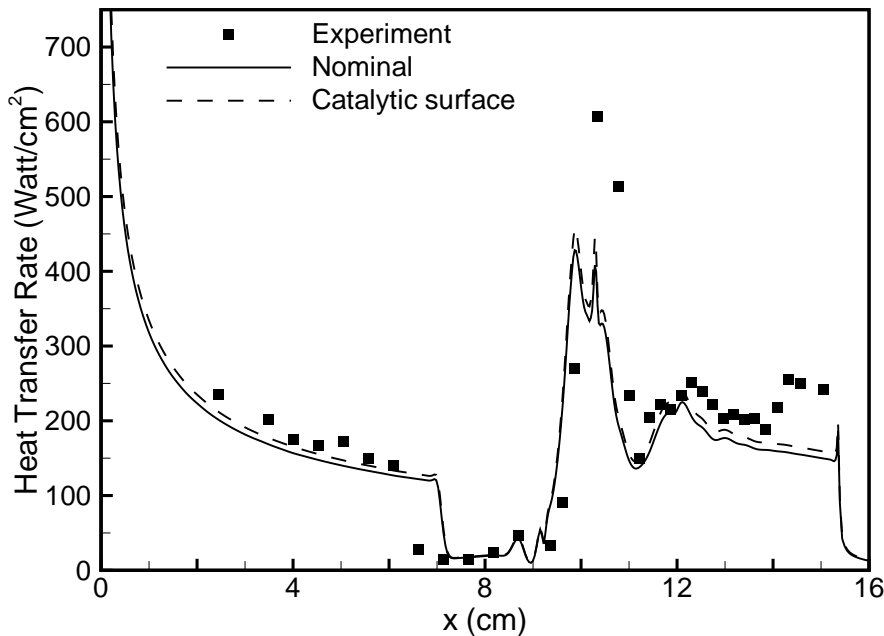
Fig. (7.4) shows a comparison between experimental measurements and simulation results for the air case (Run 43). The size of the separation zone is not predicted correctly, although the basic flow has been captured by the CFD. The heat transfer rate is under-predicted by about 30% in the shock interaction region, and the heat transfer rate to the second cone is also significantly under-predicted (by 20-30%). In general, the size of the separation zone affects the location of the peak and the strength of the interaction. In this case, the small separation zone results in having the peak in heat transfer slightly upstream from what the experiments show. Surface catalysis is not responsible for this large disagreement as shown by the fully catalytic simulation (catalytic efficiency was set to unity at the wall).

The flowfields generated under the new experimental conditions appear to be fully laminar. We computed the shear layer Reynolds numbers based on the Birch and Keyes definition, and the results are plotted in Fig. (7.5). In this figure, the points represent the Reynolds number at different locations along the shear layer, computed based on the state of the gas on the high-speed side: $Re_s = \rho vs / \mu$, where s is the length along the shear layer. This dimensionless quantity remains under 20,000 for Run 42 and under 10,000 for Run 43, and this is well under the Birch and Keyes criterion for transition. The shear layer Reynolds numbers for the fully laminar low enthalpy Run 35 case are plotted for reference.

From these results we see that the high enthalpy nitrogen and air double-cone experiments are fully laminar and the free-stream conditions are calculated very accurately. Also, the results of the numerical simulation are mostly within the 5% experimental uncertainty for this effectively blind comparison. In view of the discrepancies observed initially for the low enthalpy experiments presented in chapter 4, this is encouraging, particularly given the uncertainty introduced by the air chemistry models employed. It should be noted that the magnitude of the peak in heat transfer rate is not reproduced, and the difference is significant. This discrepancy is common among all high enthalpy flow simulations presented here.



a)



b)

Fig. 7.4 Surface pressure (a) and heat transfer rate (b) to the model for high enthalpy air free-stream conditions (Run 43).

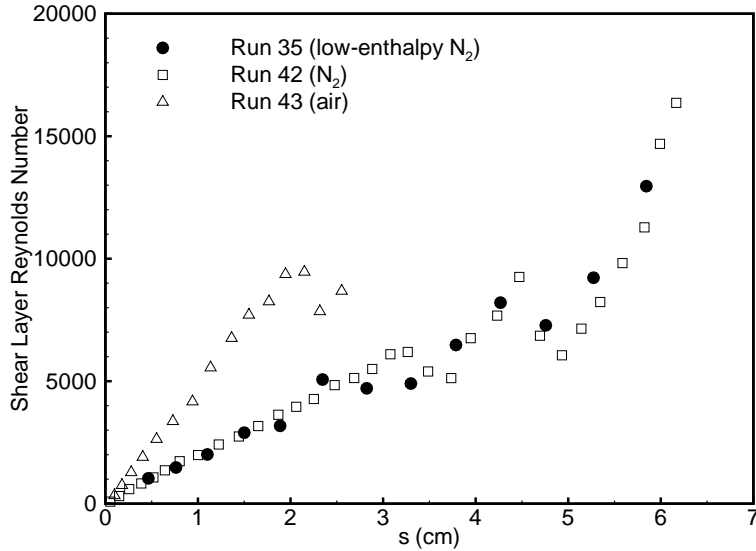


Fig. 7.5 Shear layer Reynolds numbers at the edge of the separation region calculated based on the Birch and Keyes definition for Run 42 and Run 43. The low enthalpy Run 35 result is plotted for reference.

7.4 Nozzle Flow Simulations

In this section we present nozzle flow simulations performed under the experimental conditions of Runs 42 and Run 43. Our objective is to provide additional characterization of the free-stream at the high enthalpy LENS conditions. The nozzle flow is simulated from the driven section, through the nozzle throat and into the contoured nozzle. The reservoir conditions are taken from direct measurements in the driven section, where thermochemical equilibrium is assumed. We use a 541×148 grid to represent the nozzle, and the grid is constructed from the nozzle geometry specification. In previous studies of the flow inside the LENS facility nozzle at low enthalpy conditions (chapter 6), we used the Baldwin-Lomax turbulence model for the nozzle wall boundary layer. This turbulence model did not reproduce the boundary layer thickness observed in the experiments. However, when we employed the Spalart-Allmaras model for wall turbulence the simulation matched the Pitot pressure profile at the nozzle exit-plane. In the present studies, we also employ the Spalart-Allmaras model for wall turbulence [Spalart and Allmaras, (1992)] with the compressibility correction from Catris and Aupoix (2000).

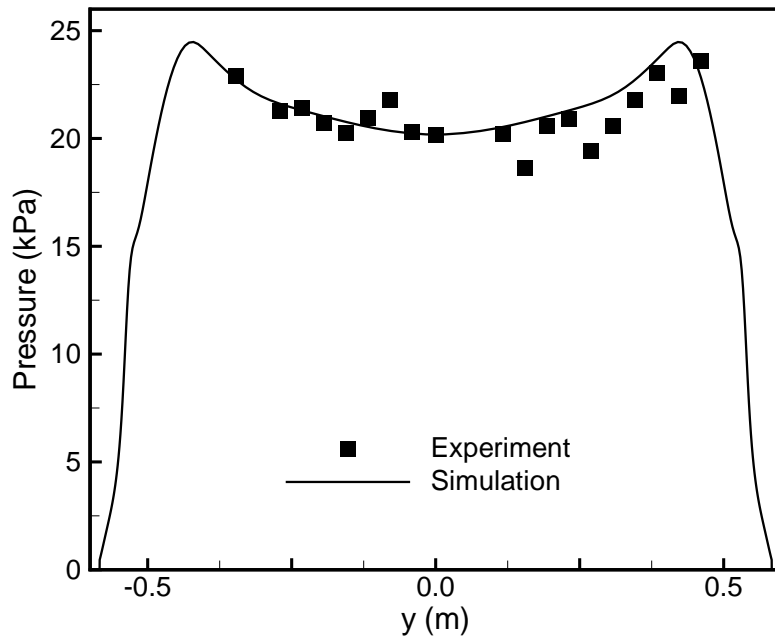


Fig. 7.6 Predicted and measured Pitot pressure profiles for the calibration run in nitrogen (Run 187).

Fig. (7.6) compares the computed exit-plane Pitot pressure profile with the probe rake measurements for the calibration case of Run 42 (Run 187). The numerical predictions match the measured values very well, without any adjustable constants in the calculation. Fig. (7.7) plots the velocity profiles at different locations along the nozzle wall plotted in wall variables. We see that the turbulence model closely resembles the logarithmic law of the wall in van Driest coordinates in the region of the throat (the subsonic region and the sonic point), as well as the expansion region ($M = 2$). This is a verification of the turbulence model implementation in the CFD. The profile progressively deviates from the log-law as the flow expands to the test-section. The more advanced turbulence model captures the reduction in the boundary layer thickness due to the favorable pressure gradient. Fig. (7.8) plots the heat transfer to the nozzle wall during the expansion under the calibration run conditions. The numerical results match the measured values, and the trend

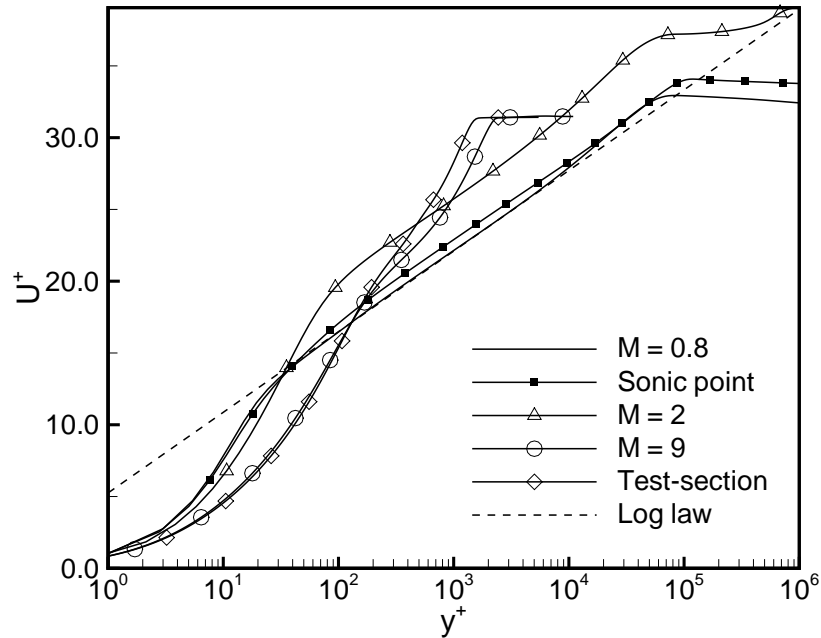


Fig. 7.7 Velocity profiles of the nozzle wall boundary layer from the Run 42 calibration case plotted in wall variables.

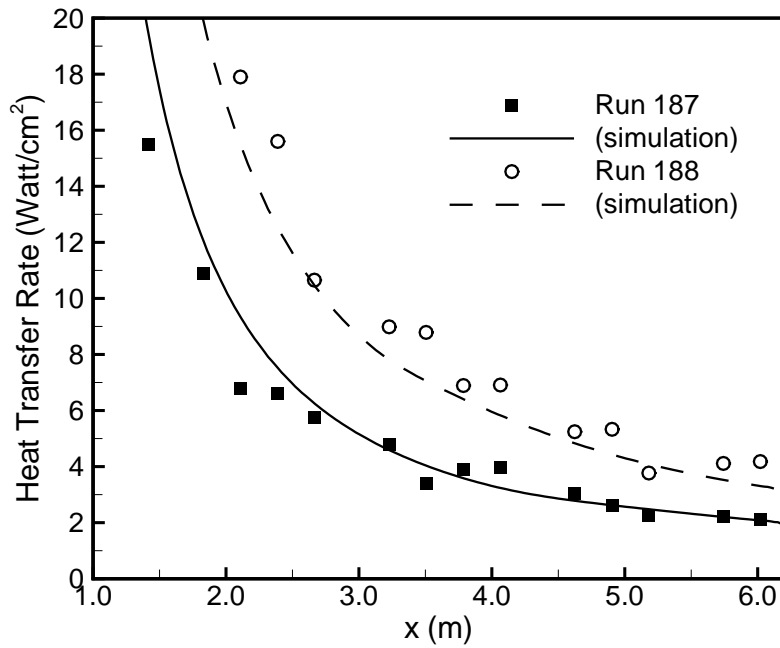


Fig. 7.8 Heat transfer rate predictions and measurements at the wall for Run 187 and Run 188.

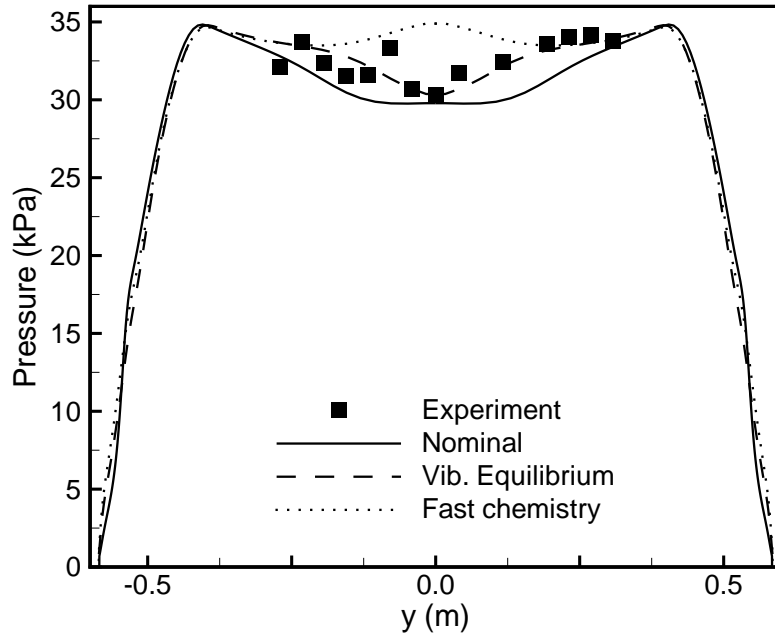


Fig. 7.9 Predicted and measured Pitot pressure profiles for the calibration run in air (Run 188).

is predicted correctly, indicating that the boundary layer is turbulent in the region where measurements could be made in the nozzle. This is contrasted to results of previous simulations in which the algebraic model for wall turbulence was used. Thus, the use of the Spalart-Allmaras turbulence model makes the nozzle simulations a more predictive tool. The Pitot pressure profile for the air calibration run (Run 188) is plotted in Fig. (7.9) along with the probe measurements. The baseline (vibrational equilibrium and nominal reaction rates) simulation does not predict the profile correctly, and is within 10% of the measured values. However, when we force the vibrational energy to be in equilibrium during the expansion, agreement with measurements is improved. In a similar fashion, if we force the chemical reaction rates to be faster by an order of magnitude for the vibrational equilibrium simulations, we observe a 15% increase in the Pitot pressure at the centerline. Thus, uncertainties in vibrational relaxation and reaction rate affect the predicted test-section conditions. The computed test-section conditions obtained

with the baseline simulations are tabulated in Table (7.2).

Case	Run 42 (nitrogen)	Run 43 (air)
T_∞ (K)	268.1	338.6
$T_{v\infty}$ (K)	3021.8	2103.8
ρ_∞ (10^{-3} kg/m ³)	1.486	1.832
u_∞ (m/s)	3886.5	4126.4
c_{N_2}	0.99765	0.74422
c_{O_2}	-	0.15099
c_{NO}	-	0.04898
c_N	0.00235	0.00000
c_O	-	0.05580

Table. 7.2 Computed test-section conditions for the 25-55° sharp double-cone high enthalpy experiments.

7.5 Simulations at Computed Conditions

In this section, we present simulations of the double-cone flows using the computed conditions presented in the previous section. Fig. (7.10) shows the computed pressure and heat transfer rate to the model under the computed conditions of Run 42. We see that the pressure and heat transfer rate to the first cone have increased by about 2%, but the overall agreement has not improved. This is not surprising, given that the computed test-section conditions are not very different from the nominal conditions listed in Table (7.1). This is because vibrational nonequilibrium was included in the quasi-one-dimensional calculation used to obtain the free-stream conditions for the nitrogen case.

Results of simulations of the air case (Run 43) under computed test-section conditions are plotted in Fig. (7.11). A fully catalytic surface model was employed for these simulations. The pressure and heat transfer rate are reduced by about 10-15% under conditions for vibrational and thermal equilibrium. These predictions substantially deviate from the measured values, and also the separation zone is under-predicted. At computed conditions obtained with the fast reaction rates for the nozzle flow, the numerical predictions are very close to those at the nominal conditions.

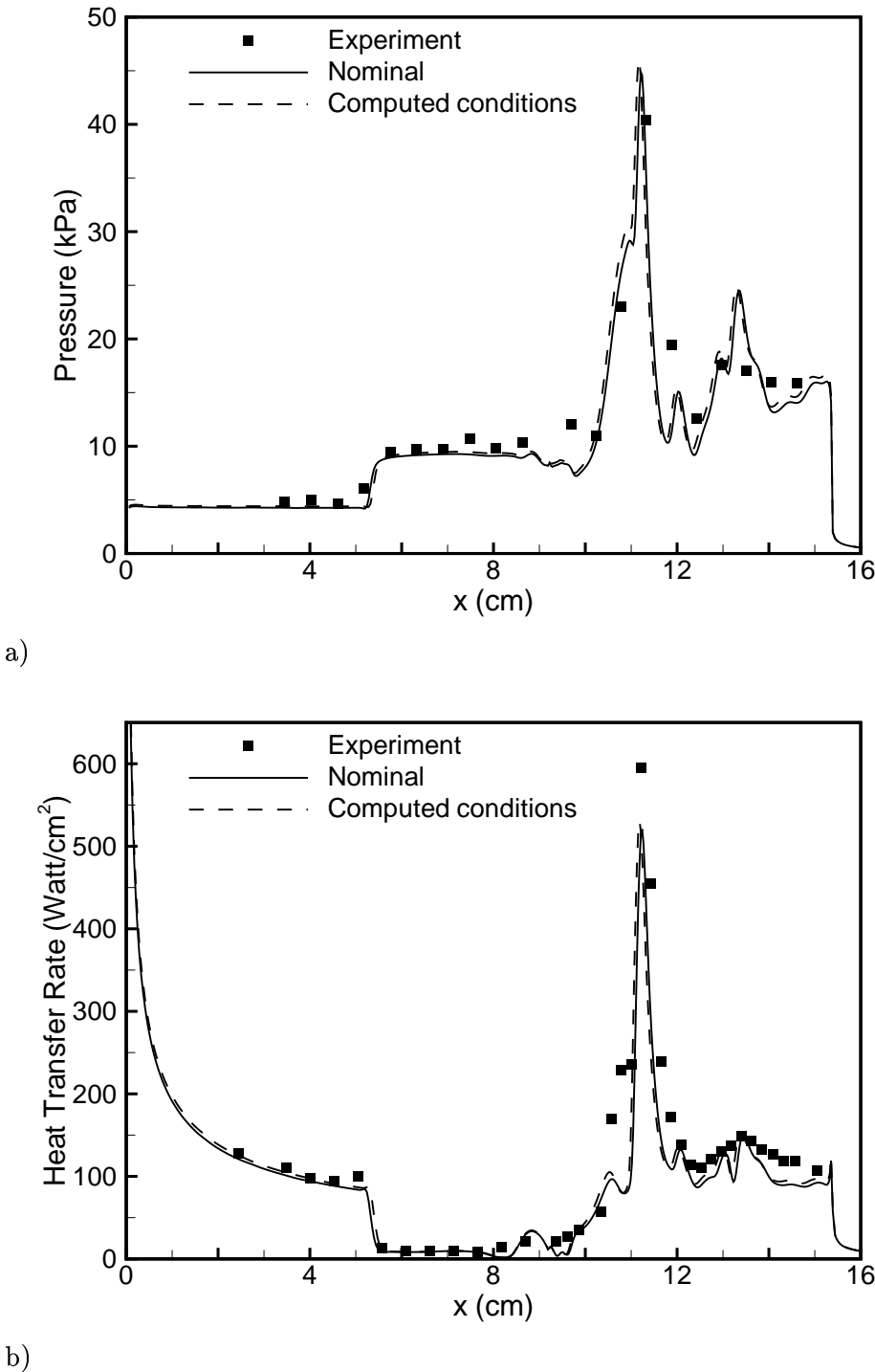


Fig. 7.10 Predicted surface pressure (a) and heat transfer rate (b) for Run 42 computed test-section conditions.

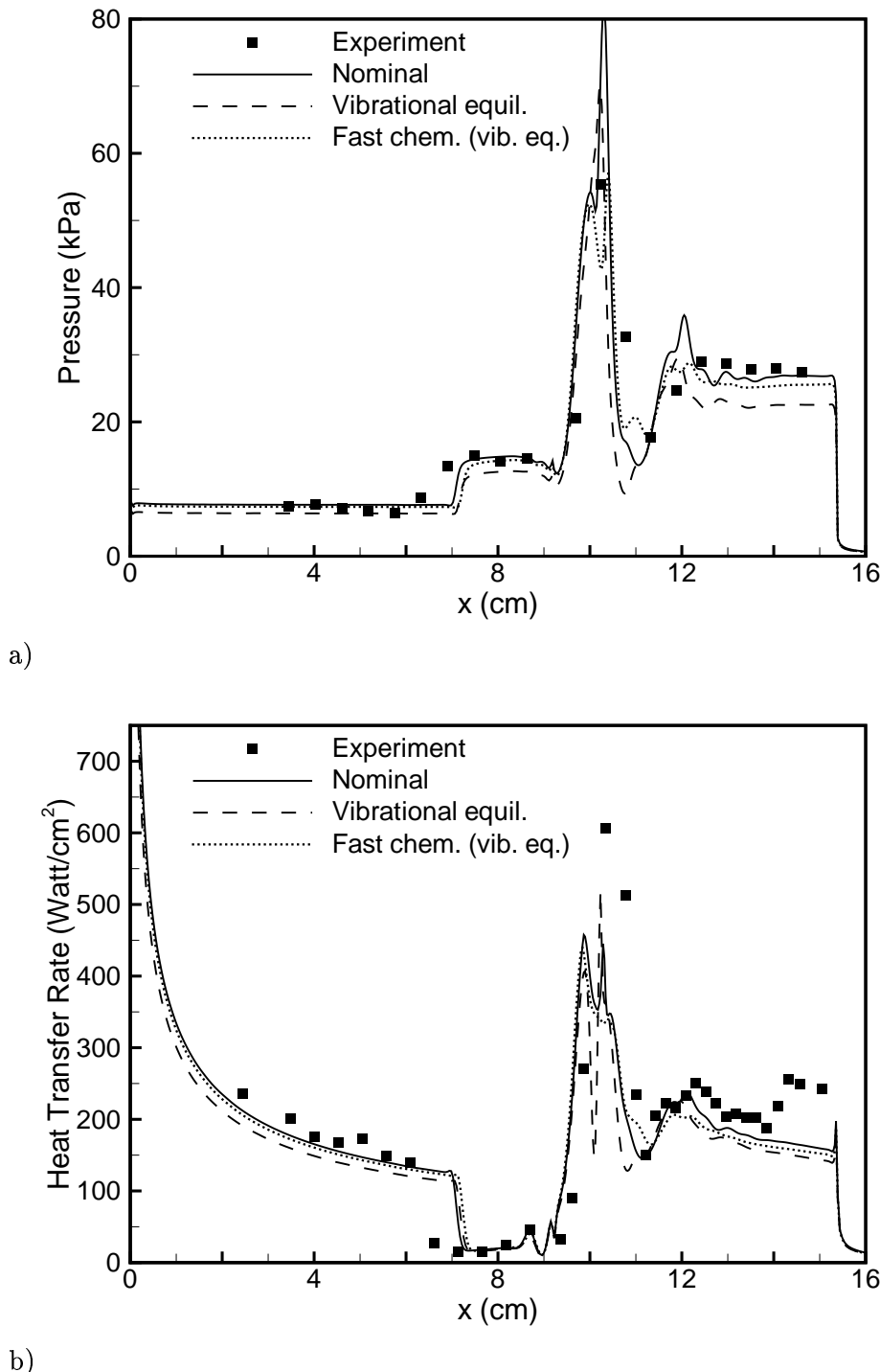


Fig. 7.11 Predicted surface pressure (a) and heat transfer rate (b) for Run 43 computed test-section conditions.

7.6 Conclusions

We performed detailed numerical simulations of high enthalpy nitrogen and air experiments from the LENS facility. These experiments were performed guided by the results of numerical simulation and evaluation of previous high enthalpy experiments. Also, the nominal experimental free-stream conditions provided by the experimentalists included the effect of vibrational nonequilibrium. After the experiments were completed, we re-evaluated the free-stream conditions by performing numerical simulations of the nozzle flow under the exact reservoir conditions of the experiments. We employed the Spalart-Allmaras turbulence model for all simulations of the nozzle flow. We were able to verify our implementation of the turbulence model by making comparisons with the heat transfer measurements to the nozzle wall during the calibration runs in both air and nitrogen. Numerical results were in good agreement with the Pitot pressure measurements at the nozzle exit-plane for the calibration runs. With this turbulence model, we did not have to adjust the simulation in order to match the Pitot pressure profile at the exit-plane. Therefore, the methodology that we developed based on the low enthalpy experiments of chapter 6 for free-stream characterization can be used for experiments at high enthalpy.

We simulated flows over the double-cone model at high enthalpy conditions. We compared numerical predictions under nominal and computed test-section conditions with the experimental data. The simulations are in agreement with the measurements for the pure nitrogen cases, however the peak in heat transfer rate and the width of the peak are significantly under-predicted at higher Reynolds numbers. This is indicative of inaccurate modeling, either in the determination of the free-stream conditions, or the chemistry models employed in the simulations. We did not obtain as good agreement for the air case. We performed simulations where we increased the rate of reaction both in the nozzle flow and in the flow over the model. In this way, we were able to reproduce the Pitot pressure profile in the test-

section when vibrational equilibrium was enforced in the simulation. Interestingly, simulations under the corresponding test-section conditions produced results very similar to those of the baseline simulation. We were unable to improve agreement with measurements for these high enthalpy experiments.

Chapter 8

Design of Experiments in the Expansion Tunnel

8.1 Introduction

In the previous chapter we presented simulations of high enthalpy air and nitrogen experiments performed using the LENS Leg I tunnel. These experiments were performed at low pressures, such that the resulting flow-fields were laminar and steady. The results showed good overall agreement for nitrogen flows, but significant differences between measurements and predictions were observed for air flows. This is not a surprising result. The pressures at which the experiments were performed were very low, in order to ensure that the flow over the model is laminar. At such low pressures, the free-stream generated by the reflected shock tunnel is in vibrational nonequilibrium and is weakly dissociated. Therefore, some degree of uncertainty is introduced because of this effect. Therefore, an alternative method of generating high Mach number free-streams at low pressure has been considered, and this involves using an expansion tunnel instead of a reflected shock tunnel.

A new hypervelocity tunnel has been developed at the LENS facility, which utilizes an expansion tube to generate high Mach number free-streams, and is designated as LENS-X. In this chapter, we present a preliminary study of a high enthalpy experiment performed using the LENS-X expansion tunnel. Computational fluid dynamics is used to simulate the entire experiment. This includes simulations of the flow inside the expansion tube and nozzle after the primary diaphragm breaks, and also the flow over the double-cone model. First, we provide a short description of the facility, and discuss results of the one-dimensional analysis performed for two cases. We proceed by presenting axisymmetric simulations of the flow inside the ex-

pansion tunnel assuming laminar and fully turbulent flow for one of the conditions. We obtain free-stream conditions by performing simulations of the nozzle flow, and finally, we simulate the flow over the model using these conditions.

8.2 Expansion Tube Experiments

Previous high enthalpy experiments at the LENS facility were performed using the LENS Leg I tunnel, operated in reflected shock mode. In these experiments, the test gas in the reservoir region behind the diaphragm is shock heated twice and stagnates before it accelerates into the nozzle. This allows the gas to reach its equilibrium composition at the stagnation temperature in the reservoir region. As the flow accelerates through the throat and into the nozzle, the gas cools rapidly during the expansion before it reaches the test-section. Depending on the flow conditions, this process may result in a partially dissociated or nonequilibrium free-stream. This is likely to be the case for the low pressure experiments of interest. Therefore, an alternative method of obtaining realistic high enthalpy free-streams using the existing experimental facilities was devised by making some modifications to the LENS facility. A section was added to the LENS Leg II tunnel, which allows it to be operated as an expansion tunnel. The details can be found in Holden (2004). The added section makes a transition from the expansion tube to the existing divergent nozzle. This type of arrangement forces the gas to undergo a steady expansion inside the divergent nozzle, following the unsteady expansion it experiences in the expansion tube [Lukasiewicz (1973)].

The expansion tube is a device by which high enthalpy cold flows can be obtained experimentally. The device consists of a long tube, separated by a primary and a secondary diaphragm as shown in Fig. (8.1). The three compartments contain the driver and driven gas at different temperatures and pressures. The driver gas is at high pressure and temperature, and is in the unperturbed region 1 as indicated on the $x - t$ diagram of Fig. (8.1). The driven gas occupies two compartments, the second of which is at a substantially lower pressure than the

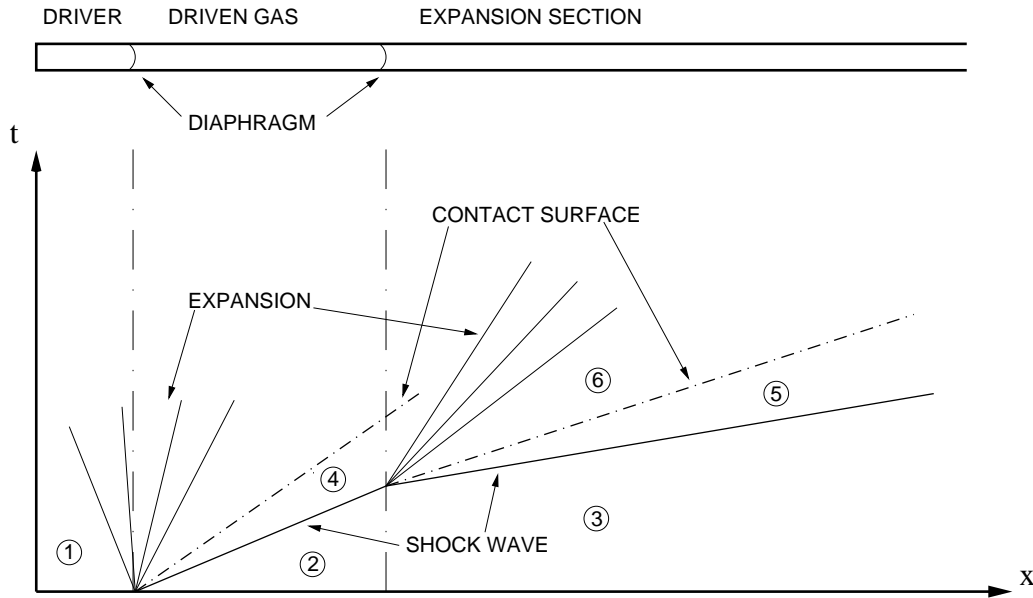


Fig. 8.1 Schematic of an expansion tube and its $x - t$ diagram.

first; these are regions 2 and 3 in Fig. (8.1). When the primary diaphragm breaks at the desired pressure, the driver gas accelerates into the second compartment, compressing the driven gas, and sending a shock wave traveling down the tube, as seen in the figure. Region 4 is a region of uniform state behind the primary shock, and is the test gas. When the primary shock breaks the second diaphragm, it sends a fast-moving shock down the expansion region. The total enthalpy is conserved and thus the gas behind the shock in region 5 is at very high temperature. The gas in region 6 has been accelerated to high velocity, but is at a relatively low temperature. Therefore, if air is placed in region 2 as the test gas, it can be set into motion at high enthalpy and maintained at a non-reacted state (region 6) using this experimental setup.

The expansion tunnel facility LENS-X consists of a nearly 48 m long, 0.6 m (24 in) diameter tube with a nozzle attached to it. Experiments have been performed in the LENS-X facility for two initial conditions. The driver gas for these experiments was helium and the test gas was air. The three compartments were

filled according to the conditions tabulated in Table (8.1). In the experiments, the primary diaphragm is actively broken, and the primary shock heats the test gas in the 583 inch long driven section. The second diaphragm breaks when the shock strikes it, and the test gas is accelerated behind the contact surface that is trailing the newly formed shock wave.

Compartment	Case A		Case B	
	$T(^{\circ}\text{R})$	p (psi)	$T(^{\circ}\text{R})$	p (psi)
Driver gas	770.0	1200	630.0	2000
Driven gas	529.3	3.000	527.9	1.470
Expansion section	529.3	0.0480	527.9	0.0059

Table. 8.1 Initial experimental conditions for LENS-X.

In the following sections we present results from a one-dimensional simulation of this process for both experimental conditions. We use computational fluid dynamics to perform this analysis, assuming an inviscid flow with finite rate chemical reactions and vibrational relaxation. The conditions of case B result in vibrational nonequilibrium inside the expansion tube. This is not the case for conditions A, where the test gas is in equilibrium. Subsequently, we perform two-dimensional laminar and turbulent simulations of the flow in the expansion tube for case A. From these simulations we extract free-stream conditions for the flow over the model.

8.3 Computational Procedure

Simulations of the expansion tube are performed using the numerical method presented in chapter 3. We solve the conservation equations for a six-species helium-air mixture. An additional equation is solved along with the conservation equations for the unsteady RANS simulations of the expansion tube and the nozzle flows. The Spalart-Allmaras one-equation turbulence model is employed in its original form, and the equation is solved in conservation law form. The MUSCL scheme for variable extrapolation with a minmod limiter is also used selectively in this work. We state explicitly where this scheme is employed.

8.4 One-Dimensional Analysis

In this section we present results from the one-dimensional simulation of the flow inside the expansion tube. We show that this type of analysis is very useful for assessing the state and composition of the test gas during the experiment. For these simulations, a first-order accurate stencil was used on a 10,000 point mesh representing the 48 m long tube.

Consider the experimental setup based on the initial conditions of case A mentioned previously. The primary diaphragm breaks and we allow the flow to evolve by integrating the equations in a time-accurate manner. This process is illustrated in Fig. (8.2), which plots the velocity and temperatures on the left vertical axis, and the mass-fractions of the species on the right axis, versus axial length measured from the primary diaphragm. The gas behind the primary shock is heated and is set in motion. This is seen in Fig. (8.2a) as the sharp increase in translational-rotational temperature and velocity. When the shock ruptures the second diaphragm, a fast-moving shock forms in the expansion region, and the test gas goes through a rapid expansion. The temperature behind the shock wave reaches levels at which chemical reactions take place. This is indicated by the increase in the mass-fractions of N, O, and NO and the corresponding decrease in N₂ and O₂ (Fig. (8.2b)). The effect of numerical dissipation is visible by the contact surfaces, which are no longer sharp. This is not critical for the purpose of this analysis. There are two interesting things to note for this simulation. First, the small region of moving test gas behind the shock is at a uniform state – this is region 6 in Fig. (8.1). Secondly, for this particular initial condition, the test gas is in its initial composition and in equilibrium before it enters the nozzle. The hot, partially reacted gases behind the shock will enter the nozzle and pass over the model geometry. Therefore, it is critical for the measurements over the model surface to be taken when the test gas is flowing over the geometry.

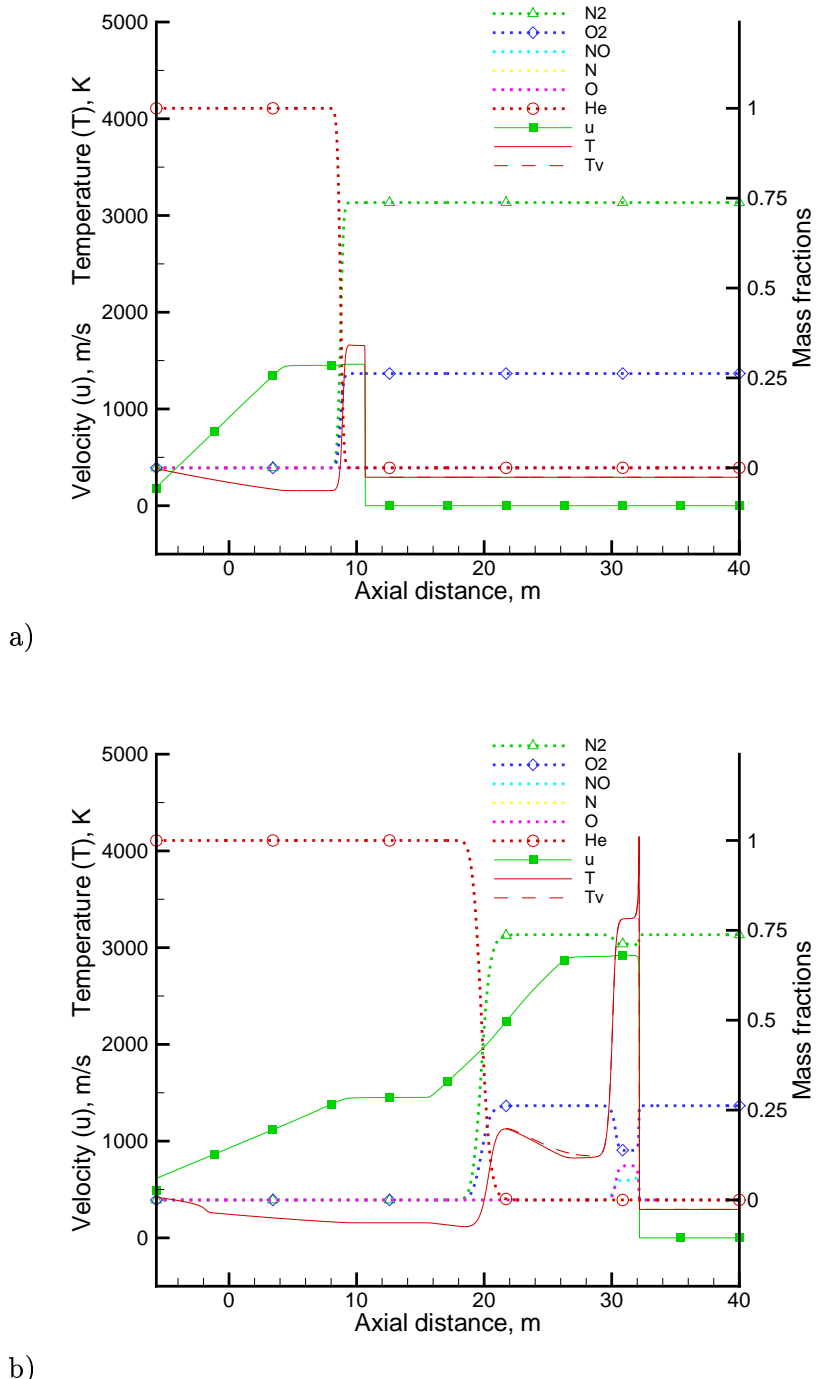


Fig. 8.2 Evolution of the 1-D flow in the expansion tube after rupture of (a) the primary diaphragm and (b) the secondary diaphragm for case A.

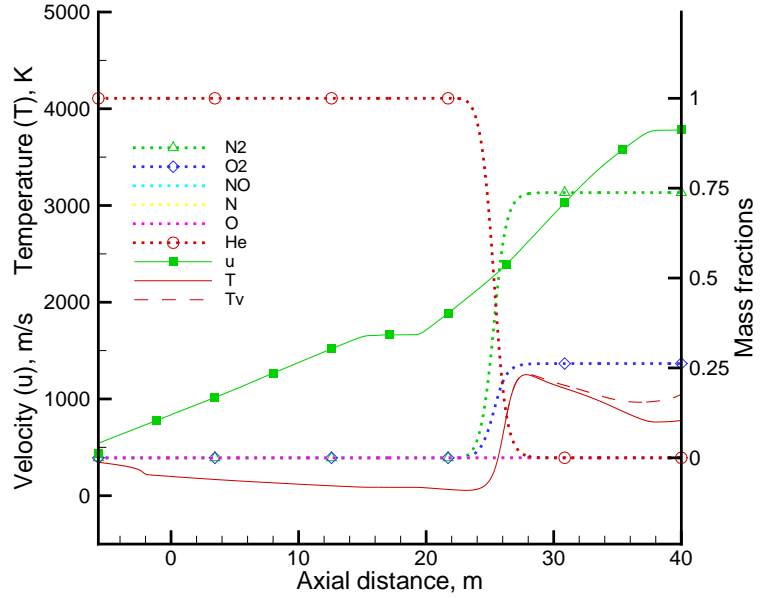


Fig. 8.3 Snapshot of the 1-D flow in the expansion tube for case B.

We performed the same analysis for case B. The simulation proceeds in the same manner, and the flow is very similar to that of case A. The test gas experiences an expansion behind the fast-moving shock, while the air in the expansion section dissociates in the high temperature region. Interestingly, the test gas is not in equilibrium as it leaves the expansion section and enters the nozzle (Fig. (8.3)). Based on this result, we did not investigate case B any further, and focused our work on case A.

8.5 Two-dimensional Simulations

From the one-dimensional analysis we were able to calculate the approximate time-varying state of the gas as it enters the nozzle. However, it is possible that the flow exhibits strong two-dimensionality, both in the expansion tube and in the nozzle itself. Thus, a more detailed two-dimensional simulation was required in order to have an accurate time-varying input specification for the nozzle flow. We carefully constructed a 8000×160 point mesh to represent the entire tube, with very

close stretching near the wall. After having performed preliminary axisymmetric simulations on coarser meshes, we concluded that this size mesh would produce reasonably accurate results without making the simulations extremely expensive. In this section, we show that the flow inside the tube is most likely turbulent, and that with a laminar simulation we are unable to get realistic results.

We performed simulations assuming a laminar axisymmetric flow inside the tube. For this simulation, the higher-order reconstruction for the evaluation of the inviscid fluxes was based on the MUSCL variable extrapolation scheme, and the minmod limiter was used. We used this type of reconstruction because with this method, extrapolation is performed individually for each of the conserved variables. This is appropriate for the unsteady turbulent simulations, where the turbulent viscosity may exhibit gradients in regions where other flow quantities are uniform and vice versa. Thus, the formulation is consistent between laminar and turbulent simulations. The flow behind the primary shock is mainly uniform, but exhibits small oscillations and vortical structures near the wall. The presence of these oscillations is probably the cause of the weak two-dimensionality that we observed in these flows.

The Reynolds number near the wall region of the flow behind the primary diaphragm is in the order of a few million per meter. Thus, the boundary layer that forms near the wall is likely to be turbulent. Therefore, we performed an unsteady RANS simulation of the nozzle flow assuming that the flow is fully turbulent. The turbulent simulation predicts a relatively uniform flow profile in the radial direction, throughout the entire length of the tube. Small oscillations were observed shortly after the primary diaphragm rupture, but they did not persist after the second diaphragm was ruptured.

Fig. (8.4) shows contours of translational temperature for the laminar and turbulent simulations, just before the primary shock enters the nozzle. The test gas is traveling to the right, and is situated to the left of the hot gas. We can see that

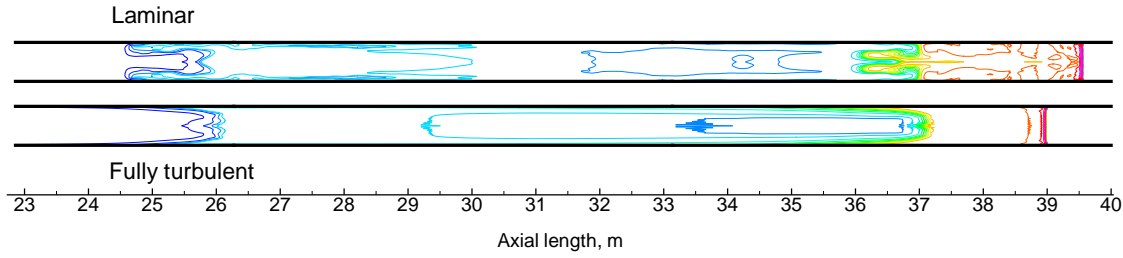


Fig. 8.4 Snapshot of the laminar (top) and fully turbulent (bottom) flows inside the expansion tube – temperature contours are shown.

there is some two-dimensionality in the laminar simulation, while the turbulent simulation resembles “plug flow.” Fig. (8.5) plots flow variables at the centerline of the tube for the snapshots shown in Fig. (8.4). At the centerline the flows are very similar, with the exception of the presence of small oscillations in the laminar simulation. In the turbulent simulation, there is a region of the flow behind the primary shock, where the gas is at a uniform state. This is not the case for the laminar simulation, where the variation of the temperature and velocity in that region are significant. This is attributed to the presence of small disturbances near the advancing front during the evolution of the flow in the tube. In view of these results, we concluded that a laminar simulation gives substantially different results than the more realistic turbulent one. Thus, it is not possible to obtain a realistic time-varying input specification for the nozzle flow using a laminar simulation of the expansion tube.

8.6 Nozzle Flow Simulations

In this section we present results from the simulation of the nozzle flow. The flow inside the nozzle is assumed to be fully turbulent, and is computed in a way similar to the flow inside the expansion tube. We extended the computational domain ahead of the primary shock shown in Fig. (8.4), by attaching a 2000×160 point mesh representing the nozzle geometry. In this way, we were able to simply continue the evolution of the flow, and thus we effectively provided a time dependent input specification to the nozzle flow. This simulation was performed using the MUSCL scheme.

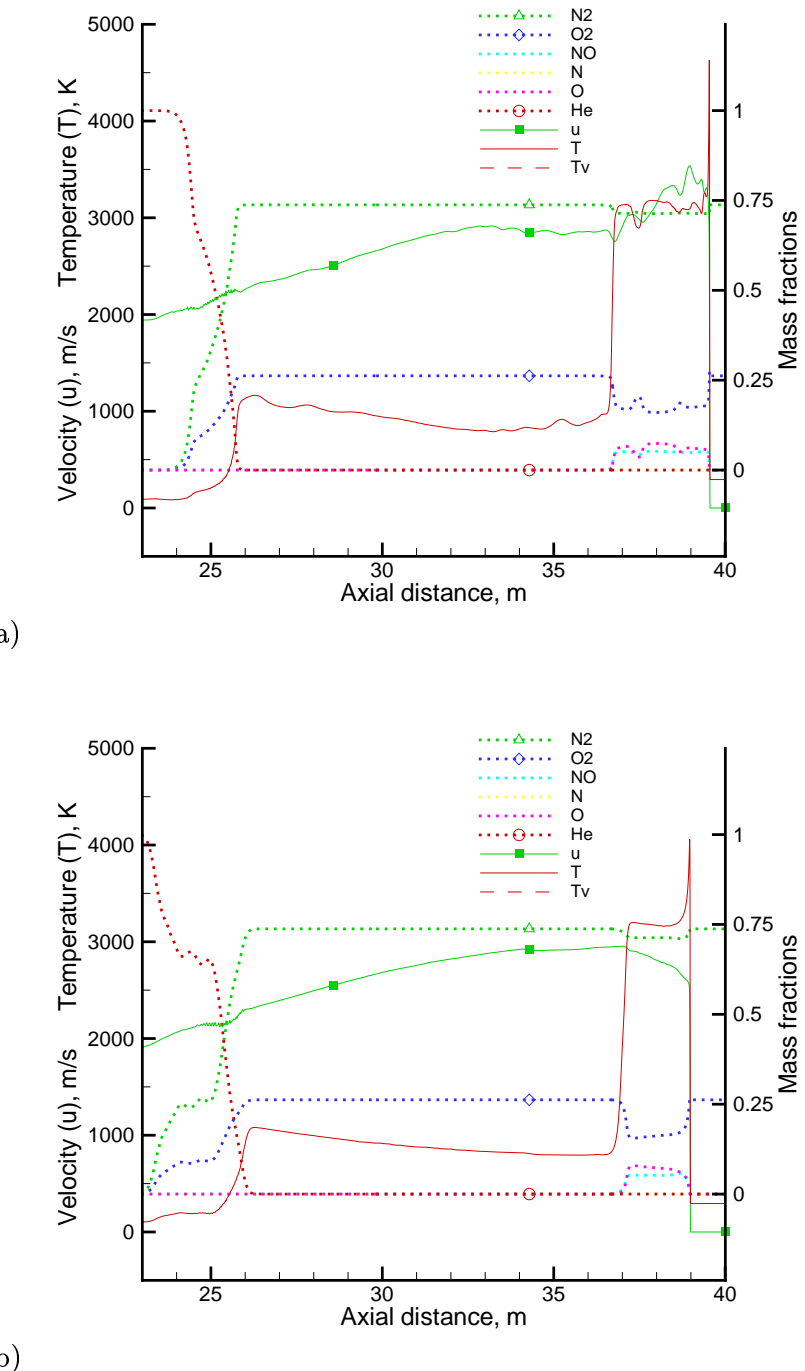


Fig. 8.5 State variables and species mass-fractions at the centerline of the tube for laminar (left) and fully turbulent (right) flow snapshots of Fig. (8.4).

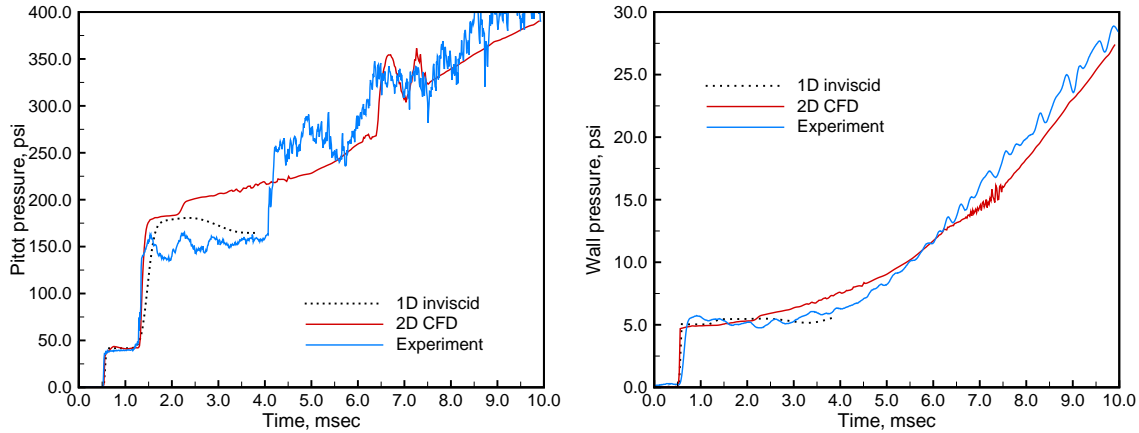


Fig. 8.6 Computed and measured time history of the Pitot pressure (left) and computed wall pressure (right) near the exit of the expansion section.

In this simulation, we allowed the flow to evolve until the driver gas reached the test-section. During the experiments, measurements are made of the Pitot pressure and wall pressure at the exit of the expansion tube. These measurements can be compared directly with the computed Pitot and static pressures, which are shown in Fig. (8.6). The Pitot and wall pressures are plotted versus the time measured from when the primary shock reaches the nozzle section. We see the sharp increase in Pitot pressure when the primary shock passes, followed by another increase when the test gas arrives (Fig. (8.6a)). We also see the increase in the wall pressure when the test gas passes (Fig. (8.6b)).

The test gas expands to a high Mach number at the centerline just upstream of the exit-plane. Then, the gas recompresses to a Mach number of about 7 as it enters the test-section. We should emphasize that when the test gas enters the nozzle, it undergoes a steady expansion. This steady expansion is desired because it allows for a steady nozzle flow to be established. For this particular experimental condition, we predict the flow inside the nozzle to remain steady for an excess of 3 msec.

Fig. (8.7) plots the Pitot pressure at the exit-plane of the nozzle versus the time from when the primary shock enters the nozzle. The primary shock takes approxi-

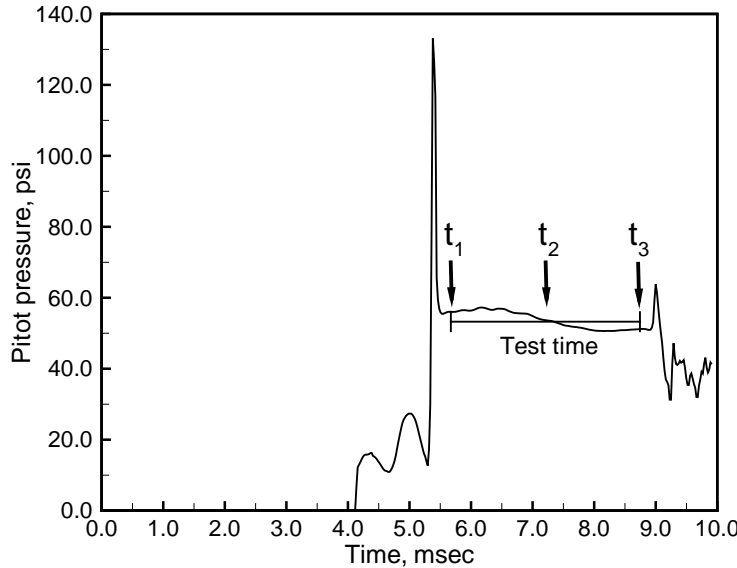


Fig. 8.7 Computed time history of the Pitot pressure at the nozzle exit-plane.

mately 4 msec to reach the exit-plane of the nozzle. The oscillations that follow are due to the structure of the advancing front that consists of the hot gas. When the test gas reaches the exit-plane, the Pitot pressure at the centerline remains constant at about 55 psi, as indicated by the plateau in Fig. (8.7). A direct estimate of the conditional test time can be made from this plateau, which measures approximately 3 msec. Note that this Pitot measurement is at the centerline. Therefore an assessment must be made of the uniformity of the flow in the test-section by examining the radial distribution of flow quantities. Furthermore, the distribution of flow quantities in the radial direction must be examined over the duration of the useful test time. We do this by extracting flow profiles in the radial direction for three instances marked by the arrows on Fig. (8.7), and indicated by $t_1 = 5.7$ msec, $t_2 = 7.2$ msec, and $t_3 = 8.7$ msec. The radial distributions of axial velocity, Pitot pressure, and Mach number are plotted in Fig. (8.8). The profiles show that the flow is relatively uniform inside a circular region of about 0.5 m (20 in) in diameter. This is because of the large size of the facility. Also, we see that the time-varying profiles start by exhibiting substantial non-uniformity immediately following the

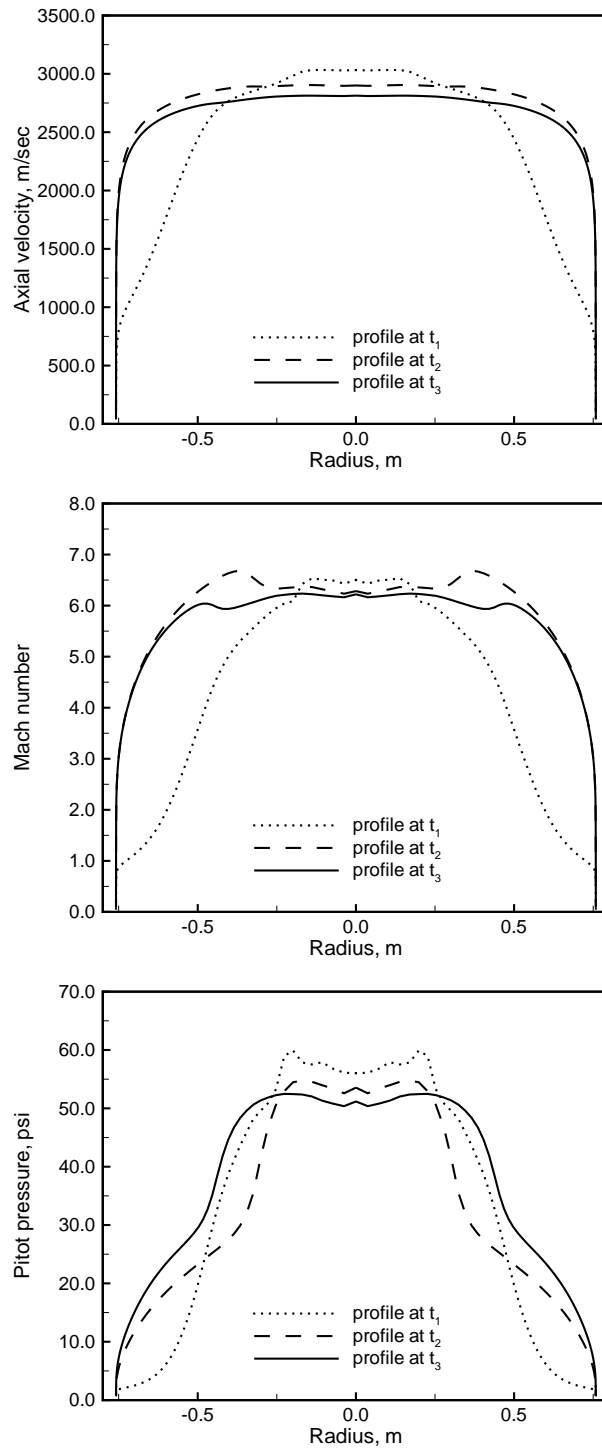


Fig. 8.8 Computed axial velocity (top), Mach number (middle), and Pitot pressure (bottom) at the nozzle exit-plane.

arrival of the test gas. This is because of the structure of the advancing front.

With this study of the flow we were able to get an estimate of the test time that can be achieved using this setup, and also calculate the state of the gas at the test-section. The computed free-stream conditions are tabulated in Table (8.2).

Case A	Computed (air)	Nominal (air)
M_∞	6.34	7.39
T_∞ (K)	548.2	565.3
$T_{v\infty}$ (K)	851.4	565.3
ρ_∞ (g/m ³)	47.77	15.25
u_∞ (m/s)	2974.7	3521.7

Table. 8.2 Computed free-stream conditions at the exit-plane of the nozzle for case A.

8.7 Double-Cone Flow

We simulated the flow over the 25°-55° double-cone model with free-stream conditions as given in Table (8.2). We used a mesh of 512 × 256 points in the streamwise and wall-normal directions. The numerical method employed was the same as what we used to simulate the low and high enthalpy double-cone flows of chapters 4 and 7. This particular numerical method along with a mesh of this size is expected to give results accurate to about 1% in terms of the size of the separation zone. The computed flowfield exhibited a very large region of separation. The existence of such a large region of separated flow is an indication that this flow might be transitional. This is probably because the free-stream density is an order of magnitude larger than that of the earlier LENS Leg I double-cone experiments.

8.8 Conclusions

Detailed simulations of hypersonic high enthalpy experiments in the LENS expansion tube were performed. We focused on one of the two experimental conditions provided. We compared our simulation results with measurements made during the experiment, in particular, Pitot pressure and wall pressure at the exit of the expansion tube. The comparisons showed that the CFD predicts correctly the arrival

of the test gas in the nozzle behind the primary shock. We were unable to obtain complete quantitative agreement between the measurements and simulation results for this experiment. The pressure near the wall at the end of the expansion section was in good agreement, but the Pitot pressure along the centerline of the tube at that location was not matched. This discrepancy is probably a result of numerical dissipation and insufficient grid resolution.

We obtained an estimate of the available test time during the experiment using this approach. Under the present conditions, the available test time is about 3 msec. We computed conditions at the exit-plane, and these can be used as free-stream conditions for the double-cone flow. Also, the free-stream resulted from this experiment is non-reacted and exhibits only a small degree of vibrational nonequilibrium. The simulation showed that the flow is uniform in a relatively large region at the center of the nozzle when it enters the test-section. This region is large enough to ensure that there is uniform flow around the entire double-cone model. However, under the present conditions, we expect that the double-cone flowfield will likely be transitional. Finally, we have demonstrated that it is possible to simulate the entire experiment in this large facility with reasonable accuracy. This process will help design new expansion tube experiments with realistic free-streams.

Chapter 9

Summary and Conclusions

9.1 Summary

This thesis discusses numerical simulations of experiments of hypersonic flows over double-cone geometries performed at the Large Energy National Shock (LENS) facility. This work was motivated by earlier computational studies of double-cone and double-wedge experiments, which showed primarily that flows with strong shock interactions may serve as test cases for the validation of nonequilibrium chemistry models. The double-cone flow was chosen because it exhibits circular symmetry, thus only two-dimensional simulations are required, which substantially decreases the cost of such simulations.

First, the governing equations for the relevant flow physics were presented, along with the physical models that provide closure, namely the transport coefficients, the chemical reaction rate coefficients, the equilibrium constants, and the vibration-dissociation coupling model. Also, the discretization of the governing equations and the numerical method of solution were discussed in detail.

In the first stage of this work, simulations of double-cone flow experiments at low enthalpy conditions were performed, with the purpose to assess the ability of the numerical method to reproduce the basic flows. These experiments were performed at low pressures, such that the flow over the model was laminar. There was no prior knowledge of the experimental measurements when these simulations were performed. The *blind* comparisons showed good agreement between the numerical predictions and the experimental surface measurements, with the exception of the heat transfer rate at the first cone.

In order to better understand the limitations of the numerical method and to assess its accuracy, the double-cone flow was simulated using different flux evaluation methods of varying degree of sophistication. In this study, the effect of numerical dissipation exhibited by different flux evaluation schemes was examined. Additionally, grid convergence studies were presented. As a result of these studies, we established a measure for the numerical dissipation and the rate of grid convergence of a given numerical scheme, based on the computed size of the separation zone that is resulted by employing this scheme.

Next, the reason for the discrepancies observed in simulations of low enthalpy flows was investigated by performing detailed simulations of the experiments and the wind tunnel flow. We used CFD to simulate the flow in the nozzle of the LENS tunnel. By matching Pitot pressure measurements of survey instruments, we attempted to compute the free-stream conditions at the exit-plane of the nozzle. We found that there is some degree of nonequilibrium in the free-stream due to the low density at which the experiments were performed. This, along with weak vibrational energy accommodation at the surface is responsible for the discrepancies. From this approach, a methodology was developed for designing and characterizing the LENS experiments. Following this study, new high enthalpy experiments were performed. We applied this methodology to the new high enthalpy double-cone flows of nitrogen and air. We observed good agreement for nitrogen flows, but we were unable to reproduce the measurements for air flows.

Finally, an alternative method for producing high enthalpy non-reacted free-streams was presented. This makes use of the newly developed expansion tunnel facility at LENS. With this study, we showed that useful test times of up to 3 msec can be obtained, and the free-stream exhibits only a small degree of vibrational nonequilibrium, but maintains its original composition.

9.2 Conclusions

This work showed that computational fluid dynamics is capable of accurately

reproducing hypersonic flows with shock/shock and shock wave/boundary layer interactions. However, large computational meshes may be required, and it is important to perform a careful grid convergence study. Also, for these flows with large regions of separation, the amount of physical time that must be simulated may exceed several flow times. Thus, obtaining accurate results on a fine mesh requires the use of an implicit solver.

The double-cone flow is an excellent case for validating computational fluid dynamics codes. This is in part because the embedded region of separation is sensitive to high enthalpy effects, and its size can be measured accurately during the experiment from the surface measurements. The LENS experiments use densely instrumented models, and allow for an accurate measurement of the separation zone size to be made. Thus, provided that a CFD code accurately predicts the flow under conditions where chemical reactions are not taking place, air chemistry models can be tested at higher enthalpy conditions.

Also, double-cone flow predictions are sensitive to the quality of the numerical method employed. In particular, the predicted size of the separation zone on a given computational mesh, is directly related to the amount of numerical dissipation in the scheme. In general, less dissipative numerical schemes predict a larger separation zone than the more dissipative ones. Additionally, dissipative numerical methods may require many more points to produce grid resolved results. Therefore, we can quantify the amount of numerical dissipation in a given scheme by the separation zone size that is predicted using the scheme.

In validation studies, it is crucial to have the correct free-stream specification and boundary conditions, but also adequate modeling of the flow physics. For the low density flows of interest, it is important to model the gas surface interaction correctly, and account for non-continuum effects. In doing this, partial accommodation to the wall of the internal energy modes of the gas must be considered.

Because the separation zone size depends on the grid resolution and the quality

of the numerics, it is possible to obtain spurious “agreement” with experiments due to poor grid resolution. Therefore, the double-cone simulations illustrate the importance of conducting careful grid convergence studies. Also, for the same reason, we see the value in making blind comparisons with experiments.

9.3 Recommendations for Future Research

The development of double-cone experiments at high enthalpy remains a difficult task. The process of specifying the experimental conditions remains a source of uncertainty, particularly for air flows. This is because the chemical reaction rates are not accurate for the sudden expansion of high temperature air that is partially dissociated and in nonequilibrium. Thus, we do not have complete knowledge of the state of the gas in the hypersonic nozzle and at the exit-plane. However, using CFD to understand the nozzle flows has provided an advantage over traditional methods, and more work needs to be done in that area. This process must be aided by experimental measurements made in the nozzle.

Using the expansion tube for generating hypersonic free-streams at high enthalpy can aid the validation process. First, experiments must be designed to produce low density, low enthalpy free-streams, resulting in essentially perfect gas laminar flows. In this way, comparisons across facilities can be made. Upon successful completion of this process, high enthalpy experiments should be designed and characterized with CFD.

Finally, independent work on high temperature nonequilibrium air chemistry models should be done. This is an area of research where work in other disciplines, such as computational chemistry, must be done.

Appendix A

Model Constants

Species	θ_{vs} (K)
N ₂	3395
O ₂	2239
NO	2817

Table A.1 Characteristic harmonic oscillator vibrational temperatures.

Species	h_s° (J/kg)
N ₂	0.0
O ₂	0.0
NO	$2.996123 \cdot 10^6$
N	$3.362161 \cdot 10^7$
O	$1.543119 \cdot 10^7$

Table A.2 Formation enthalpies for each species.

Species	A_s	B_s	C_s
N ₂	0.0268142	0.3177838	-11.3155513
O ₂	0.0449290	-0.0826158	-9.2019475
NO	0.0436378	-0.0335511	-9.5767430
N	0.0115572	0.6031679	-12.4327495
O	0.0203144	0.4294404	-12.6031403

Table A.3 Viscosity coefficients for the Blottner model.

Reaction	C_{f_m} (m ³ /kg s)			η_m	θ_m (K)
	(for collision partner)				
	N ₂ ,O ₂	NO	N,O		
1	$7.00 \cdot 10^{18}$	$7.00 \cdot 10^{18}$	$3.00 \cdot 10^{19}$	-1.60	113200
2	$2.00 \cdot 10^{18}$	$2.00 \cdot 10^{18}$	$1.00 \cdot 10^{19}$	-1.50	59500
3	$5.00 \cdot 10^{12}$	$1.10 \cdot 10^{14}$	$1.10 \cdot 10^{14}$	0.00	75500
4			$6.40 \cdot 10^{14}$	-1.00	38400
5			$8.40 \cdot 10^9$	0.00	19400

Table A.4 Arrhenius coefficients for forward reaction rates.

Reaction	C_m	A_{1m}	A_{2m}	A_{3m}	A_{4m}	A_{5m}
1	1000	1.606000	1.573200	1.39230	-11.5530	-0.004543
2	1000	0.641830	2.425300	1.90260	-6.62770	0.035151
3	1000	0.638170	0.681890	0.66336	-7.57730	-0.011025
4	0	0.967940	0.891310	0.72910	-3.95550	0.006488
5	0	-0.003732	-1.743400	-1.23940	-0.94952	-0.046182

Table A.5 Constants for computing K_{eq_m} .

Appendix B

The Axisymmetric Finite Volume Formulation

In this section we derive the axisymmetric formulation of the finite volume method. The specific case of a perfect gas is presented here, and thus a single mass conservation equation, two momentum equations, and one energy equation are considered. The resulted form of the equations can be extended to more complicated sets of equations in a straightforward manner. The axisymmetric formulation is presented for the weak form of the Euler and Navier-Stokes equations within a fixed volume in physical space.

We consider a cylindrical system of coordinates (r, θ, x) with the axial direction x aligned with the x -axis in the Cartesian system of coordinates, and the plane $\theta=0$ be the x - y plane. The local velocity vector in the cylindrical coordinate system $\vec{v}(\vec{r}) = v_r \hat{e}_r + v_\theta \hat{e}_\theta + v_x \hat{e}_x$ can be expressed in terms of its components in the Cartesian coordinate system as:

$$\begin{pmatrix} u_1 \\ u_2 \\ u_3 \end{pmatrix} = \begin{pmatrix} 0 & 0 & 1 \\ \cos \theta & -\sin \theta & 0 \\ \sin \theta & \cos \theta & 0 \end{pmatrix} \begin{pmatrix} v_r \\ v_\theta \\ v_x \end{pmatrix} \quad (B.1)$$

for the local angle θ . We can express the conserved variables U and the components of the corresponding inviscid flux $\vec{F} = F_1 \hat{i} + F_2 \hat{j} + F_3 \hat{k}$ in Cartesian coordinates using the transformation of (B.1) as:

$$U = \begin{pmatrix} \rho \\ \rho v_x \\ \rho(v_r \cos \theta - v_\theta \sin \theta) \\ \rho(v_r \sin \theta + v_\theta \cos \theta) \\ E \end{pmatrix}, \quad F_1 = \begin{pmatrix} \rho v_x \\ \rho v_x v_x + p \\ \rho(v_r \cos \theta - v_\theta \sin \theta) v_x \\ \rho(v_r \sin \theta + v_\theta \cos \theta) v_x \\ (E + p) v_x \end{pmatrix},$$

$$F_2 = \begin{pmatrix} \rho(v_r \cos \theta - v_\theta \sin \theta) \\ \rho v_x(v_r \cos \theta - v_\theta \sin \theta) \\ \rho(v_r \cos \theta - v_\theta \sin \theta)^2 + p \\ \rho(v_r \sin \theta + v_\theta \cos \theta)(v_r \cos \theta - v_\theta \sin \theta) \\ (E + p)(v_r \cos \theta - v_\theta \sin \theta) \end{pmatrix},$$

$$F_3 = \begin{pmatrix} \rho(v_r \sin \theta + v_\theta \cos \theta) \\ \rho v_x(v_r \sin \theta + v_\theta \cos \theta) \\ \rho(v_r \cos \theta - v_\theta \sin \theta)(v_r \sin \theta + v_\theta \cos \theta) \\ \rho(v_r \sin \theta + v_\theta \cos \theta)^2 + p \\ (E + p)(v_r \sin \theta + v_\theta \cos \theta) \end{pmatrix}$$

Let C be a fixed area on the r - x plane, sweeping a volume Ω by a $2\theta_o$ rotation about the x -axis, and symmetric about $\theta=0$. The weak form of the Euler equations on the axisymmetric domain Ω is:

$$\int_{\Omega} \frac{\partial U}{\partial t} dV + \int_{\partial\Omega} \vec{F} \cdot \hat{n} dS = 0. \quad (B.2)$$

If the area C is an quadrilateral cell made of four infinitesimal line segments, the surface of the axisymmetric domain is $\partial\Omega = A_{x_1+} \cup A_{x_1-} \cup A_{x_2+} \cup A_{x_2-} \cup A_{x_3+} \cup A_{x_3-}$. Then the surface integral can be calculated over the six faces of the volume, and we may rewrite equation (B.2) as:

$$\frac{\partial \bar{U}}{\partial t} V + \int_{A_{x_1+} \cup A_{x_1-} \cup A_{x_2+} \cup A_{x_2-}} \vec{F} \cdot \hat{n} dS + \int_{A_{x_3+} \cup A_{x_3-}} \vec{F} \cdot \hat{n} dS = 0 \quad (B.3)$$

where $V = 2\theta_o r_c A$ is the total volume of Ω , A is the area of the cell C and r_c the radius of the centroid of the cell. The quantities U are averaged over Ω . We will compute the two integrals of eq. (B.3) separately. We approximate the first integral of eq. (B.3) as:

$$\int_{A_{x_1+} \cup A_{x_1-} \cup A_{x_2+} \cup A_{x_2-}} \vec{F} \cdot \hat{n} dS = 2\theta_o [H_{x_1+} l_{x_1+} r_{x_1+} + H_{x_1-} l_{x_1-} r_{x_1-} + H_{x_2+} l_{x_2+} r_{x_2+} + H_{x_2-} l_{x_2-} r_{x_2-}] \quad (B.4)$$

where $H_{x_1+}, H_{x_1-}, H_{x_2+}, H_{x_2-}$ are the numerical fluxes, l corresponds to the length of each line segment, and r is the distance from the center of each line segment to the symmetry axis. The second integral of eq. (B.3) involves the normal vectors on

the surfaces A_{x_3+}, A_{x_3-} and the corresponding flux vectors evaluated at angles $+\theta_o$ and $-\theta_o$ respectively. We write the integrands for each face as:

$$\begin{aligned}
 (\vec{F} \cdot \hat{n})|_{\theta=+\theta_o} &= \vec{F}|_{\theta=+\theta_o} \cdot (-\sin \theta_o \hat{j} + \cos \theta_o \hat{k}) \\
 &= -F_2|_{\theta=+\theta_o} \sin \theta_o + F_3|_{\theta=+\theta_o} \cos \theta_o \\
 &= \begin{pmatrix} \rho v_\theta \\ \rho v_x v_\theta \\ \rho(-v_\theta^2(\sin^3 \theta_o + \sin \theta_o \cos^2 \theta_o) + v_r v_\theta(\cos \theta_o \sin^2 \theta_o + \cos^3 \theta_o)) - p \sin \theta_o \\ \rho(v_\theta^2(\sin^2 \theta_o \cos \theta_o + \cos^3 \theta_o) + v_r v_\theta(\sin^3 \theta_o + \cos^2 \theta_o \sin \theta_o)) + p \cos \theta_o \\ (E + p)v_\theta \end{pmatrix}, \\
 (\vec{F} \cdot \hat{n})|_{\theta=-\theta_o} &= \vec{F}|_{\theta=-\theta_o} \cdot (-\sin \theta_o \hat{j} - \cos \theta_o \hat{k}) \\
 &= -F_2|_{\theta=-\theta_o} \sin \theta_o - F_3|_{\theta=-\theta_o} \cos \theta_o \\
 &= \begin{pmatrix} -\rho v_\theta \\ -\rho v_x v_\theta \\ \rho(-v_\theta^2(\sin^3 \theta_o + \cos^2 \theta_o \sin \theta_o) - v_r v_\theta(\cos \theta_o \sin^2 \theta_o + \cos^3 \theta_o)) - p \sin \theta_o \\ \rho(-v_\theta^2(\cos^3 \theta_o + \cos \theta_o \sin^2 \theta_o) + v_r v_\theta(\sin^3 \theta_o + \sin \theta_o \cos^2 \theta_o)) - p \cos \theta_o \\ -(E + p)v_\theta \end{pmatrix}.
 \end{aligned}$$

We compute the integral by summing the contributions from both faces:

$$\begin{aligned}
 \int_{A_{x_3+} \cup A_{x_3-}} \vec{F} \cdot \hat{n} dS &= [(\vec{F} \cdot \hat{n})|_{\theta=+\theta_o} + (\vec{F} \cdot \hat{n})|_{\theta=-\theta_o}] A \\
 &= \begin{pmatrix} 0 \\ 0 \\ \rho(-2v_\theta^2 \sin \theta_o) - 2p \sin \theta_o \\ \rho(2v_r v_\theta \sin \theta_o) \\ 0 \end{pmatrix} A. \tag{B.5}
 \end{aligned}$$

We rewrite eq. (B.3) using the expressions obtained for the two integrals of equations (B.4), (B.5) and divide by $2\theta_o$ to get:

$$\begin{aligned}
 \frac{\partial \bar{U}}{\partial t} r_c A + [H_{x_{1+}} l_{x_{1+}} r_{x_{1+}} + H_{x_{1-}} l_{x_{1-}} r_{x_{1-}} + H_{x_{2+}} l_{x_{2+}} r_{x_{2+}} + H_{x_{2-}} l_{x_{2-}} r_{x_{2-}}] + \\
 \begin{pmatrix} 0 \\ 0 \\ \rho(-v_\theta^2 \sin \theta_o) - p \sin \theta_o \\ \rho(v_r v_\theta \sin \theta_o) \\ 0 \end{pmatrix} \frac{A}{\theta_o} = 0. \tag{B.6}
 \end{aligned}$$

We take the limit of eq. (B.6) as θ_o shrinks to zero, and we write the final form of the equations as:

$$r_c A \frac{\partial}{\partial t} \begin{pmatrix} \rho \\ \rho v_x \\ \rho v_r \\ \rho v_\theta \\ E \end{pmatrix} + \sum_{i \in \{x_{1\pm}, x_{2\pm}\}} H_i l_i r_i + \begin{pmatrix} 0 \\ 0 \\ -\rho v_\theta^2 - p \\ \rho v_r v_\theta \\ 0 \end{pmatrix} A = 0 .$$

The extension of this axisymmetric formulation to the Navier-Stokes equations is straight forward. We integrate the divergence of the diffusive flux \vec{F}_v and we add it to the right hand side of eq. (B.2). This gives us the weak form of the Navier-Stokes equations:

$$\int_{\Omega} \frac{\partial U}{\partial t} dV + \int_{\partial\Omega} \vec{F} \cdot \hat{n} dS = \int_{\partial\Omega} \vec{F}_v \cdot \hat{n} dS . \quad (B.7)$$

We must evaluate the surface integrals in the Cartesian coordinate system as we did for the Euler equations. First we need to construct the diffusive fluxes in terms of the viscous stresses and the heat flux vector; this involves the velocities given by eq. (B.1) and their derivatives, and also the gradient of temperature. We need to know how derivatives between coordinates are related and so we consider the transformations:

$$\begin{aligned} x_1 &= x & r^2 &= x_2^2 + x_3^2 \\ x_2 &= r \cos \theta & \tan \theta &= \frac{x_3}{x_2} \\ x_3 &= r \sin \theta \end{aligned} \quad (B.8)$$

From these relationships we can construct operators for the derivatives of quantities with respect to Cartesian coordinates:

$$\begin{aligned} \frac{\partial}{\partial x_1} &= \frac{\partial}{\partial x} \\ \frac{\partial}{\partial x_2} &= \cos \theta \frac{\partial}{\partial r} - \frac{\sin \theta}{r} \frac{\partial}{\partial \theta} \\ \frac{\partial}{\partial x_3} &= \sin \theta \frac{\partial}{\partial r} + \frac{\cos \theta}{r} \frac{\partial}{\partial \theta} \end{aligned} \quad (B.9)$$

Using the expressions for velocity components given by eq. (B.1) and the above operators, we can write expressions for the Cartesian components of the viscous stress tensor $\tilde{\tau}$:

$$\begin{aligned}\tau_{11} &= 2\mu \frac{\partial}{\partial x} v_x + \lambda \vec{\nabla} \cdot \vec{v} \\ \tau_{12} = \tau_{21} &= \mu \left[(\cos \theta \frac{\partial}{\partial r} - \frac{\sin \theta}{r} \frac{\partial}{\partial \theta}) v_x + \frac{\partial}{\partial x} (\cos \theta v_r - \sin \theta v_\theta) \right] \\ \tau_{13} = \tau_{31} &= \mu \left[(\sin \theta \frac{\partial}{\partial r} + \frac{\cos \theta}{r} \frac{\partial}{\partial \theta}) v_x + \frac{\partial}{\partial x} (\sin \theta v_r + \cos \theta v_\theta) \right] \\ \tau_{22} &= 2\mu \left(\cos \theta \frac{\partial}{\partial r} - \frac{\sin \theta}{r} \frac{\partial}{\partial \theta} \right) (\cos \theta v_r - \sin \theta v_\theta) + \lambda \vec{\nabla} \cdot \vec{v} \\ \tau_{23} = \tau_{32} &= \mu \left[\left(\sin \theta \frac{\partial}{\partial r} + \frac{\cos \theta}{r} \frac{\partial}{\partial \theta} \right) (\cos \theta v_r - \sin \theta v_\theta) \right. \\ &\quad \left. + \left(\cos \theta \frac{\partial}{\partial r} - \frac{\sin \theta}{r} \frac{\partial}{\partial \theta} \right) (\sin \theta v_r + \cos \theta v_\theta) \right] \\ \tau_{33} &= 2\mu \left(\sin \theta \frac{\partial}{\partial r} + \frac{\cos \theta}{r} \frac{\partial}{\partial \theta} \right) (\sin \theta v_r + \cos \theta v_\theta) + \lambda \vec{\nabla} \cdot \vec{v}\end{aligned}\quad (B.10)$$

The heat flux vector \vec{q} is simply:

$$\vec{q} = -k \left[\frac{\partial T}{x} \hat{i} + \left(\cos \theta \frac{\partial}{\partial r} - \frac{\sin \theta}{r} \frac{\partial}{\partial \theta} \right) T \hat{j} + \left(\sin \theta \frac{\partial}{\partial r} + \frac{\cos \theta}{r} \frac{\partial}{\partial \theta} \right) T \hat{k} \right]. \quad (B.11)$$

We may now compute the surface integral of the diffusive fluxes in eq. (B.7) by splitting it into two parts. The contribution from the integral over the faces $A_{x_1+}, A_{x_1-}, A_{x_2+}, A_{x_2-}$ will consist of another set of numerical fluxes similar to those in eq. (B.4). We will evaluate the integral over faces A_{x_3+} and A_{x_3-} explicitly. The integrands for these faces are:

$$\begin{aligned}(\vec{F}_v \cdot \hat{n})|_{\theta=+\theta_o} &= \vec{F}_v|_{\theta=+\theta_o} \cdot (-\sin \theta_o \hat{j} + \cos \theta_o \hat{k}) \\ &= \begin{pmatrix} 0 \\ \tau_{21} \\ \tau_{22} \\ \tau_{23} \\ (\tilde{\tau} \cdot \vec{v})_2 + q_2 \end{pmatrix}_{\theta=+\theta_o} (-\sin \theta_o) + \begin{pmatrix} 0 \\ \tau_{31} \\ \tau_{32} \\ \tau_{33} \\ (\tilde{\tau} \cdot \vec{v})_3 + q_3 \end{pmatrix}_{\theta=+\theta_o} \cos \theta_o, \\ (\vec{F}_v \cdot \hat{n})|_{\theta=-\theta_o} &= \vec{F}_v|_{\theta=-\theta_o} \cdot (-\sin \theta_o \hat{j} - \cos \theta_o \hat{k}) \\ &= \begin{pmatrix} 0 \\ \tau_{21} \\ \tau_{22} \\ \tau_{23} \\ (\tilde{\tau} \cdot \vec{v})_2 + q_2 \end{pmatrix}_{\theta=-\theta_o} (-\sin \theta_o) + \begin{pmatrix} 0 \\ \tau_{31} \\ \tau_{32} \\ \tau_{33} \\ (\tilde{\tau} \cdot \vec{v})_3 + q_3 \end{pmatrix}_{\theta=-\theta_o} (-\cos \theta_o).\end{aligned}$$

When summing the contribution from both sides, the terms that survive give:

$$\begin{aligned} \int_{A_{x_3+} \cup A_{x_3-}} \vec{F}_v \cdot \hat{n} \, dS &= [(\vec{F}_v \cdot \hat{n})|_{\theta=+\theta_o} + (\vec{F}_v \cdot \hat{n})|_{\theta=-\theta_o}]A \\ &= \begin{pmatrix} 0 \\ 0 \\ 2\mu(-2\frac{\sin\theta_o}{r}(v_r + \frac{\partial v_\theta}{\partial\theta})) - 2\lambda\sin\theta_o \vec{\nabla} \cdot \vec{v} \\ 2\mu(\sin\theta_o \frac{\partial v_\theta}{\partial r} + \frac{\sin\theta_o}{r}(\frac{\partial v_r}{\partial\theta} - v_\theta)) \\ 0 \end{pmatrix} A . \end{aligned} \quad (B.12)$$

We may now express the weak form of the Navier-Stokes equations over the axisymmetric domain Ω by making use of the results we obtained for the Euler equations. We modify the numerical fluxes of eq. (B.6) to include numerical viscous fluxes. We divide the right hand side of eq. (B.12) by $2\theta_o$ and add it to the right hand side of eq. (B.6) to get:

$$\begin{aligned} \frac{\partial \bar{U}}{\partial t} r_c A + \sum_{i \in \{x_{1\pm}, x_{2\pm}\}} (H - H_v)_i l_i r_i \\ + \begin{pmatrix} 0 \\ 0 \\ \rho(-v_\theta^2 \sin\theta_o) - p \sin\theta_o \\ \rho(v_r v_\theta \sin\theta_o) \\ 0 \end{pmatrix} \frac{A}{\theta_o} = \begin{pmatrix} 0 \\ 0 \\ \mu(-\frac{2\sin\theta_o}{r}(v_r + \frac{\partial v_\theta}{\partial\theta})) - \lambda\sin\theta_o \vec{\nabla} \cdot \vec{v} \\ \mu(\sin\theta_o \frac{\partial v_\theta}{\partial r} + \frac{\sin\theta_o}{r}(\frac{\partial v_r}{\partial\theta} - v_\theta)) \\ 0 \end{pmatrix} \frac{A}{\theta_o} . \end{aligned} \quad (B.13)$$

We take the limit of eq. (B.13) as θ_o shrinks to zero to obtain the final form of the Navier-Stokes equations for the axisymmetric volume Ω :

$$\begin{aligned} r_c A \frac{\partial}{\partial t} \begin{pmatrix} \rho \\ \rho v_x \\ \rho v_r \\ \rho v_\theta \\ E \end{pmatrix} + \sum_{i \in \{x_{1\pm}, x_{2\pm}\}} (H - H_v)_i l_i r_i \\ + \begin{pmatrix} 0 \\ 0 \\ -\rho v_\theta^2 - p \\ \rho v_r v_\theta \\ 0 \end{pmatrix} A = \begin{pmatrix} 0 \\ 0 \\ \mu(-\frac{2}{r}(v_r + \frac{\partial v_\theta}{\partial\theta})) - \lambda \vec{\nabla} \cdot \vec{v} \\ \mu(\frac{\partial v_\theta}{\partial r} + \frac{1}{r}(\frac{\partial v_r}{\partial\theta} - v_\theta)) \\ 0 \end{pmatrix} A . \end{aligned}$$

The divergence of the velocity that appears in the above equation is given in terms of the cylindrical system of coordinates as:

$$\vec{\nabla} \cdot \vec{v} = \frac{\partial v_x}{\partial x} + \frac{\partial v_r}{\partial r} + \frac{v_r}{r} + \frac{1}{r} \frac{\partial v_\theta}{\partial \theta} .$$

This axisymmetric finite volume formulation of the Euler and Navier-Stokes equations can be easily generalized for discretizations involving polygons with an arbitrary number of faces (e.g. triangular volume elements).

Appendix C

The Inviscid Flux Jacobians

In this section we present the block matrices that are used to compute the split fluxes using the Steger-Warming method. The chemical species are ordered such that the diatomic species are listed first, and then the monatomic species.

The Jacobian $S = \frac{\partial V}{\partial U}$, that transforms from the conservative variables to the primitive variables, is computed in such a way that the primitive variables are functions of the conserved variables. The least obvious of the calculations involves the pressure, which can be written in terms of the conserved variables alone as:

$$p = \frac{\sum_{s=1}^{ns} \rho_s \frac{R}{M_s}}{\sum_{s=1}^{ns} \rho_s C_{vs}} \left[E - \frac{1}{2}((\rho u)^2 + (\rho v)^2) \frac{1}{\sum_{s=1}^{ns} \rho_s} - E_v - \sum_{s=1}^{ns} \rho_s h_s^\circ \right]. \quad (C.1)$$

Then, differentiating this expression with respect to the conserved variables yields

$$\begin{aligned} \frac{\partial p}{\partial \rho_s} &= \left(\frac{R}{M_s} - C_{vs} \frac{\bar{R}}{C_v} \right) T + \frac{\bar{R}}{C_v} \left(\frac{1}{2} (u^2 + v^2) - h_s^\circ \right) \\ \frac{\partial p}{\partial \rho u} &= -u \frac{\bar{R}}{C_v} \\ \frac{\partial p}{\partial \rho v} &= -v \frac{\bar{R}}{C_v} \\ \frac{\partial p}{\partial E_v} &= -\frac{\bar{R}}{C_v} \\ \frac{\partial p}{\partial E} &= \frac{\bar{R}}{C_v}, \end{aligned} \quad (C.2)$$

where we have defined

$$C_v = \sum_{s=1}^{ns} \frac{\rho_s}{\rho} C_{vs} \quad \text{and} \quad \bar{R} = \sum_{s=1}^{ns} \frac{\rho_s}{\rho} \frac{R}{M_s}. \quad (C.3)$$

The final form of the matrix S is

$$S = \frac{\partial V}{\partial U} = \begin{pmatrix} 1 & & & & & & \\ 0 & 1 & & & & & \\ \vdots & \vdots & \ddots & & & & \\ 0 & 0 & \dots & 1 & & & \\ -\frac{u}{\rho} & -\frac{u}{\rho} & \dots & -\frac{u}{\rho} & \frac{1}{\rho} & & \\ -\frac{v}{\rho} & -\frac{v}{\rho} & \dots & -\frac{v}{\rho} & 0 & \frac{1}{\rho} & \\ -\frac{e_v}{\rho} & -\frac{e_v}{\rho} & \dots & -\frac{e_v}{\rho} & 0 & 0 & \frac{1}{\rho} \\ \frac{\partial p}{\partial \rho_1} & \frac{\partial p}{\partial \rho_2} & \dots & \frac{\partial p}{\partial \rho_{ns}} & \frac{\partial p}{\partial \rho u} & \frac{\partial p}{\partial \rho v} & \frac{\partial p}{\partial E_v} & \frac{\partial p}{\partial E} \end{pmatrix} \quad (C.4)$$

In principle, we could invert S directly to obtain its inverse S^{-1} , but it is easier to compute $S^{-1} = \frac{\partial U}{\partial V}$ directly. The derivatives of E with respect to the non-conserved variables are computed by writing E in terms of these variables

$$E = \left(\frac{\sum_{s=1}^{ns} \rho_s C_{vs}}{\sum_{s=1}^{ns} \rho_s \frac{R}{M_s}} \right) p + \frac{1}{2} \sum_{s=1}^{ns} \rho_s (u^2 + v^2) + \sum_{s=1}^{ns} \rho_s e_{vs} + \sum_{s=1}^{ns} \rho_s h_s^\circ, \quad (C.5)$$

and taking derivatives with respect to these variables

$$\begin{aligned} \frac{\partial E}{\partial \rho_s} &= \left(C_{vs} - \frac{C_v}{R} \frac{R}{M_s} \right) T + \frac{1}{2} (u^2 + v^2) + e_v + h_s^\circ \\ \frac{\partial E}{\partial u} &= \rho u \\ \frac{\partial E}{\partial v} &= \rho v \\ \frac{\partial E}{\partial e_v} &= \sum_{s=1}^{nd} \rho_s \\ \frac{\partial E}{\partial p} &= \frac{C_v}{R}. \end{aligned} \quad (C.6)$$

The Jacobian matrix S^{-1} is

$$S^{-1} = \frac{\partial U}{\partial V} = \begin{pmatrix} 1 & & & & & & & \\ 0 & 1 & & & & & & \\ \vdots & \vdots & \ddots & & & & & \\ 0 & 0 & \dots & 1 & & & & \\ u & u & \dots & u & \rho & & & \\ v & v & \dots & v & 0 & \rho & & \\ e_v & e_v & \dots & e_v & 0 & 0 & \rho & \\ \frac{\partial E}{\partial \rho_1} & \frac{\partial E}{\partial \rho_2} & \dots & \frac{\partial E}{\partial \rho_{ns}} & \frac{\partial E}{\partial u} & \frac{\partial E}{\partial v} & \frac{\partial E}{\partial e_v} & \frac{\partial E}{\partial p} \end{pmatrix} \quad (C.7)$$

The orthogonal transformation that appears in the split fluxes, rotates the momenta such that the Jacobian matrix to be diagonalized resembles the Jacobian matrix of the flux in the x -direction, A (note that A is not *primed* because it is the Jacobian appearing in $F = AU$, where F is the flux component in the x -direction). In this way, the diagonalization involves u' and v' , whereas in the diagonalization of the x -direction flux we would encounter u and v . The velocity components u' and v' are the components normal and tangential to the face in question respectively (these velocity projections arise naturally if we compute the product RS). The rotation matrix and its inverse are

$$R = \begin{pmatrix} 1 & & & & \\ & \ddots & & & \\ & & 1 & & \\ & & & s_x & s_y \\ & & & -s_y & s_x \\ & & & & 1 \\ & & & & & 1 \end{pmatrix} \quad (C.8)$$

$$R^{-1} = \begin{pmatrix} 1 & & & & \\ & \ddots & & & \\ & & 1 & & \\ & & & s_x & -s_y \\ & & & s_y & s_x \\ & & & & 1 \\ & & & & & 1 \end{pmatrix}. \quad (C.9)$$

The matrix to be diagonalized is

$$\frac{\partial V}{\partial U} \frac{\partial F'}{\partial V} = \begin{pmatrix} u' & 0 & \dots & 0 & \rho_1 \\ 0 & u' & \dots & 0 & \rho_2 \\ \vdots & \vdots & \ddots & \vdots & \vdots \\ 0 & 0 & \dots & u' & \rho_{ns} \\ & & & & u' \\ & & & & 0 \\ & & & & 0 \\ & & & & 0 \\ & & & & 1/\rho \\ & & & & 0 \\ & & & & 0 \\ & & & & 0 \\ & & & & 0 \\ \rho a^2 & 0 & 0 & 0 & u' \end{pmatrix}, \quad (C.10)$$

and the speed of sound a has been defined such that

$$\rho a^2 = \sum_{s=1}^{ns} \rho_s \frac{\partial p}{\partial \rho_s} + 2\rho u \frac{\partial p}{\partial \rho u} + \rho v \frac{\partial p}{\partial \rho v} + E_v \frac{\partial p}{\partial E_v} + \left(E + p + u \frac{\partial E}{\partial u} \right) \frac{\partial p}{\partial E}, \quad (C.11)$$

which may be simplified using the expressions above

$$\begin{aligned} a^2 &= \left(\frac{\bar{R}}{C_v} + 1 \right) \bar{R}T \\ &= \bar{\gamma} \bar{R}T, \end{aligned} \quad (C.12)$$

and $\bar{\gamma}$ is the ratio of the translational-rotational specific heats of the gas $\bar{\gamma} = C_p/C_v$.

The similarity transformation consists of the diagonal matrix of eigenvalues

$$\Lambda = \text{diag}(u', u', \dots, u', u' + a, u', u', u' - a), \quad (C.13)$$

and the left and right eigenvector matrices

$$C_A^{-1} = \begin{pmatrix} 1 & 0 & \dots & 0 & c_1/a^2 & 0 & 0 & c_1/a^2 \\ 0 & 1 & \dots & 0 & c_2/a^2 & 0 & 0 & c_2/a^2 \\ \vdots & \vdots & \ddots & \vdots & \vdots & \vdots & \vdots & \vdots \\ 0 & 0 & \dots & 1 & c_{ns}/a^2 & 0 & 0 & c_{ns}/a^2 \\ & & & & 1/a\rho & 0 & 0 & -1/a\rho \\ & & & & 0 & 1 & 0 & 0 \\ & & & & 0 & 0 & 1 & 0 \\ & & & & 1 & 0 & 0 & 1 \end{pmatrix} \quad (C.14)$$

$$C_A = \begin{pmatrix} 1 & 0 & \dots & 0 & & -c_1/a^2 \\ 0 & 1 & \dots & 0 & & -c_2/a^2 \\ \vdots & \vdots & \ddots & \vdots & & \vdots \\ 0 & 0 & \dots & 1 & & -c_{ns}/a^2 \\ & & & & a\rho/2 & 0 & 0 & 1/2 \\ & & & & 0 & 1 & 0 & 0 \\ & & & & 0 & 0 & 1 & 0 \\ & & & & -a\rho/2 & 0 & 0 & 1/2 \end{pmatrix}. \quad (C.15)$$

The operator E_w used in the implicit inviscid boundary conditions to reflect the momentum normal to the wall is

$$E_w = \begin{pmatrix} 1 & & & & & \\ & \ddots & & & & \\ & & 1 & & & \\ & & & 1 - s'_x^2 & -2s'_y s'_x & \\ & & & -2s'_x s'_y & 1 - s'_y^2 & \\ & & & & & 1 \\ & & & & & 1 \end{pmatrix}. \quad (C.16)$$

Appendix D

The Implicit Viscous Jacobians

In this section we present the block matrices that are used in the implicit approximation of the viscous fluxes. For convenience, we define

$$L_\xi = -\left(\frac{\partial \xi}{\partial x} s'_x + \frac{\partial \xi}{\partial y} s'_y\right) \quad \text{and} \quad L_\eta = -\left(\frac{\partial \eta}{\partial x} s'_x + \frac{\partial \eta}{\partial y} s'_y\right)$$

and the matrices M_ξ and M_η are given below.

The Jacobian $N = \frac{\partial \mathbf{V}}{\partial U}$ which is used to map from the conserved variables to the primitive variables used in the viscous implicit formulation is

$$N = \begin{pmatrix} \frac{\partial c_1}{\partial \rho_1} & \frac{\partial c_1}{\partial \rho_2} & \cdots & \frac{\partial c_1}{\partial \rho_{ns}} \\ \frac{\partial c_2}{\partial \rho_1} & \frac{\partial c_2}{\partial \rho_2} & \cdots & \frac{\partial c_2}{\partial \rho_{ns}} \\ \vdots & \vdots & \ddots & \vdots \\ \frac{\partial c_{ns}}{\partial \rho_1} & \frac{\partial c_{ns}}{\partial \rho_2} & \cdots & \frac{\partial c_{ns}}{\partial \rho_{ns}} \\ -\frac{u}{\rho} & -\frac{u}{\rho} & \cdots & -\frac{u}{\rho} & 1/\rho & 0 \\ -\frac{v}{\rho} & -\frac{v}{\rho} & \cdots & -\frac{v}{\rho} & 0 & 1/\rho \\ -\frac{e_v}{\rho} & -\frac{e_v}{\rho} & \cdots & -\frac{e_v}{\rho} & 0 & 0 & 1/\rho \\ \frac{\partial T}{\partial \rho_1} & \frac{\partial T}{\partial \rho_2} & \cdots & \frac{\partial T}{\partial \rho_{ns}} & \frac{\partial T}{\partial (\rho u)} & \frac{\partial T}{\partial (\rho v)} & \frac{\partial T}{\partial E_v} & \frac{\partial T}{\partial E} \end{pmatrix}$$

and the derivatives are

$$\begin{aligned} \frac{\partial T}{\partial \rho_s} &= \frac{1}{\rho C_v} (-C_{vs}T + \frac{1}{2}(u^2 + v^2) - h_s^\circ) \\ \frac{\partial T}{\partial (\rho u)} &= -\frac{u}{\rho C_v} \\ \frac{\partial T}{\partial (\rho v)} &= -\frac{v}{\rho C_v} \\ \frac{\partial T}{\partial E_v} &= -\frac{1}{\rho C_v} \\ \frac{\partial T}{\partial E} &= \frac{1}{\rho C_v} \\ \frac{\partial c_r}{\partial \rho_s} &= (\delta_{rs} - c_r) \frac{1}{\rho} \end{aligned}$$

$$M_\xi = \begin{pmatrix} \rho\mathcal{D}_1L_\xi & & & & \\ 0 & \rho\mathcal{D}_2L_\xi & & & \\ \vdots & \vdots & \ddots & & \\ 0 & 0 & \dots & \rho\mathcal{D}_{\text{ns}}L_\xi & \\ 0 & 0 & \dots & 0 & -s'_x(\lambda + 2\mu)\frac{\partial\xi}{\partial x} - s'_y\mu\frac{\partial\xi}{\partial y} \\ 0 & 0 & \dots & 0 & -s'_y\lambda\frac{\partial\xi}{\partial x} - s'_x\mu\frac{\partial\xi}{\partial y} \\ \rho\mathcal{D}_1e_{v1}L_\xi & \rho\mathcal{D}_2e_{v2}L_\xi & \dots & \rho\mathcal{D}_{\text{ns}}e_{v\text{ns}}L_\xi & 0 & 0 & \frac{\kappa_v}{C_{vv}}L_\xi \\ \rho\mathcal{D}_1h_1L_\xi & \rho\mathcal{D}_2h_2L_\xi & \dots & \rho\mathcal{D}_{\text{ns}}h_{\text{ns}}L_\xi & -((2\mu + \lambda)us'_x + \lambda vs'_y)\frac{\partial\xi}{\partial x} & -((us'_x + vs'_y)\lambda + 2\mu vs'_x)\frac{\partial\xi}{\partial y} & \frac{\kappa_v}{C_{vv}}L_\xi \kappa L_\xi \\ & & & & + \mu(vs'_x + us'_y)\frac{\partial\xi}{\partial y} & + \mu(vs'_x + us'_y)\frac{\partial\xi}{\partial x} & \end{pmatrix}$$

$$M_\eta = \begin{pmatrix} \rho\mathcal{D}_1L_\eta & & & & \\ 0 & \rho\mathcal{D}_2L_\eta & & & \\ \vdots & \vdots & \ddots & & \\ 0 & 0 & \dots & \rho\mathcal{D}_{\text{ns}}L_\eta & \\ 0 & 0 & \dots & 0 & -s'_x(\lambda + 2\mu)\frac{\partial\eta}{\partial x} - s'_y\mu\frac{\partial\eta}{\partial y} \\ 0 & 0 & \dots & 0 & -s'_y\lambda\frac{\partial\eta}{\partial x} - s'_x\mu\frac{\partial\eta}{\partial y} \\ \rho\mathcal{D}_1e_{v1}L_\eta & \rho\mathcal{D}_2e_{v2}L_\eta & \dots & \rho\mathcal{D}_{\text{ns}}e_{v\text{ns}}L_\eta & 0 & -s'_x\lambda\frac{\partial\eta}{\partial y} - s'_y\mu\frac{\partial\eta}{\partial x} \\ \rho\mathcal{D}_1h_1L_\eta & \rho\mathcal{D}_2h_2L_\eta & \dots & \rho\mathcal{D}_{\text{ns}}h_{\text{ns}}L_\eta & -\left((2\mu + \lambda)us'_x + \lambda vs'_y\right)\frac{\partial\eta}{\partial x} & -s'_x\mu\frac{\partial\eta}{\partial x} - s'_y(\lambda + 2\mu)\frac{\partial\eta}{\partial y} \\ & & & & +\mu(vs'_x + us'_y)\frac{\partial\eta}{\partial y} & 0 \\ & & & & +((us'_x + vs'_y)\lambda + 2\mu vs'_y)\frac{\partial\eta}{\partial y} & \frac{\kappa_v}{C_{vv}}L_\eta \end{pmatrix}$$

Appendix E

The Implicit Source Term Jacobians

In this section we present the block matrices that are used in the implicit treatment of the chemical sources appearing in the species mass conservation and vibrational energy conservation equations. In general, this involves the linearization of the source terms in time by taking derivatives with respect to the conserved variables.

Vibrational energy source term

There are two vibrational energy source terms which need to be linearized in time, in order to be evaluated at the future time level. The first term is the sum of the vibrational energy relaxation rates of the diatomic species ($Q_{t-v_s}^{(LT)}$). The second term is due to the recombination of diatomic species (Q_v). We will examine each of the terms separately.

The Landau-Teller model for the rate of vibrational energy relaxation of diatomic species s is expressed as

$$Q_{t-v_s}^{(LT)} = \rho_s \frac{e_{v_s}^* - e_{v_s}}{\langle \tau_s \rangle},$$

where

$$e_{v_s} = \frac{R}{M_s} \frac{\theta_{v_s}}{\exp(\theta_{v_s}/T_v) - 1}, \quad , \quad e_{v_s}^* = e_{v_s}|_{T_v=T},$$

and the molar averaged relaxation time $\langle \tau_s \rangle$ depends on the local state of the gas. In order to express the Jacobian, we need to obtain derivatives of the energy relaxation rate with respect to each of the conserved quantities U_i . The derivatives will be of the form:

$$\frac{\partial}{\partial U_r} Q_{t-v_s}^{(LT)} = \delta_{sr} \frac{e_{v_s}^* - e_{v_s}}{\langle \tau_s \rangle} + \frac{\rho_s}{\langle \tau_s \rangle} \frac{\partial}{\partial U_r} (e_{v_s}^* - e_{v_s}) - \rho_s \frac{e_{v_s}^* - e_{v_s}}{\langle \tau_s \rangle^2} \frac{\partial}{\partial U_r} \langle \tau_s \rangle$$

The derivatives of e_{v_s} and $e_{v_s}^*$ with respect to U_r are

$$\begin{aligned}
\frac{\partial e_{vs}}{\partial \rho_r} &= \left(\frac{\partial e_{vs}}{\partial T_v} \right)_{T_v} \frac{\partial T_v}{\partial \rho_r}, & \frac{\partial e_{vs}^*}{\partial \rho_r} &= \left(\frac{\partial e_{vs}}{\partial T_v} \right)_{T_v=T} \frac{\partial T}{\partial \rho_r} \\
\frac{\partial e_{vs}}{\partial (\rho u)} &= \left(\frac{\partial e_{vs}}{\partial T_v} \right)_{T_v} \frac{\partial T_v}{\partial (\rho u)}, & \frac{\partial e_{vs}^*}{\partial (\rho u)} &= \left(\frac{\partial e_{vs}}{\partial T_v} \right)_{T_v=T} \frac{\partial T}{\partial (\rho u)} \\
\frac{\partial e_{vs}}{\partial (\rho v)} &= \left(\frac{\partial e_{vs}}{\partial T_v} \right)_{T_v} \frac{\partial T_v}{\partial (\rho v)}, & \frac{\partial e_{vs}^*}{\partial (\rho v)} &= \left(\frac{\partial e_{vs}}{\partial T_v} \right)_{T_v=T} \frac{\partial T}{\partial (\rho v)} \\
\frac{\partial e_{vs}}{\partial E_v} &= \left(\frac{\partial e_{vs}}{\partial T_v} \right)_{T_v} \frac{\partial T_v}{\partial E_v}, & \frac{\partial e_{vs}^*}{\partial E_v} &= \left(\frac{\partial e_{vs}}{\partial T_v} \right)_{T_v=T} \frac{\partial T}{\partial E_v} \\
\frac{\partial e_{vs}}{\partial E} &= \left(\frac{\partial e_{vs}}{\partial T_v} \right)_{T_v} \frac{\partial T_v}{\partial E}, & \frac{\partial e_{vs}^*}{\partial E} &= \left(\frac{\partial e_{vs}}{\partial T_v} \right)_{T_v=T} \frac{\partial T}{\partial E}
\end{aligned}$$

The derivatives of T_v with respect to the conserved variables are obtained by means of implicit differentiation using the expression for E_v ,

$$E_v = \sum_{s=1}^{ns} \rho_s e_{vs} = \sum_{s=1}^{ns} \rho_s \frac{R}{M_s} \frac{\theta_{vs}}{\exp(\theta_{vs}/T_v) - 1}.$$

For example we consider

$$\frac{\partial E_v}{\partial \rho_r} = e_{vr} + \sum_{s=1}^{ns} \left[\rho_s \left(\frac{\partial e_{vs}}{\partial T_v} \right) \right] \frac{\partial T_v}{\partial \rho_r} = 0,$$

which gives

$$\frac{\partial T_v}{\partial \rho_r} = -e_{vr} / \sum_{s=1}^{ns} \left[\rho_s \left(\frac{\partial e_{vs}}{\partial T_v} \right) \right].$$

Similarly we obtain

$$\begin{aligned}
\frac{\partial T_v}{\partial (\rho u)} &= 0, \\
\frac{\partial T_v}{\partial (\rho v)} &= 0, \\
\frac{\partial T_v}{\partial E_v} &= 1 / \sum_{s=1}^{ns} \left[\rho_s \left(\frac{\partial e_{vs}}{\partial T_v} \right) \right], \\
\frac{\partial T_v}{\partial E} &= 0.
\end{aligned}$$

The remaining derivatives of the molar-averaged relaxation times are

$$\begin{aligned}
\frac{\partial}{\partial \rho_r} \langle \tau_s \rangle &= - \frac{\langle \tau_s \rangle^2}{M_r} \frac{1}{\sum_{l=1}^{ns} \rho_l / M_l} \left(\frac{1}{\tau_{sr}} - \frac{1}{\langle \tau_s \rangle} \right) \\
&\quad - \langle \tau_s \rangle^2 \sum_{k=1}^{ns} \left[\frac{X_k}{\tau_{sk}} \left(\frac{1}{p} \frac{\partial p}{\partial \rho_r} + \frac{1}{3} A_{sk} T^{-4/3} \frac{\partial T}{\partial \rho_r} \right) \right],
\end{aligned}$$

$$\begin{aligned} \frac{\partial}{\partial(\rho u)} <\tau_s> = <\tau_s>^2 \sum_{k=1}^{ns} \left[\frac{X_k}{\tau_{sk}} \left(\frac{1}{p} \frac{\partial p}{\partial(\rho u)} + \frac{1}{3} A_{sk} T^{-4/3} \frac{\partial T}{\partial(\rho u)} \right) \right], \\ \frac{\partial}{\partial(\rho v)} <\tau_s> = <\tau_s>^2 \sum_{k=1}^{ns} \left[\frac{X_k}{\tau_{sk}} \left(\frac{1}{p} \frac{\partial p}{\partial(\rho v)} + \frac{1}{3} A_{sk} T^{-4/3} \frac{\partial T}{\partial(\rho v)} \right) \right], \\ \frac{\partial}{\partial E_v} <\tau_s> = <\tau_s>^2 \sum_{k=1}^{ns} \left[\frac{X_k}{\tau_{sk}} \left(\frac{1}{p} \frac{\partial p}{\partial E_v} + \frac{1}{3} A_{sk} T^{-4/3} \frac{\partial T}{\partial E_v} \right) \right], \\ \frac{\partial}{\partial E} <\tau_s> = <\tau_s>^2 \sum_{k=1}^{ns} \left[\frac{X_k}{\tau_{sk}} \left(\frac{1}{p} \frac{\partial p}{\partial E} + \frac{1}{3} A_{sk} T^{-4/3} \frac{\partial T}{\partial E} \right) \right]. \end{aligned}$$

The pressure and translational-rotational temperature derivatives that appear above were presented previously.

Chemical source terms

There are two types of reactions involved in the species density generation terms; these are the dissociation reactions and the Zeldovich exchange reactions. In terms of the mathematical expressions for the reaction rates, we can view the exchange reactions as a special form of the dissociation reactions. Therefore only the Jacobian terms involving dissociation reactions are presented here.

The generic form of a dissociation reaction is:

$$\mathcal{R}_i = \sum_m \left[k_{bim} \frac{\rho_r}{M_r} \frac{\rho_s}{M_s} \frac{\rho_m}{M_m} - k_{fim} \frac{\rho_i}{M_i} \frac{\rho_m}{M_m} \right]$$

where i is the dissociating species, r, s are the dissociated atoms, and m is the generic collision partner. The derivatives of the reaction rate with respect to the conserved quantities take the generic form:

$$\begin{aligned} \frac{\partial}{\partial U_j} \mathcal{R}_i = & \sum_{m=1}^{ns} \left[\frac{\partial}{\partial U_j} k_{bim} \frac{\rho_r}{M_r} \frac{\rho_s}{M_s} \frac{\rho_m}{M_m} - \frac{\partial}{\partial U_j} k_{fim} \frac{\rho_i}{M_i} \frac{\rho_m}{M_m} \right] \\ & + \sum_{m=1}^{ns} \left[k_{bim} \left(\frac{\delta_{jr}}{M_r} \frac{\rho_s}{M_s} \frac{\rho_m}{M_m} + \frac{\rho_r}{M_r} \frac{\delta_{js}}{M_s} \frac{\rho_m}{M_m} + \frac{\rho_r}{M_r} \frac{\rho_s}{M_s} \frac{\delta_{jm}}{M_m} \right) \right] \\ & - \sum_{m=1}^{ns} \left[k_{fim} \left(\frac{\delta_{ji}}{M_i} \frac{\rho_m}{M_m} + \frac{\rho_i}{M_i} \frac{\delta_{jm}}{M_m} \right) \right]. \end{aligned}$$

The derivatives of the forward reaction rate coefficient are computed using the chain rule as:

$$\frac{\partial}{\partial U_j} k_{fm} = \frac{\partial T}{\partial U_j} \frac{\partial}{\partial T} k_{fm},$$

where

$$\frac{\partial}{\partial T} k_{fm} = k_{fm} \left(\frac{\eta_m}{T} + \frac{\theta_m}{T^2} \right).$$

The backward rate coefficient is given in terms of the equilibrium constant, and its derivative is expressed as:

$$\frac{\partial}{\partial U_j} k_{bm} = \left(\frac{\partial}{\partial T} k_{fm} K_{eq}^{-1} + k_{fm} \frac{\partial}{\partial T} K_{eq}^{-1} \right) \frac{\partial T}{\partial U_j}.$$

References

- ANDERSON, J. D., (1989) *Hypersonic and High Temperature Gas Dynamics*, McGraw-Hill.
- BALDWIN, B. S. AND LOMAX, H., (1978) "Thin Layer Approximation and Algebraic Model for Separated Turbulent Flows," *AIAA Paper No. 78-257*.
- BIRCH, S. F. AND KEYES, J. W., (1972) "Transition in Compressible Free Shear Layers," *Journal of Spacecraft and Rockets*, **9** (8), pp. 623-624.
- BLACK, G., WISE, H., SCHECHTER, S., AND SHARPLESS, R. L., (1974) "Measurements of vibrationally excited molecules by Raman Scattering. II. Surface Deactivation of vibrationally excited N₂," *J. Chem. Phys.*, **60** (9), pp. 3526-3536.
- BLOTTNER, F. G., JOHNSON, M., AND ELLIS, M., (1971) "Chemically Reacting Viscous Flow Program for Multi-Component Gas Mixtures," Sandia Laboratories Report No. SC-RR-70-754, Albuquerque, New Mexico.
- BOYD, I. D., CHEN, G., AND CANDLER, G. V., (1995) "Predicting Failure of the Continuum Fluid Equations in Transitional Hypersonic Flows," *Phys. of Fluids*, **7** (1), pp. 210-219.
- CANDLER, G. V., (1988) "The Computation of Weakly Ionized Hypersonic Flows in Thermo-chemical Nonequilibrium," *Ph.D. Thesis*, Stanford University.
- CANDLER, G. V., NOMPELIS, I., AND HOLDEN, M. S., (2000) "Computational Analysis of Hypersonic Laminar Viscous-Inviscid Interactions," *AIAA Paper No. 2000-0532*.
- CANDLER, G. V., NOMPELIS, I., AND DRUGUET, M.-C., (2001) "Navier-Stokes Predictions of Hypersonic Double-Cone and Cylinder-Flare Flow Fields," *AIAA Paper No. 2000-1024*.
- CANDLER, G. V., NOMPELIS, I., DRUGUET, M.-C., HOLDEN, M. S., BOYD, I. D., AND WANG, W.-L., (2002) "CFD Validation for Hypersonic Flight: Hypersonic Double-Cone Flow Simulations," *AIAA Paper No. 2002-0581*.
- CANDLER, G. V. AND NOMPELIS, I., (2002) "CFD Validation for Hypersonic Flight: Real Gas Effects," *AIAA Paper No. 2002-0434*.

- CATRIS, S. AND AUPOIX, B., (2000) "Density Corrections for Turbulence Models," *Aerospace Science and Technology*, **4**, pp. 1-11.
- DRUGUET, M.-C., CANDLER, G. V., AND NOMPELIS, I., (2002) "Navier-Stokes Computations of Hypersonic Double-Cone Flows: Influence of Numerics," Proceedings of the West East High Speed Flow Field Conference, Marseille, France.
- DRUGUET, M.-C., CANDLER, G. V., AND NOMPELIS, I., (2003) "Simulations of Viscous Hypersonic Double-Cone Flows: Influence of Numerics," *AIAA Paper No. 2003-3548*.
- GAITONDE, D., CANUPP, P. W., AND HOLDEN, M. S., (2002) "Heat Transfer Predictions in a Laminar Hypersonic Viscous/Inviscid Interaction," *Journal of Thermophysics and Heat Transfer*, **16** (4), pp. 481-489.
- GNOFFO, P. A., (2001) "CFD Validation Studies for Hypersonic Flow Prediction," *AIAA Paper No. 2001-1025*.
- GÖKÇEN, T., (1989) "Computation of Hypersonic Low Density Flows with Thermochemical Nonequilibrium," *Ph.D. Thesis*, Stanford University.
- HARVEY, J. K., HOLDEN, M. S., AND WADHAMS, T. P., (2001) "Code Validation Study of Laminar Shock/Boundary Layer and Shock/Shock Interactions in Hypersonic Flows. Part B: Comparison with Navier-Stokes and DSMC Solutions," *AIAA Paper No. 2001-1031*.
- HIRSCH, C. (1991) *Numerical Computation of Internal and External Flows*, Wiley, New York.
- HOLDEN, M. S. (1998) "Shock Interaction Phenomena in Hypersonic Flows," *AIAA Paper No. 98-2751*.
- HOLDEN, M. S. (2000) "Experimental Studies of Laminar Separated Flows Induced by Shock Wave/Boundary Layer and Shock/Shock Interaction in Hypersonic Flows for CFD Validation," *AIAA Paper No. 2000-0930*.
- HOLDEN, M. S. AND WADHAMS, T. P., (2001) "Code Validation Study of Laminar Shock/Boundary Layer and Shock/Shock Interactions in Hypersonic Flows. Part A: Experimental Measurements," *AIAA Paper No. 2001-1031*.

- HOLDEN, M. S. (2004) "Experimental Studies in LENS Shock and Expansion Tunnel to Examine Real-Gas Effects in Hypervelocity Flows," *AIAA Paper No. 2004-0916*.
- LANEY, C. B. (1998) *Computational Gasdynamics*, Cambridge Univ. Press.
- LEE, J.-H. (1985) "Basic Governing Equations for the Flight Regimes of Aeroassisted Orbital Transfer Vehicles," *Thermal Design of Aeroassisted Orbital Transfer Vehicles*, H. F. Nelson (Ed.), Progress in Aeronautics and Astronautics, **96**, pp. 3-53.
- LUKASIEWICZ, J., (1973) *Experimental Methods of Hypersonics*, Gasdynamics Series, **3**, Marcel Dekker.
- MEOLANS, J. G. AND GRAUR, I. A., (2002) "Thermal Slip Boundary Conditions at the Wall in Nonequilibrium Flows," Proceedings of the West East High Speed Flow Fields 2002 Conference, Marseilles, France, Apr. 2002.
- MILLIKAN, R. C. AND WHITE, D. R., (1953) "Systematics of Vibrational Relaxation," *J. Chem. Phys.*, **39**, pp. 3209-3213.
- NOMPELIS, I., CANDLER, G. V., HOLDEN, M. S. AND WADHAMS, T. P., (2003) "Real Gas Effects on Hypersonic Shock Wave Laminar Boundary Layer Interactions," *AIAA Paper No. 2003-0443*.
- NOMPELIS, I., CANDLER, G. V., HOLDEN, M. S. AND WADHAMS, T. S., (2003) "Computational Investigation of Hypersonic Viscous/Inviscid Interactions in High Enthalpy Flows," *AIAA Paper No. 2003-3642*.
- NOMPELIS, I., CANDLER, G. V. AND HOLDEN, M. S., (2003) "Effect of Vibrational Nonequilibrium on Hypersonic Double-Cone Experiments," *AIAA Journal*, **41** (11), pp. 2162-2169.
- NOMPELIS, I., CANDLER, G. V., WADHAMS, T. P. AND HOLDEN, M. S., (2003) "Numerical Simulation of High-Enthalpy Experiments in the LENS-X Expansion Tube Facility," *AIAA Paper No. 2004-1000*.
- OLEJNICZAK, J., WRIGHT, M. J. AND CANDLER, G. V., (1997) "Numerical Study of Inviscid Shock Interactions on Double-Wedge Geometries," *J. Fluid Mech.*, **352**, pp. 1-25.

- OLEJNICZAK, J., CANDLER, G. V., AND HORMUNG, H. G., (1997) "Computation of Double-Cone Experiments in High Enthalpy Nitrogen," *AIAA Paper No. 97-2549*.
- OLEJNICZAK, J., (1997) "Computational and Experimental Study of Nonequilibrium Chemistry in Hypersonic Flows," *Ph.D. Thesis*, University of Minnesota.
- OLEJNICZAK, J., CANDLER, G. V., WRIGHT, M. J., LEYVA, I. AND HORMUNG, H. G., (1999) "An Experimental and Computational Study of High Enthalpy Double-Wedge Flows," *Journal of Thermophysics and Heat Transfer*, **13** (4), pp. 431-440.
- PARK, C., (1985) "On Convergence of Computation of Chemically Reacting Flows," *AIAA Paper No. 85-0247*.
- PARK, C., (1986) "Assessment of Two-Temperature Kinetic Model for Dissociating and Weakly Ionizing Nitrogen," *AIAA Paper No. 86-1347*.
- PARK, C., (1988) "Two Temperature Interpretation of Dissociation Rate Data for N₂ and O₂," *AIAA Paper No. 88-0458*.
- PARK, C., (1990) *Nonequilibrium Hypersonic Aerothermodynamics*, John Wiley & Sons.
- ROY, C. J., GALLIS, M. A., BARTEL, T. J, AND PAYNE, J. L., (2001) "Navier-Stokes and Direct Simulation Monte Carlo Predictions for Laminar Hypersonic Separation," *AIAA Paper No. 2001-1024*.
- SANDRERS, R., MORANO, E. AND DRUGUET, M.-C., (1998) "Multidimensional Dissipation for Upwind Schemes Stability and Applications to Gas Dynamics," *J. of Computational Physics*, **145** (2), pp. 511-537.
- SCHAAF, S.A. AND CHAMBRE, P. L., (1966) *Flow of Rarefied Gases*, Princeton Univ. Press.
- SPALART, P. R. AND ALLMARAS, S. R., (1992) "A One-Equation Turbulence Model for Aerothermodynamic Flows," *AIAA Paper No. 92-0439*.
- STEGER, J. L. AND WARMING, R. F., (1981) "Flux Vector Splitting for the Inviscid Gasdynamic Equations with Application to Finite Difference Methods," *J. Comp. Phys.*, **40**, pp. 263-293.

- TORO, E. F., (1997) *Riemann Solvers and Numerical Methods for Fluid Dynamics*, Springer.
- VINCENTI, W. G. AND KRUGER, C. H., (1982) *Introduction to Physical Gas Dynamics*, Krieger Publishing Company.
- WILKE, C. R., (1950) "A Viscosity Equation for Gas Mixtures," *J. Chem. Phys.*, **18**, pp. 517-519.
- WRIGHT, M. J., (1997) "A Family of Data-Parallel Relaxation Methods for the Navier-Stokes Equations," *Ph.D. Thesis*, University of Minnesota.
- WRIGHT, M. J., BOSE, D., AND CANDLER, G. V., (1998) "A Data-Parallel Line Relaxation Method for the Navier-Stokes Equations." *AIAA Journal*, **36** (9), pp. 1603-1609.
- WRIGHT, M. J., SINHA, K., AND CANDLER, G. V., (1999) "The Effect of Turbulence on Double-Cone Shock Interactions," *AIAA Paper No. 99-0146*, Jan. 1999.
- WRIGHT, M. J., SINHA, K., OLEJNICZAK, J., CANDLER, G. V., MAGRUDER, T. D. AND SMITS, A. J., (2000) "Numerical and Experimental Investigation of Double-Cone Shock Interactions," *AIAA Journal*, **38**(12), pp. 2268-2276.